Alma Mater Studiorum – Università di Bologna

DOTTORATO DI RICERCA IN

MONITORAGGIO E GESTIONE DELLE STRUTTURE E DELL'AMBIENTE - SEHM2

Ciclo XXXIV

Settore Concorsuale: 09/E3 Elettronica
Settore Scientifico Disciplinare: Ing-Inf/01 Elettronica

Embedded systems and advanced signal processing for Acousto-Ultrasonic Inspections

Presentata da: Michelangelo Maria Malatesta

Coordinatore Dottorato

Alessandro Marzani

Supervisore

Luca De Marchi

Co-supervisore

Nicola Testoni

Esame finale anno 2022

Abstract

Non Destructive Testing (NDT) and Structural Health Monitoring (SHM) are becoming essential in many application contexts, *e.g.* civil, industrial, aerospace, automotive etc., to reduce structures maintenance costs and improve safety. To foster the widespread diffusion of these techniques, essential features are reliability, precision, low cost, low invasiveness and scalability. Conventional inspection methods typically exploit bulky and expensive instruments and rely on high computational cost signal processing techniques. In such a context, the pressing need to overcome these limitations is the common thread that guided the work presented in this Thesis. In particular, this dissertation will investigate both embedded systems solutions and advanced signal processing for Acousto-Ultrasonic inspections.

In the first part, a scalable, low–cost and multi–sensors smart sensor network is introduced. The capability of this technology to carry out accurate modal analysis on structures undergoing flexural vibrations has been validated by means of two experimental campaigns. Then, the suitability of low–cost piezoelectric disks in modal analysis has been demonstrated. To enable the use of this kind of sensing technology in such non conventional applications, *ad–hoc* data merging algorithms have been developed.

In the second part, instead, imaging algorithms for Lamb waves inspection have been developed. More specifically, two beamforming algorithms capable

to achieve high–quality images (namely DMAS and DS-DMAS) have been implemented and validated on a carbon fibre plate. Results show that DMAS outperforms the canonical Delay and Sum (DAS) approach in terms of image resolution and contrast. Similarly, DS-DMAS can achieve better results than both DMAS and DAS by suppressing artefacts and noise. Moreover, an *ad–hoc* filtering technique referred to as Fresnel zone filtering has been presented to further enhance the damage imaging. To exploit the full potential of these procedures, accurate group velocity estimations are required. Since numerical models are not sufficiently accurate for this goal, novel wavefield analysis tools that can address the estimation of the dispersion curves from Scanner Laser Doppler Vibrometer acquisitions have been investigated. In particular, an image segmentation technique (called DRLSE) which operates in the wavefield k–space to draw out the wavenumber profile was validated. The DRLSE method was compared with compressive sensing methods to extract the group and phase velocity information. The validation, performed on three different carbon fibre plates, showed that the proposed solutions can accurately determine the wavenumber and velocities in polar coordinates at multiple excitation frequencies.

Contents

Acronyms

$PbZr_xTi_{1-x}O_3$**, or PZT** Lead Zirconate Titanate.

2DSWA 2D Sparse Wavefield Analysis.

ACC Accelerometer.

AE Acoustic Emission.

ANN Artificial Neural Network.

AR Autoregressive.

ART Algebraic Reconstruction.

ASWA Anisotropic Sparse Wavefield Analysis.

BSS Baseline Signal Stretch.

CC Correlation Coefficient.

CFRP Carbon Fibre Reinforced Plate.

CH Cluster Head.

CNR Contrast-to-Noise Ratio.

COMAC Coordinate MAC Damage.

CR Contrast Ratio.

CS Compressive Sensing.

CSI Cubic Spline Interpolation.

CWT Continuous Wavelet Transform.

DAQ Data AQuisition.

DAS Delay and Sum.

DMAS Delay Multiply and Sum.

DoA Direction of Arrival.

DoP Data over Power.

DP Damage Prognosis.

DRLSE Distance Regularized Level Set Evolution.

DS-DMAS Double-Stage Delay Multiply and Sum.

DSP Digital Signal Processing.

DToA Difference Time of Arrival.

EC Eddie Currents.

EMAT Electromagnetic Acoustic Transducer.

EMI ElectroMechanical Impedance.

FDD Frequency Domain Decomposition.

FDM Finite Difference Method.

FEM Finite Element Method.

FPU Floating Point Unit.

FZF Fresnel Zone Filtering.

GA Genetic Algorithm.

gCNR generalized Contrast-to-Noise ratio.

GUIGUW Graphical User Interface for Guided Ultrasonic Waves.

GW Guided Wave.

HANI Highly Anisotropic.

HSN Heterogeneous Sensor Network.

IIR Infinite Impulse Response.

IoS Internet of Structures.

IoT Internet of Things.

LDV Laser Doppler Vibrometer.

LISA Local Interaction Simulation Approach.

LSF Level Set Function.

LSM Least-Squares Method.

MAC Modal Assurance Criterion.

MAPD Mean Absolute Percentage Deviation.

MART Multi-resolution Algebraic Reconstruction Technology.

MCU Microcontroller Unit.

MEMS Micro Electro-Mechanical Systems.

MI Microwave-based Imaging.

MIMO Multiple Inputs Multiple Outputs.

MV Minimum Variance.

NDE Non Destructive Evaluation.

NDT Non Destructive Testing.

OBS Optimal Baseline Subtraction.

OGW Open Guided Waves.

OMA Operational Modal Analysis.

OMP Orthogonal Matching Pursuit.

PCA Principal Component Analysis.

PDE Partial Differential Equation.

PEC Pulsed Eddie Currents.

PECT Pulsed Eddie Currents Tomography.

PNR Peak-to-Noise Ratio.

PSD Power Spectral Density.

PSNR Peak Signal-to-Noise ratio.

PVDF PolyVinyliDene Fluoride.

PWAS Piezoelectric Wafer Active Sensors.

PZT Lead Zirconate Titanate.

RAPID Reconstruction Algorithm for the Probabilistic Inspection of Damage.

RMSD Root Mean Square Deviation.

RoI Region of Interest.

RTM Reverse Time Migration.

RTT Round Trip Time.

SAFE Semi-Analytical Finite Element.

SAN Sensor Area Network.

SANI Slightly ANIsotropic.

SDC Signal Difference Coefficient.

SH Shear Horizontal.

SHM Structural Health Monitoring.

SLDV Scanner Laser Doppler Vibrometer.

SN Sensor Node.

SNR Signal-to-Noise Ratio.

SRCNN Super-Resolution Convolutional Neural Network.

SSN Smart Sensor Network.

ToF Time-of-Flight.

uCT micro Computer Tomography.

UW Ultrasonic Wave.

UWB Ultra-Wideband.

WSSN Wireless Smart Sensor Network.

XCL X-ray Computed Laminography.

Chapter 1

Introduction

1.1 Motivations

All structures deteriorate with time. Civil, aerospace, automotive, oil and gas structures such as industrial facilities are subjected to natural and artificial decay which reduce the margin of safety or might generate serviceability problems. These issues can lead to high financial losses due to corrective maintenance. In the worst–case scenario, life losses can occur if critical failures remain undetected thus generating sudden structural collapse. For instance, in civil engineering context, famous bridge collapses can be remembered, such as the Tacoma Narrows Bridge in 1940 [1], the Laval overpass in Quebec, Canada, in 2006 [2] and the Morandi bridge in 2018 [3]. To avoid such kind of dramatic events, preventive maintenance is periodically scheduled to check the existence of critical damages which might put the structure itself at risk [4]. The main limitations of such an approach are the following. First, the structure history is usually exploited to determine significant changes in the main structural response, making the analysis difficult for novel constructions. Second, preventive maintenance is not effective against unexpected external actions,

possibly due to both natural and human actions (e.g. earthquakes, floods or sudden impacts). Finally, it is not cost-effective, since human intervention is required and the duty of the structure under test is usually interrupted. To tackle these problems, Structural Health Monitoring (SHM)) aim to continuously acquire and process data to assess the structural integrity by using permanently attached sensors. SHM is usually based on well established Non Destructive Testing (NDT) techniques, which aim to find material discontinuities and assess the structural conditions.

In this Thesis, both SHM and NDT approaches are investigated.

Among the many NDT methods, some can be adapted for permanent installation and exploited in SHM. Anyway, the migration of NDT technologies to address SHM needs is usually non-trivial, since conventional inspection instrumentation is often bulky and expensive. Thus, novel approaches have been investigated to perform reliable, affordable and accurate SHM. In particular, Smart Sensor Network (SSN) and Wireless Smart Sensor Network (WSSN) are rising as the most promising strategies to inspect large structures by continuous monitoring. The main idea is to exploit interconnected nodes with embedded signal processing capabilities to acquire, pre–process and transfer data to a central unit or a cloud. In such a way, a real–time evaluation of the structural integrity is enabled. This approach reduces drastically the overall cost since human intervention and unoptimized maintenance can be avoided. Moreover, the inspection capabilities can be enhanced by exploiting multi sensor types that act simultaneously. The acquisition of signals related to different physical phenomena is fundamental in data fusion, where the information gathered by the sensing technologies are complemented each other. The pressing need to develop such kind of hardware architectures, as well as suitable signal processing techniques, lays the groundwork for the first part of this Thesis,

where a novel heterogeneous approach based on multi sensing sensor network is presented.

In the second part of this dissertation, instead, the focus is on NDT methods. In 2008, Thomas Aastroem [5] discussed the fast evolution of NDT and their proliferation over the last sixty years. Just focusing on machine diagnostic, up to two hundred various methods can be listed. The availability of different approaches for specific needs makes NDT extremely efficient and adaptable to many different application contexts. Among NDT approaches, ultrasonic inspections based on Lamb waves have attracted a considerable attention, specially in the aerospace and automotive fields [6]. Lamb waves are stress waves that propagate through plate–like structures. Then, waves can be acquired by sensing elements such as piezoelectric sensors and processed to detect and characterize damages. In particular, localization of damages, delaminations and discontinuities in metallic and composite laminates is a hot topic in the SHM community. Despite the variety of techniques proposed in literature, one of the most exploited imaging methods still remain the well known Delay and Sum (DAS) beamforming algorithm due to its ease of use, low computational requirements and overall good performances. Nevertheless, DAS imaging has a low resolution due to the high levels of side lobes and limited off-axis signal rejection which leads to limited image resolution and contrast. Moreover, multimodal propagation, dispersion and material anisotropy can affect the imaging result and applicability to a real application case. Since very few comprehensive experimental methods for characterizing the propagation medium exist in literature, compensation and tuning procedures which might be applied to improve the damage localization are usually carried on by exploiting numerical models that are often not accurate enough.

For such reasons, the development of imaging methods that overcome DAS

limitations in terms of resolution and contrast, without dramatically rising the computational burden and implementation complexity, is fundamental. Similarly, the development of new tools for characterizing the waves propagation is a critical need in such a context. Thus, in this Thesis, both issues are addressed. In detail, innovative beamforming algorithms based on DAS are introduced and validated in different application case scenarios. Moreover, new wavefield analysis tools for the characterization of Lamb waves propagating in anisotropic plates are presented.

1.2 Contributions

The main points investigated and discussed in this Thesis lead to the following contributions:

- A novel SSN for SHM based on multi–sensing technologies, *i.e.* piezoelectric and accelerometers, is presented. The importance of using different types of sensors for improving the reliability and effectiveness of the monitoring assessment is demonstrated by two experimental setups. In the first one, an aluminium cantilever beam is characterized by exploiting data from both accelerometers and piezo sensors, comparing the performance of the two technologies. It has been demonstrated that the capability of the multi sensing combined approach enriches the frequency insight for a more reliable and complete modal inspection. Consequently, low–cost piezo sensors can be used alongside traditional accelerometers to characterize the modal response of structures undergoing flexural vibrations. In the second one, a supported beam was instrumented. To compensate intrinsic piezoelectric non idealities which affect the derivation of modal shapes, a tuning based on merging data from accelerome-

ters is implemented. Thus, a complete damage detection and localization strategy was successfully performed.

- Innovative signal processing techniques for Ultrasonic NDT inspection are introduced. In particular, two main methods, referred to as Delay Multiply and Sum (DMAS) and Double-Stage Delay Multiply and Sum (DS-DMAS) are presented in order to improve the performance of conventional Delay and Sum in terms of image resolution and contrast. The proposed methods are validated and characterized by mainly using a freely available online guided waves dataset (`http://openguidedwaves.de/`), where pitch–catch measurements from a Carbon Fiber Reinforced Plate are collected. Experimental results show a clear improvement w.r.t. DAS approach quantified by different metrics, such as contrast–to–noise ratio, peak signal to noise ratio or contrast ratio. In particular, DS-DMAS shows a marked noise reduction and artefacts suppression capabilities which enhances the localization. To further improve the method, a filtering technique addressed as Fresnel Zone Filtering is presented. In such a way, the beamforming partial sums are restricted in a physical way to the area around the scattering point. Nevertheless, such methods are strongly dependant on the precision of the group velocity estimation of Lamb waves. In anisotropic materials, where the propagation properties change for the different directions, very few experimental methods exist to address group velocity extraction. The last contribution of this Thesis is related to this issue.

- New wavefield analysis tools for Lamb waves characterization are introduced. In particular, the experimental extraction of dispersion curves in anisotropic plates by means of scanning laser Doppler vibrometer is

addressed to tackle intrinsic limits of theoretical models where material inaccuracies and non-idealities cannot be easily considered. By exploiting a three dimensional analysis, the polar representation of wavenumber, phase and group velocity at the excitation frequency are extracted, enabling a direction dependant inspection. For such a goal, two methods were studied. The former is based on a image segmentation technique called Distance Regularized Level Set Evolution (DRLSE), which permits the extraction of the wavenumber profile in the k–space of the wavefield. The latter, instead, is based on compressive sensing by exploiting the sparse representation of the wavefield in the 2D wavenumber domain. Both the methods are validated and characterized in three different anisotropic plates with different properties.

1.3 Organization

This manuscript is subdivided as follows. In chapter 2 a brief overview on SHM and NDT techniques is presented. SSNs role in SHM is introduced, highlighting their importance for low–cost, high performance monitoring approaches. Then, in chapter 3, a modal analysis inspection strategy is carried on two different experimental setups by exploiting an innovative heterogeneous smart sensor network in conjunction with data fusion algorithms. In chapter 4, instead, Lamb waves inspection is described, starting from the physical phenomena to the different possible monitoring strategies and sensing technologies. Lamb waves are then experimentally applied in chapters 5 and 6. In particular, chapter 5 focuses on damage localization techniques in both *passive–only* and *active–passive* networks. In the former case, a wavelet–based approach is exploited to determine the direction of arrival of impact–generated Lamb

waves. In the latter, instead, beamforming imaging techniques are characterized and validated on a composite plate. Since the described techniques are strongly dependant on the estimation of the group velocity of the propagating waves, in chapter 6, wavefield analysis tools for dispersion curves extraction in anisotropic plates are presented. Two different approaches are discussed, the former based on image segmentation techniques, the latter on compressive sensing. Finally, conclusions such as future developments are provided in chapter 7.

Chapter 2

Background

Damage detection and characterization are usually carried on by different disciplines, which the most widely known and exploited are Structural Health Monitoring (SHM), Non Destructive Testing (NDT), also known as Non Destructive Evaluation (NDE), and Damage Prognosis (DP).

SHM, according to Balageas et al. [7] definition, aims to give, at every moment during the life of a structure, a diagnosis of the state of the constituent materials, of the different parts, and of the full assembly of these parts constituting the structure as a whole. The process is based on collecting structural response measurements over prolonged periods of time, extracting damage-sensitive features from data. In particular, long-term SHM must periodically provide updates of the structure status by online monitoring - even in harsh environmental conditions - to develop suitable maintenance strategies.

NDT, instead, usually refers to off-line techniques able to determine the severity and the location of potential damages. This kind of approach usually requires the structure to be off-duty, with the exceptions of pressure vessels and rails monitoring [8]. Since SHM and NDT are based on the understanding of the same material properties and physical phenomena which occur in the

material, the main difference lies in the monitoring approach. On one hand, SHM aims to perform continuous monitoring over the entire lifetime of the structure, by exploiting non–invasive sensors technologies to be embedded in the SHM system. On the other hand, NDT is usually carried on with high precision bench instruments by interrupting the duty of the structure.

Finally, DP aims to predict the remaining useful time of a structure by estimating damages and structural conditions evolution through probabilistic models [9]. DP has applications to almost all engineered structures and mechanical systems, with different models depending on the application case. For instance, a stochastic model based on the Gaussian process was used by Liu et al. [10] to determine the remaining useful life of composite structures. The non-homogeneous hidden semi Markov model, instead, was exploited by Eleftheroglou et al. [11] for modelling the damage accumulation of composite structures, subjected to fatigue loading. Chen et al [12], instead, used a mixture proposal particle filter and on-line crack monitoring in a dual crack growth in an aluminium specimen. Although DP is a promising technique for estimating the severity of damages and thus, estimating the remaining structure lifetime, there are many drawbacks which are not been fully addressed so far. Traditional methods, in fact, exploit analytical methods and numerical simulations to characterize the damage evolution from a physical point of view. This kind of analysis is usually restricted to the specific case under evaluation, and it is difficult to migrate the same model to different structures or different damage types. Moreover, several uncertainties might affect the model which can lead to relevant errors in the real–case scenario prediction. Conversely, data–driven approaches can be agnostic to *a–priori* physical phenomena since these methods learn the prognosis model from the experimental data. Nevertheless, online monitoring data is usually not sufficient during the early crack

growth stage and off–stage learning requires a huge amount of data in different operational conditions, which is not trivial to obtain.

2.1 NDT and SHM methods

NDT methods permit the materials or components examination without compromising their serviceability and future usefulness. In particular, NDT allows the detection, localization, measurement and evaluation of different types of damages, leaks, and discontinuities. Thus, it enables the characterization of integrity, properties and composition of the structure, such as the measurement of geometrical characteristics. Many standard practices are published including ASME, ASTM, BS, and ABS (*e.g.* ASTM E1316 [13]). In particular, a wide range of different inspection techniques exists, for addressing many different types of structures and damages, such as Acoustic Emission (AE), X–radiology, vibration analysis, Eddy currents inspection, ultrasonic testing, and others. In the following, a brief overview of the principles and applications of the main NDT methods is provided.

2.1.1 Acoustic Emission

AE exploits elastic waves which are generated in a structure by discontinuities formation, *i.e.* cracks, delaminations, corrosion, etc., and then propagate through the material. By means of suitable piezoelectric sensors and acquisition systems, AE can be recorded and characterized [14]. AE is widely exploited in many different application fields due to the possibility to apply the technique to several different materials, such as alloy (aluminium [15], iron [16], steel [17], copper [18], etc), fiber-reinforced composites [19], concrete [20], and wood [21]. Some application examples can be mentioned, such as bridge mon-

itoring [22], pressure vessels [23] and tanks [24], aircrafts [25], wind turbine blades [26] and others [27]. Each specific application field can exploit suitable signal processing techniques. In particular, signal features such as amplitude, energy, rise time, duration, and counts can provide qualitative and quantitative information about the damage event which created the record. Recently, more complex algorithms have been introduced to address complex structures analysis and damage discrimination, such as classification algorithms [28], Artificial Neural Network (ANN) [29], auto regressive modelling [30], principal component analysis [31] and supervised and unsupervised classification techniques for damage diagnosis and defect distinction [32, 33].

2.1.2 X–Ray

X–ray inspection is based on short wavelength electromagnetic radiations which are a penetrating form of high-energy electromagnetic radiation. Thus, a shadow graph image of the material under test can be obtained. The main principle is that the denser the material, the longer the path length and the higher the X-ray absorption, the more the X-ray radiations is attenuated while it passes through the test object toward an X-ray detector [34]. This relationship can be expressed by the Beer–Lambert law:

$$ln(\frac{I_0}{I}) = \int \mu(x, y, z)\, dl \tag{2.1}$$

where I is the intensity of the transmitted X beam, I_0 is the incident beam intensity and $\mu(x, y, z)$ is the attenuation coefficient at point (x, y, z) along the ray path. Nowadays, accurate inspections by X–rays can be performed using micro Computer Tomography (uCT) and X-ray Computed Laminography (XCL) which enable micro–scale monitoring. In general, tomography is a very powerful tool to characterise with high accuracy structures and compo-

nents. Anyway, the method is quite expensive and features some limitations, such as component size limitations, attenuation contrast issues and in–situ monitoring difficulties. In particular, Garcea et al. [35] demonstrated that the samples must be no larger than 1000–2000 times the smallest feature size, which disables the inspection of large structures. Moreover, in composite materials where the attenuation contrast between carbon fibres and resin is low, the characterization of the material porosity, such as fibre architecture or damages inspection is challenging. Usually, uCT is exploited in such application cases, due to the better resolution achievable. Finally, it's worthy to address the difficulties to perform X–ray inspection for *in-situ* monitoring. In fact, the requirements of mounting test rigs within laboratory X-ray CT systems are extremely strict. Test object position, illumination, synchronization and other aspects must be designed very accurately to obtain satisfactory measurements results [36–38].

2.1.3 Vibration analysis

NDT methods can be grouped into two main categories: local and global. In the former, techniques such as AE and X–ray can be pointed. In particular, these techniques can detect damage in a restricted area or portion of the entire structure where the damage is supposed to exist. This is due to the intrinsic behaviour and characteristics of the NDT. For instance, X–ray is limited by component size limitations, and AE is limited by the attenuation in the propagation path of the stress waves. In the latter category, instead, vibration based damage identification can be addressed. In particular, the main idea is that structural changes induced by damages lead to modifications in the physical properties of the material, such as mass, damping, and stiffness, which can be detected by analysing the modal properties of the structure itself. In particu-

lar, the conventional modal analysis relies on the characterization of vibration signals in both the time domain and frequency domain, where modal information can be extracted such as natural frequencies, modal damping, and mode shapes. Then, by comparing the structural signature with the one extracted when the structure was undamaged, it is possible to evaluate and locate the damage. Parameters can be synthesised, such as the Modal Assurance Criterion (MAC) or the Coordinate MAC Damage (COMAC) [39]. By using both frequency analysis and modal shapes, local damages can be identified since not only global information but also local is exploited for the structural analysis. Capecchi et al. [40] investigated the damage identification capabilities in a parabolic arch by exploiting natural frequencies, modal shapes and curvatures. Khiem et al. [41], instead, addressed the problem of multiple crack identification for beam–like structures from a natural vibration mode following the same principle. Furthermore, many signal processing techniques have been developed. Finite Element Method (FEM) model and iterative algorithms are presented in [42] for implementing FE model updating algorithm to regenerate baselines of frequencies and mode shapes. A genetic algorithm in conjunction with pattern search was used by Ghodrati et al. [43] to detect and estimate damage in plates. An Artificial Neural Network (ANN), instead, was exploited by Neves et al. [44] to detect damages in bridges without the need of *a-priori* model. Moreover, other methods such as machine learning [45], Bayesian classification [46], sparse Bayesian learning [47], unsupervised learning [48] and artificial bee colony algorithms [49] can be mentioned.

2.1.4 Eddy currents and Electromagnetic inspection

Electromagnetic sensors exploit electromagnetic induction. In particular, if a time–varying current passes through an excitation coil, an electromagnetic

field will be created. Following Faraday's Law, if an electrically conductive material is in the proximity of this electromagnetic field, an Eddie Currents (EC) is induced in the material [50]. By analysing the induced EC, information can be extracted. Thus, Eddy currents can be exploited for conductive materials NDT. In particular, EC NDT is based on AC–driven excitation coil which induces the current via electromagnetic coupling. In turn, the circulation of the eddy current induces a secondary magnetic field. If the electrical conductivity, magnetic permeability or thickness of the sample change, the secondary magnetic field will change accordingly, thus enabling multiple different types of inspections. For instance, ECs have been used for crack detection [51], material and coating thickness measurement [52], conductivity measurement for material identification [53], heat damage detection, case depth determination, and heat treatment monitoring [54]. Nevertheless, conventional EC testing is based on a single frequency excitation which does not permit the detection of sub–surface damages. To tackle this limitation, several solutions have been introduced in the scientific literature. A multi–frequency EC testing has been presented in [55], where different excitation frequencies are excited in a row. Pulsed Eddie Currents (PEC), instead, is considered one of the most effective methods in multilayer structures [56]. Albidin et al. [57] demonstrated the effectiveness of the method for the evaluation of the integrity of rivet joints. Hosseini and Lakis [58], instead, used PEC data in time-frequency domain. In particular, by exploiting maximum variances of Principal Component Analysis (PCA) they automatically determined corrosion in thin multi-layer structures. Finally, it's worthy to mention the Pulsed Eddie Currents Tomography (PECT), which enables imaging of conductive structures without scanning. The two main PECTs techniques are the ones based on induction, which is stimulated by short bursts of electromagnetic excitation and the ones based

on heat diffusion, which use flash thermography. Examples of PECT can be found in [59–61]

2.1.5 Ultrasonic inspection

Ultrasonic Wave (UW) are stress waves with frequencies ranging from 20 kHz to 10 MHz. UW can travel freely in liquid and solid (bulk wave) or, alternatively, being guided (guided waves), depending on the medium. In the former case, bulk waves have been extensively exploited for NDT purposes for flaws, *i.e.* cracks or inclusions, far beneath the inspection surface. The most simple ultrasonic test which can be performed is the so called *Through-transmission* or *shadow* test, where the inspection is carried on by placing a probe on each of two opposite surfaces of the structure. Then, flaws are detected and measured by exploiting the shadow that they generate in the direct path of the wave. Nevertheless, many different ultrasonic tests have been developed, such as contact testing, immersion testing, air-coupled ultrasonic testing, laser ultrasonic testing, and Electromagnetic Acoustic Transducer (EMAT) [62–65]. Each method is characterized by different sensing elements, *e.g.* piezoelectric transducers, laser or electromagnetic transducer, and different characteristics such as limitations. For instance, air–coupled ultrasonic testing suffers from low efficiency if a large impedance difference exist [66]. All the methods above are able to detect and characterize the crack size in the material under test. In particular, ultrasonic sizing techniques can be divided into four main categories: Amplitude [67], temporal [68], imaging [69] and inversion [70] techniques. A comprehensive review of ultrasonic bulk waves inspection, such as ultrasonic sizing techniques can be found in [71]. Guided waves inspection, instead, is widely exploited for plate–like structures, where Lamb waves are mostly involved. An in–depth description of guided Lamb waves principles,

equations and applications is provided in chapter 4.

2.2 SHM Smart Sensor Networks

Disclaimer: the following section was partially published by ©2020 IEEE [AP1]

Usually, an SHM system is composed of four main actors: the sensing elements, data acquisition/transmission sub–system, data management/control module and structure performance evaluation system [39]. The installation of such real–time, long term systems is usually not trivial, due to the large number of sensors required which increase the monitoring complexity and cost. At the same time, the SHM system is supposed to satisfy strict requirements in terms of accuracy and reliability for the safety of the entire structure. For such reasons, SHM is still suffering to be widely used in industrial and civil real application scenarios where these technologies are only partially exploited. The cost reduction of the devices employed, without losing accuracy and reliability, is fundamental in order to achieve a widespread diffusion of SHM techniques. In particular, low–cost electronic devices which feature embedded signal processing capabilities, low power consumption, small size and small weight are preferable in comparison with conventional SHM instruments, made of expensive transducers and data acquisition systems. Thus, in the last few years, different kinds of Smart Sensor Network (SSN) are rising, tackling the limits of conventional SHM instruments. While wired smart sensor networks, such as [72], feature more security against external hacks, a robust transmission synchronization and the possibility to exploit a stable wired power supply, Wireless Smart Sensor Network (WSSN) are the most promising systems for SHM applications because they don't require long cables leading a significant cost reduction and an easier installation procedure of the network

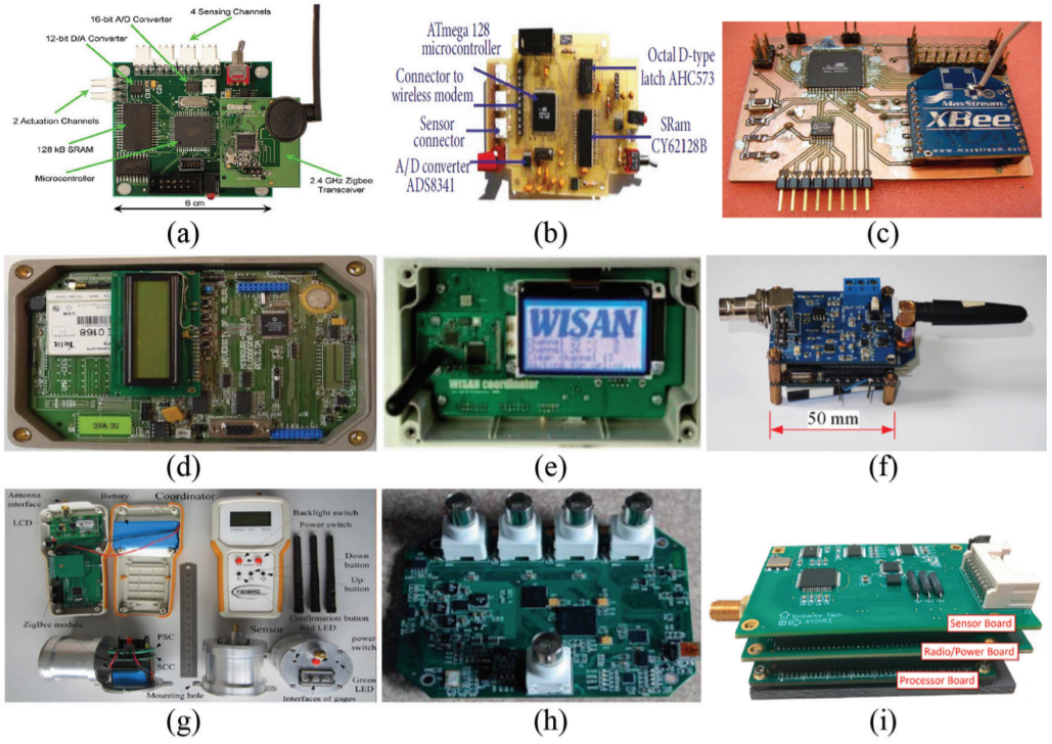

Figure 2.1: Academic wireless sensors prototypes [74]: (a) Narada wireless prototype [75], (b) PCB two-layer circuit board [76], (c) Thinner wireless sensor node [77], (d) SmartBrick V2.0 [78], (e) WISAN coordinator [79], (f) WSNG2 Prototype [80], (g) PWSMS portable wireless system [81], (h) AEPod Prototype V1.0. [82], and (i) Xnode smart sensor [83].

on the structure under test. Moreover, the implementation of WSSNs by the Internet of Things (IoT) paradigm [73], will probably lead to a new Internet of Structures (IoS) paradigm in which real–time and continuous monitoring will strictly interact with IoT devices, such as temperature sensor, humidity sensor, GPS etc. Due to the limited cost and miniaturization required for WSSNs devices, it is important to consider even limits and constraints that such features lead. Usually, the most important constraint in WSSN is the power consumption of the nodes, which are typically supplied by batteries or

by energy harvesting solutions. The energy–saving capability of the network, and thus its flexibility is a fundamental metrics to consider. At first, different kinds of topologies exist for WSSN. Usually, the choice of one topology among others is related to the specific application case. Shrestha et al. [84] discussed the various WSSNs topologies performance by comparing performance criteria such reliability, energy–efficiency, network life, scalability, self–organizing capability and data latency. Star topologies are one of the simplest and most common forms of communication topology. Unfortunately, because of the direct connection between each element of the network and the central unit, or sink, the energy–saving techniques which can be exploited for such kind of architecture are limited. In fact, it has been demonstrated that communication is the most energy–consuming activity performed by sensor nodes, and typically one–bit transmission requires around 100 to 1000 times more energy in comparison with one instruction processing. Thus, it is fundamental to embed signal processing directly inside the nodes, reducing the amount of data to be transmitted. This is not a trivial task, because the processing capabilities of the nodes are limited by the hardware architecture and technology constraints, such as memory space, Floating Point Unit (FPU) operation capabilities, clock speed, Microcontroller Unit (MCU) performance. Thus, an accurate feasibility analysis and performance study must be performed in order to determine if a specific signal processing is actually beneficial for the sensor network. In the case of mesh WSSN and Clustered Hierarchical Configurations there is more flexibility and different energy–saving techniques can be exploited. In the former, the intra–node communication can be used to distribute the computational effort to multiple devices, meanwhile, in the latter, a Cluster Head (CH) with advanced signal processing capabilities can be exploited in order to perform more complex signal processing reducing the effort of the nodes.

Thus, it's evident that the right strategy to adopt depends not only on the pure sensor node capabilities but even on the right topology and Network architecture, which has to be analysed on the specific application case. For a sake of completeness, an exhaustive overview of WSSNs technologies, hardware implementations and SHM applications is presented by Abdulkarem et al. [74]. In Figure 2.1 some of the WSSNs implemented in the last years by academic research groups are shown. A general trend can be observed by analysing the existing solutions. In fact, WSSNs and SSNs are usually designed to acquire different types of signals from different sensing elements. In such a way, the SHM inspection is more robust, reliable and complete. The idea behind Heterogeneous Sensor Network (HSN) is to enable advanced signal processing, which might be on board or off boards, correlating different types of information [AP2]. This kind of approach tackles the single inspection limits, enabling data cross–validation and prognosis.

In the next chapter, a lightweight, heterogeneous sensor network, consisting of strictly synchronized nodes based on low–cost Lead Zirconate Titanate ($PbZr_xTi_{1-x}O_3$, or PZT) transducers and triaxial Micro Electro-Mechanical Systems (MEMS) Accelerometer (ACC) is presented. The multi–sensor network is validated and investigated by analysing the modal characteristic of defective structures. A numerical model built on closed analytic formulae was developed to investigate the adherence of experimentally extracted modal parameters to the predicted ones. A dedicated processing flow comprising a PZT tuning step was specifically implemented to recover modal shapes. Damage-sensitive parameters were finally employed for fault detection in presence of structurally perturbed conditions.

Chapter 3

Heterogeneous Sensor Networks for SHM

Disclaimer: the following section was previously published by ©2020 IEEE [AP1] and ©2019 IEEE [AP2]

Modern SHM systems are typically constituted by a multitude of sensor nodes. Such devices should be based on low–cost and low–power solutions both to ease the deployment of progressively denser sensor networks and to be compatible with a permanent installation. Thus, real–time monitoring, maintenance costs reductions and safety increase are enabled. In civil infrastructures, vibrational analysis based on Operational Modal Analysis (OMA) is one of the most effective and reliable tools to assess the integrity of the structures [85], by observing the structural vibration characteristics which change with respect to baseline healthy values [86, 87]. In OMA, natural frequencies are commonly tracked to detect global damages, while mode shapes can be used for defect localization [88]. To achieve good localization capabilities, dense sensor networks must be implemented. However, the high cost of such SHM networks

inhibits their widespread implementation. Nowadays, rapid advances in signal processing and sensor technology allow for the implementation of smart maintenance schemes for conventional buildings and infrastructures [AP3].

In this framework, this chapter presents a sensor network that is based on either MEMS accelerometers and cost–effective piezoelectric devices to extract strictly synchronized modal parameters. In literature, many research studies validated MEMS for vibrational analysis. For instance, Testoni et al. [89] described low power and low–cost smart sensor network based on three-axial MEMS with local data processing and data-to-cloud capabilities. Bedon et al. [90], instead, presented original self–made MEMS sensor prototypes. The prototype has been then validated in preliminary laboratory tests, such as shaking table experiments and noise level measurements. Nevertheless, most types of MEMS accelerometers can not perform wideband analysis due to frequency range limitations. Conversely, piezoelectric (PZT) transducer technology is suitable to work in the range of up to hundreds of kHz or more. For such a reason, PZT-based modal analysis can be successfully exploited when the frequencies of interests are usually up to and higher than 10 kHz [91]. Contrarily, in the low-frequency range, down to and lower than 10 Hz, PZTs are scarcely exploited. This is mostly due to the fact that in this frequency range accelerometers are classically understood to be more reliable than PZT transducers. Thus, in this chapter, the fusion of these two technologies (PZT transducers and MEMS accelerometers) is presented. It can be demonstrated that the exploitation of hybrid, multiple sensing elements in smart sensor networks is beneficial for continuous SHM applications in the low–frequency regime in several application fields, such as civil or industrial infrastructures [92, 93]. The performances of the two sensing technologies are evaluated in two different setups, to assess the reliability in the estimation of modal features even in

presence of potential damages. Moreover, the consistency of the obtained results demonstrates the potential of a more compact and affordable monitoring system exploiting piezoelectric–driven modal analysis.

3.1 Smart Sensor Network Technology

Disclaimer: the following section was previously published by ©2020 IEEE [AP1]

Comparisons of different research prototypes and commercial MEMS acceleration sensors are presented in [94, 95]. An exhaustive literary survey on the most advanced sensing solutions currently available for vibration analysis is provided by [96]. Nevertheless, very few analyses have been conducted on systems based on disc-shaped piezoceramic patches (discs) in the vibrational field. An interesting byproduct of using PZT discs is the possibility to simultaneously perform OMA and acoustic emission testing [97]. This evaluation strategy is of primary importance in the integrity assessment of metallic or composite structures, either intended for civil and construction engineering (e.g. bridges, towers, buildings) [92] or industrial applications (e.g. rotating motors and hydraulic pumps [93], wind turbines [98, 99]), where the nominal vibration behaviour co-exists with important acoustic phenomena occurring as a consequence of structural deterioration (delaminations, soldering, etc) and external agents (corrosion, etc). The network discussed in this section is based on a compact sensor–near electronics, capable of data merging and feature extraction thanks to the embedded Digital Signal Processing (DSP) functionalities. The architecture of the proposed network is based on two main elements: two compact Sensor Node (SN), and a network interface, also called gateway, which can coordinate up to 64 sensor nodes at a time. The former SN is connected up to three PZT discs, while the latter incorporates

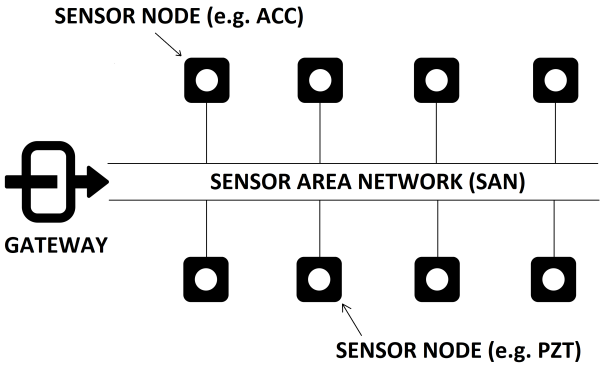

Figure 3.1: A schematic representation of the developed up-scalable and heterogeneous sensor network architecture. ACC and piezoelectric (PZT) sensor nodes can be simultaneously exploited under the orchestration of a gateway network interface [AP1].

a triaxial LSM6DSL iNEMO MEMS accelerometer accessed by means of a dedicated SPI interface. A comprehensive description of these elements can be found in [100] [AP4] and [72]. Nevertheless, a fast description is provided here below. Moreover, a sketch of the sensor network architecture is depicted in Fig. 3.1.

All these devices are joined in a daisy–chain fashion by means of a multidrop Sensor Area Network (SAN) bus, which exploits Data over Power (DoP) communication [89] based on the EIA RS–485 standard. A wired connection was preferred over a wireless one in order to grant the possibility to continuously acquire data from the structure at the highest possible data–rate; this choice also led to the design of lighter nodes, which did not require the presence of a battery. The communication protocol can be used effectively over long distances and in electrically noisy environments, which are common in many application fields. Meaningful information is transmitted to a PC through the gateway. A maximum effective data–rate of 200 kbps was selected, enough to

accommodate up to twelve 16-bit data channels simultaneously acquiring at 1 ksps. Data are transmitted sequentially, in packets, by exploiting a proprietary lossless encoding technique. The reception of each data packet must be acknowledged by the receiver before the next packet is sent by the transmitter. During acquisition, signals are collected simultaneously by each sensor node. A unique time-stamp is provided by means of an internal 32 bit high–speed hardware counter, clocked at 64 MHz; once every hour a 32 bit low–speed software counter is updated. According to the core microcontroller manufacturer [101], the cycle–to–cycle jitter of the internal high speed clock system is 300 ps whereas its accuracy for soldered parts working in the $-10\,^{\circ}\mathrm{C}$ to $85\,^{\circ}\mathrm{C}$ temperature range is $-1.9\,\%$ to $2.3\,\%$ with respect to the nominal value. Measurements taken on the implemented sensor network showed cycle–to–cycle jitter [102] of 239.5 ps, a minimum deviation of -0.069% and a maximum deviation of 0.026% over a time period of 2400 s. These results are compatible with the figure of merit reported by the manufacturer. Synchronization among the different nodes of the network is an essential requirement in order to perform data merging, data comparison and mixed–signal processing during the post–processing phase [103]. The synchronisation algorithm exploited in this work is based on a software implementation of the classical three-way handshake adopted by the RFC 793 Transmission Control Protocol [104]. First, the gateway sends a synchronization command addressed to a single node; the receiving node responds with a similar command, addressed to the gateway; finally the gateway sends an acknowledge message to the sensor node. The first two steps allow the gateway to computing the Round Trip Time (RTT), whereas the last two steps allow the sensor node to compute the RTT. Several factors contribute to the RTT: the messages encoding/decoding time, the messages transmission time, the delays between the messages transmission

and reception at the electrical level, and the messages processing time. The messages transmission time is already known to the gateway and the sensor nodes, since messages length and data rate are known a-priori, and do not change over time; the sum of remaining terms, called residual RTT, conversely can change over time and must be estimated. The mean of the residual RTT of the proposed network, estimated from 1000 observations, is 33 µs with a standard deviation of 160 ns and is dominated by large by the messages encoding/decoding time: as such, RTT/2 is considered a good approximation of the propagation delay at the software level. Once each node in the network knows its own Round Trip Time (RTT_i), the gateway issues a broadcast synchronization command containing its local time T_0: following this last command, each sensor node in the network sets its internal counters to $T_0 + RTT_i/2$. Due to clocks' drift, in absence of periodic transmission of the broadcast synchronization command, the maximum divergence between the sensor nodes' clocks in the proposed network over 2400 s of observations was 2.254 s. This value was reduced to 4.7 ms by issuing the synchronization command once per acquisition (i.e. 5 s), which is acceptable for vibration-based structural inspection [76]. The scalability and high flexibility of the network allow the user to independently handle the configuration of the parameters related to each sensor node. This is crucial for the optimization of the system according to each experimental case–study, while maintaining the same hardware architecture. Similarly, it is also possible to completely reconfigure the monitoring system during the life-cycle of the structure, by changing the network cardinality or the acquisition parameters.

3.2 Modal parameter extraction

Natural frequencies of vibration and modal shapes can be addressed as modal parameters. Usually, these parameters change according to structural evolution, enabling dynamic identification [105]. In particular, the Power Spectral Density (PSD) of vibration signals, which describes the signal distribution of power in the frequency domain, is useful for characterizing structural integrity. PSD estimators can be divided into two main groups: Autoregressive (AR) based methods and non–parametric procedures (such as periodogram and Welch's evaluation) [106]. The former methods are characterized on the dark side by high computational cost. On the bright side, instead, this strategy features the capability to effectively extract narrowband spectral peaks, which is suitable for the typical frequency response of vibrating structures [105]. The latter, instead, usually assume that the structural response can be modelled as the output of an equivalent all–pole Infinite Impulse Response (IIR) filter. Thus, let's define $s(t)$ as the time–domain structural response in the following form:

$$s(t) = \sum_{i=1}^{n} \theta_i s(t - iT) + \epsilon(t) \tag{3.1}$$

where each signal sample (with sample period of T) can be modelled as the linear combination of the n previous values of the observed process, summed to a zero–mean white noise signal $\epsilon(t)$ as a driving source. The set of parameters $\theta = [\theta_1 ... \theta_n]$, instead, refer to the filter bank. By determining θ and the noise variance σ_ϵ^2, the AR model of order n can be solved. In particular, in the frequency domain, the power spectrum $S_x(f)$ can be directly addressed as

$$S_x(f) = \frac{\sigma_\epsilon^2}{|1 - \sum_{i=1}^{N} \theta_i e^{-i2\pi f_i}|^2} \tag{3.2}$$

A variant of the conventional AR parametric method was adopted for the pre-

sented work: the AR + Noise approach [107]. AR main approach is to consider the noise as the only source to describe the different causes for misalignment between the model and the data. In AR + Noise method, instead, an additive observation error is introduced in the AR model output. This approach outperforms conventional AR strategies by exploiting combined feedback–feedforward prediction model which ensures the congruence of the obtained solution with the second–order statistics of the noisy data and with the cost of a negligible increase in the computational complexity [108]. In particular, the main effort in the algorithm is the eigen decomposition of the predicted signal's autocorrelation matrix. Then, a convex optimization problem is performed to obtain the optimal set of model parameters compatible with the second order characteristics of the noisy input signal [109]. Finally, it's worthy to notice that the harmonic energy of vibrating structures decreases w.r.t. the frequency. Thus, high-order modes are usually affected by low Signal-to-Noise Ratio (SNR), requiring *ad–hoc* signal processing. For instance, the Frequency Domain Decomposition (FDD) technique [89] can be employed due to its established effectiveness in presence of noisy vibration data [110].

3.3 Multi-type OMA of a cantilever beam

In this section, a first case study is presented. In particular, a lightweight aluminium beam fixed at one end was sensorized with both one PZT cluster made of three closely–located active areas and one triaxial MEMS ACC. The PZT cluster and the MEMS were placed in the same vertical position but

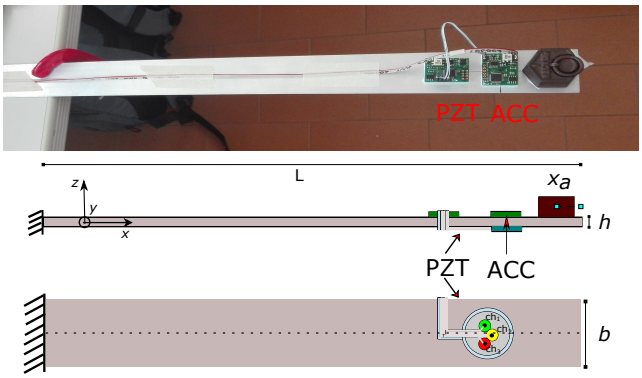

Figure 3.2: Experimental setup comprising one PZT sensor node and a tri-axial MEMS accelerometer (ACC) installed on a cantilever beam [AP2]

on opposite faces of the beam. The beam features 420 mm of length, 40 mm of depth and 1.98 mm of thickness. Moreover, the beam is characterized by density $\rho = 2700\,{}^{kg}/_{m^3}$ and Young modulus $E = 70$ GPa. A mass of 100 g of weight has been attached at the free end of the beam to permit the natural oscillation of the cantilever. The centre of gravity of the additional mass has been chosen to be exactly aligned on the mid–depth, $xA = 15$ mm distant from the longitudinal border. For sake of clarity, the experimental setup is shown in Figure 3.2.

The theoretical modes of vibration were extracted by a numerical first–order model of the cantilever beam. In particular, the first four frequencies $f_1 = 3.85$ Hz, $f_2 = 36.50$ Hz, $f_3 = 107.75$ Hz, $f_4 = 204.93$ Hz were estimated. The vertical acceleration component a_z is discussed in this analysis since it is predominant in the cantilever configuration. The a_z response such as the piezo signals are shown in Figure 3.3. It can be observed that the sinusoidal signals of the two transducers are in phase and consistent during the entire time window depicted. Thus, their frequency response is identical. In Fig. 3.3, instead, the normalized time signals of PZT and the derivative of the nor-

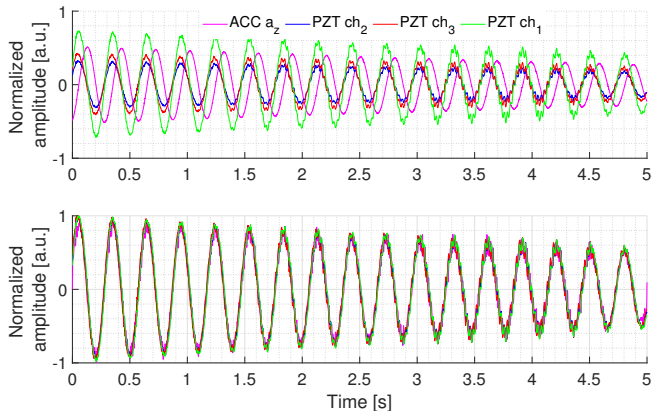

Figure 3.3: Comparison between PZT and ACC acquisitions: original signals (top) and normalized acceleration time-derivative superimposed to normalized PZT signals (bottom) [AP1]

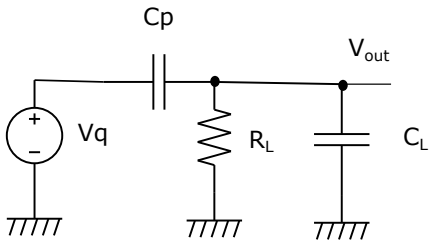

Figure 3.4: First order electrical model of a PZT sensor [AP2].

malized time signal of ACC are plotted revealing a perfect overlap, and thus a strict relationship between the two physical dimensions. In fact, from one side strain is proportional to the second order derivative w.r.t. space of the orthogonal displacement. On the other side, acceleration is the second order derivative w.r.t. time of the displacements. Since the voltage acquired by the PZT sensor node is caused by the deformation of the beam which effect is a charge redistribution, piezo voltage and strain are linearly related. Thus, a linear dependency exists also between signals measured by PZT and ACC nodes, respectively. In particular, to better understand how these dimensions

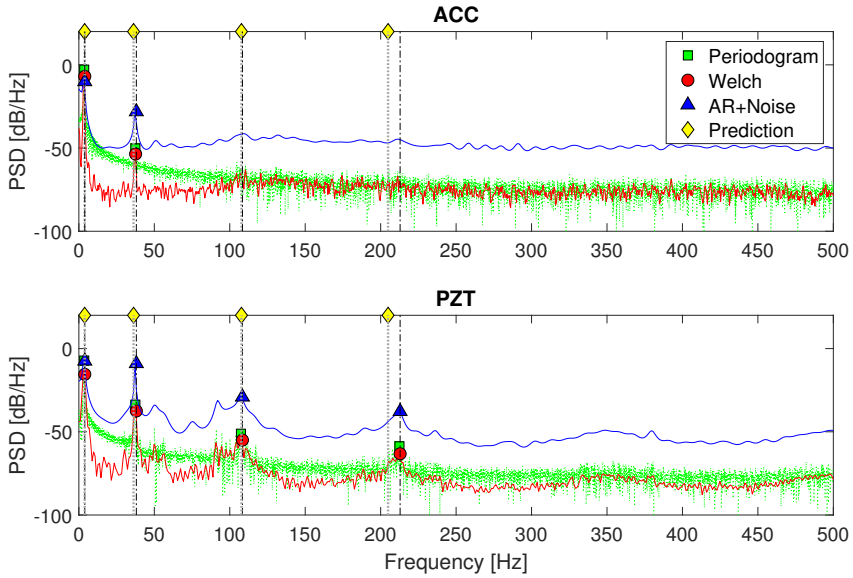

Figure 3.5: Comparison between spectral trend of a_z acceleration signal (top) and ch_1 PZT sensor (bottom) computed with different processing techniques [AP1].

are related, a few considerations about the PZT model can be addressed. The first order electrical PZT model is depicted in Fig. 3.4. In particular, C_P is the piezoelectric capacitance, V_{out} is the measured voltage at the PZT electrodes, while C_L and R_L are the load capacitor and resistor, respectively. The input–output voltage transfer function of the circuit can be written as:

$$H(s) = \frac{V_{out}(s)}{V_q(s)} = \frac{sR_LC_p}{1 + sR_L(C_L + C_p)} \tag{3.3}$$

Assuming that $\omega \ll 1/[R_L(C_L + C_p)]$, where ω is the vibration frequency, the expression can be simplified as follows:

$$H(s) = sR_LC_p \tag{3.4}$$

which acts as a derivative block on V_q. Thus, the signal measured by the PZT nodes is proportional to the first derivative of the strain, and then, to the

first derivative of the acceleration measured by the ACC node. In conclusion, these considerations demonstrate that these devices register different physical quantities relative to the same vibrating behaviour. Then, the vibration analysis in the frequency domain has been addressed. The PSD was estimated through different processing techniques. The resulting spectra are depicted in Fig. 3.5. It is worthy to notice that the spectral peaks are consistent between PZT/ACC signals and predictions. This demonstrates the capabilities of PZT disks to capture the frequency signature of the vibration of the beam at very low frequencies, *i.e.* below a few tens of Hertz. Moreover, the frequency content above 100 Hz has been successfully detected only by PZT sensor node, although the the ACC bandwidth is nominally up to 1 kHz. To quantitatively assess the quality of the frequency response of the two sensor nodes, the Peak-to-Noise Ratio (PNR) has been considered as the main metric. In particular, PNR characterizes the difference between the peak amplitude level and the noise floor, related to each identified peak. In the first and second harmonic, the PNR is PNR = 25 dB for all the spectra from both PZT and ACC. Thus, a significant deviation was not found. On the contrary, the PNR value around the third and fourth modes drops from 15 dB and 10 dB to 0 dB while moving from the PZT to the ACC spectral trends. In conclusion, by averaging all the experimentally estimated peaks with AR+Noise, the dominant modes are centered at the following frequencies: $f_1 = 2.93$ Hz, $f_2 = 37.11$ Hz, $f_3 = 104.49$ Hz, $f_4 = 208.98$ Hz.

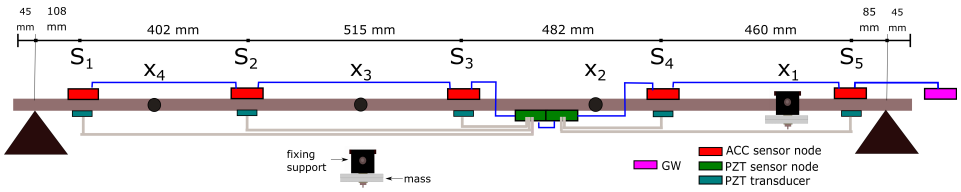

Figure 3.6: Experimental setup deployed on a sensorized supported steel beam. The gateway, the five MEMS accelerometers and the PZT transducers connected to two PZT sensor nodes are depicted as magenta, red, blue and green, respectively. The light–grey wiring lines identify the PZT transducer–to–sensor connections, whereas the blue ones refer to the sensor–to–sensor communication cables. Four different positions x_1, x_2, x_3, x_4 were considered to simulate the presence of crack-like faults by means of hanging masses.

3.4 Damage detection of a simply supported beam

Disclaimer: the following section was previously published by ©2020 IEEE [AP1]

In order to further validate the conjunction of ACC and PZT node technologies in modal analysis applications, another experimental setup was arranged. A supported steel beam characterized by length $L = 2052\,\text{mm}$, cross–section base $b = 60\,\text{mm}$ and $10\,\text{mm}$ height, was sensorized with a double chain of five PZT transducers and as many accelerometers almost equally spaced. As in the previous case, the sensors were attached in the same vertical position but on opposite surfaces. The total weight of the network is $53.1\,\text{g}$, less than 0.54% of the beam mass which weights $9.70\,\text{kg}$. Moreover, the weight of the network is uniformly distributed over the whole beam span. Thus, can be stated that its effects on the dynamic response of the structure is negligible. Damages, *e.g.* cracks or local discontinuities, were mimicked by hanging additional masses of two different weights, *i.e.* $m_A = 988\,\text{g}$ and $m_B = 1754\,\text{g}$, on the beam

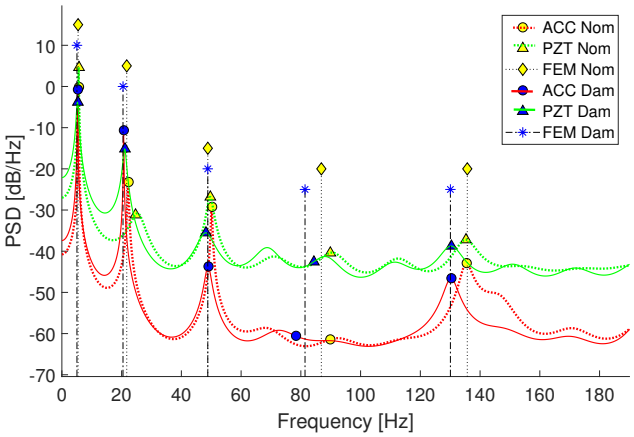

Figure 3.7: Spectral trends. ACC are depicted as red lines/circle markers, while PZT are green lines/triangle markers. Signals in nominal condition, are drawn as dotted lines/blue markers. Conversely, signals in damage condition are solid lines/yellow markers. Data were acquired in correspondence of the mid–span [AP1].

at four different positions: $x_4 = 335\,\text{mm}$, $x_3 = 820\,\text{mm}$, $x_2 = 1353\,\text{mm}$ and $x_1 = 1854\,\text{mm}$ distant from the left edge of the beam. In fact, the effect of the presence of the mass is a perturbation in the natural frequencies which depends on both its weight and placement. In Fig. 3.6 the experimental setup is depicted. Finally, it's worthy to notice that the selected positions of the sensing elements are proximal to the nodal and antinodal values of the first two modes of vibration.

After a preliminary characterization in nominal conditions, eight configurations with simulated damage were tested stimulating the beam in a free position by means of an impact hammer. In all the experiments, 5000 samples were acquired at $f_s = 1\,\text{kHz}$. In such a way, not only the effectiveness of the sensor network to extract modal parameters was validated, but also the possibility to detect a defective condition.

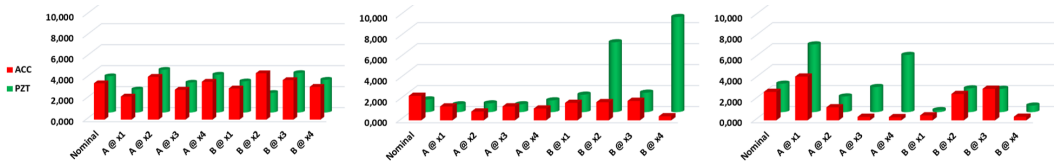

Figure 3.8: From left to right are shown the relative errors between AR–driven experimental estimation and numerical prediction obtained in nominal and damaged conditions of the first, second, and third natural frequency of vibration, respectively [AP1].

Frequency-based assessment

Due to the complexity of the experimental setup, the AR+Noise method with order 60 was exploited to compute signals spectrum. The main issue consisted of the non–ideal beam fixing mechanism which generated undesired harmonics. In Fig. 3.7, the nominal and the altered spectra, *i.e.* when the mass is attached, of the ACC sensors, PZT sensors and simulation expectations are shown. In particular, the PSDs of ACC and PZT nodes are obtained by averaging the responses acquired by the same type of transducers in the same condition. Then, the Finite Element Method was purposely developed to predict the expected modal parameters in all the inspected scenarios. At first, the agreement in the frequency response between ACC and PZT nodes is evident, thus validating the suitability of low–cost piezoelectric sensors in classical OMA–based SHM. Moreover, the frequency deviation from nominal values is coherent with expectations and numerical simulations. A quantitative evaluation is reported in Fig. 3.8. The relative percentage error $E_r^{(i)} = \left|1 - f_e^{(i)}/f_{Model}^{(i)}\right|$ for every vibration component i between the first three experimentally extracted ($f_e^{(i)}$) and numerical modal frequencies ($f_{Model}^{(i)}$) is shown. The non–uniform distribution of the error among the different acceleration components follows the same

pattern in both the adopted sensing technologies. The most noticeable fluctuation can be observed in the third mode, independently from the position or entity of the hanging mass due to the low energy content and thus, low signal–to–noise ratio of this modal component. In general, PZT response quality and precision are competitive over the MEMS accelerometers, demonstrating good performance even at low frequencies. In fact, it's worthy to underline that the error of PZT is averagely below 3.10% and 2.66% respectively for the first and second modes. On the other side, the average errors of ACC sensors are 3.38% and 1.40%. Finally, can be stated that, despite some isolated peaks, concentrated around the most deeply perturbed configurations (e.g. 6% error for the second natural frequency when m_B is in position x_2), the precision of the PZT transducers in detecting the most energetic and low–frequency harmonics outperforms the one obtained from acceleration data.

Modal shape–based assessment

In conventional model–driven SHM scenarios, frequency–based damage metrics alone are recognized to be insufficient to ensure a reliable structural integrity assessment. Thus, the frequency analysis is usually accompanied by the extraction of modal shapes which define the point–wise relationship between the specific pattern of vibration revealed by a modal component [105]. In such a way, external fluctuations such as temperature and humidity variations which might affect the frequency response of the sensors, and thus the accuracy of the analysis, are tackled [111]. The strategy for extracting the modal shapes from PZT sensors is depicted in Fig. 3.9. The final goal is to reconstruct the first three modal shapes for each tested configuration.

At first, because of differences in the amplitude response of the PZT transducers due to intrinsic non–idealities in the sensors' fabrication, wiring and

coupling mechanism, a modal shape *tuning* (or *scaling*) procedure was implemented. The tuning is performed when the structure is in pristine conditions and, subsequently, evaluated for on-condition damage assessment in presence of defective configurations. At first, M acquisitions from ACC and PZT sensor nodes were repeated under nominal dynamic behaviour. Then, the first three modal shape vectors $\mathbf{\Phi}_{ACC}^{(i,mN)} = [\Phi_{1,ACC}^{(i,mN)} \dots \Phi_{P,ACC}^{(i,mN)}]$ and $\mathbf{\Phi}_{PZT}^{(i,mN)} = [\Phi_{1,PZT}^{(i,mN)} \dots \Phi_{P,PZT}^{(i,mN)}]$, $m = 1 \dots M$, for ACC and PZT acquisitions, respectively, were extracted by means of FDD algorithm. During the second step, the PZT tuning was implemented as following. By exploiting a leave–one–out strategy, $M-1$ acquisitions were used to tune the PZTs and the remaining one, which will be addressed as k-*th* data set, was exploited for cross validation. the scaling coefficient $\alpha_{p,PZT}^{(i,kN)}$ for the $i-th$ PZT modal coordinate at the individual sampling position p can be defined as:

$$\alpha_{p,PZT}^{(i,kN)} = \frac{1}{M-1} \sum_{m=1,m\neq k}^{M} \frac{\Phi_{p,ACC}^{(i,mN)}}{\Phi_{p,PZT}^{(i,mN)}} \tag{3.5}$$

The scaling factors were then used to compute the estimated modal shape coordinates $\hat{\Phi}_{PZT}^{(i)}$:

$$\hat{\Phi}_{p,PZT}^{(i,kN)} = \alpha_{p,PZT}^{(i,kN)} \Phi_{p,PZT}^{(i,kN)} \tag{3.6}$$

In particular, the experimental setup relies on $M = 5$ acquisitions from $P = 5$ acceleration and piezoelectric devices on the beam in pristine conditions. Then, 5 different sets of tuning factors were derived, the cardinality of each set being equal to the number of the extracted modes.

The tuning procedure can be validated by computing the Modal Assurance Criterion (MAC) [112], which measures the level of coherence between numerically predicted modal shapes $\mathbf{\Phi}_{Model}^{(i,N)}$ and experimentally scaled PZT modal shapes $\mathbf{\Phi}_{PZT}^{(i,kN)}$ coming from the $k-th$ data–set. The MAC index swings between 0 and 100%, where zero stands for totally inconsistent data, while 100%

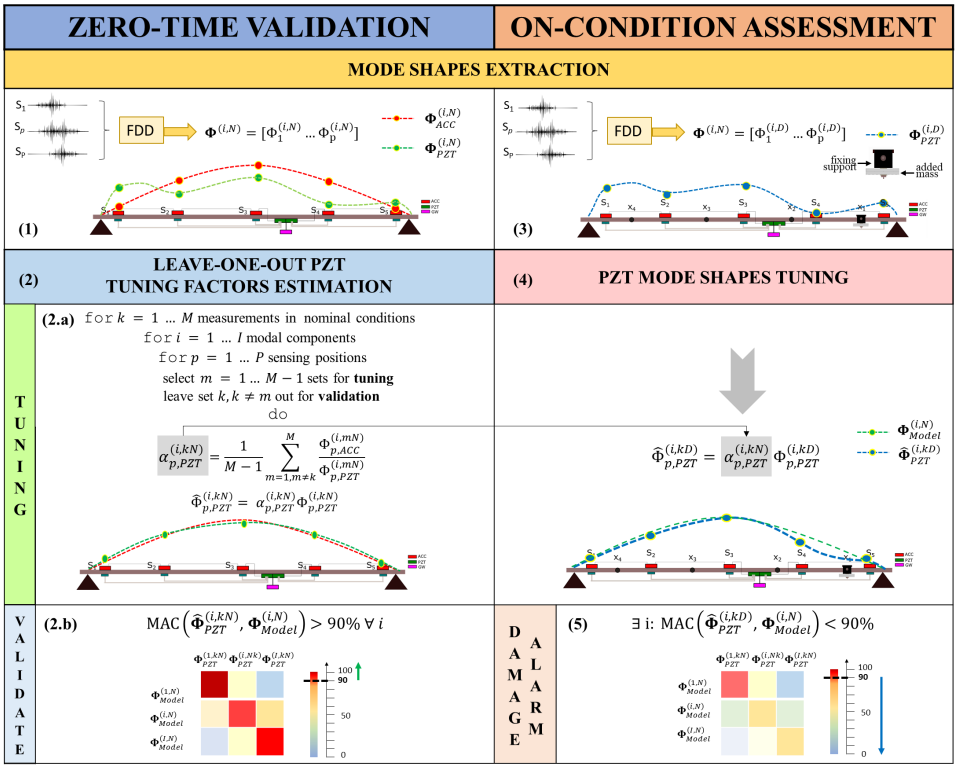

Figure 3.9: Processing steps adopted for PZT–based damage detection purposes. In the left column, the preliminary analysis carried on without the presence of damage. In detail: (1) the extraction of both the ACC and PZT raw modal shape curves, (2.a) the PZT mode shape scaling factors estimation built and (2.b) final structural validation of the reconstructed PZT modal shapes. In the right column, the damage detection processing. In (3) the FDD was used to estimate the modal shapes. Then (step 4) the previously estimated tuning factors are employed to re–scale the currently obtained raw PZT modal shapes; the comparison with reference values (step 5) is performed to notify damage alarms in case of occurrence [AP1].

expresses a perfect modal superimposition. Usually, the percentage threshold of 90% is used to discriminate between healthy (MAC indexes $\geq$ 90%) and defective (MAC indexes $\leq$ 90%) structural behaviour [113]. Table 3.1, the average of the MAC achieved for the five different sets in nominal conditions of tuning factors is shown in the first row. The percentages are consistently above 90%, demonstrating the good performance of the tuning procedure, also considering the low minimal standard deviations reported. Only the third harmonic is below 95%, because higher modal components only comprise a minimal part of the total mechanical energy of the structure, [91].

After the tuning phase, the capability to identify the damage by monitoring the modal shapes extracted from PZT acquisitions was tested. The damage configuration is the same described in the Frequency–based assessment section, and sum up in Fig. 3.9 in steps 3-5. FDD method was used to determine the modal shapes vectors in damaged conditions $\mathbf{\Phi}_{PZT}^{(i,D)} = [\Phi_{1,PZT}^{(i,D)} \dots \Phi_{P,PZT}^{(i,D)}]$ from PZT sensors. Then, the tuning coefficients $\alpha_{p,PZT}^{(i,kN)}$ are applied to compensate PZT non–idealities following Eq.3.6. For instance, In Fig. 3.9 at step (4) the modal shape in damaged condition, depicted as the blue dashed curve, with the mass placed in position $x1$, is superimposed with the nominal one extracted in pristine conditions, depicted as green dashed curve. The deviation around the actual damage position is evident. Finally, the results are further validated by estimating MAC indexes with respect to reference modal values. Table 3.1 reports the mean values $\mu^{(i)}$ and the associated standard deviations $\sigma^{(i)}$ of the MAC related to each set of five modal correlation percentages for the different considered defective conditions. For each case, it is possible to identify at least one mode with MAC correlation degrading below 90%.

Table 3.1: Mean values μ and associated standard deviations σ of MAC values obtained in nominal condition validation and damage detection assessment after applying the proposed PZT modal shapes tuning procedure.

	$\Phi^{(1)}$		$\Phi^{(2)}$		$\Phi^{(3)}$	
	$\mu^{(1)}$	$\sigma^{(1)}$	$\mu^{(2)}$	$\sigma^{(2)}$	$\mu^{(3)}$	$\sigma^{(3)}$
Nominal	96.75	1.33	96.56	2.71	94.40	1.57
A @ x_1	91.23	2.06	76.07	3.60	41.38	3.24
A @ x_2	90.03	2.34	67.78	4.16	73.57	3.28
A @ x_3	83.32	2.60	78.44	2.60	72.24	3.17
A @ x_4	88.14	2.09	66.42	4.10	38.64	11.24
B @ x_1	95.24	0.93	51.32	3.79	49.44	20.72
B @ x_2	75.65	1.89	49.94	1.94	13.96	6.24
B @ x_3	96.49	0.21	54.64	3.08	96.09	1.01
B @ x_4	71.65	2.79	52.04	2.06	90.26	1.92

Chapter 4

Guided Waves in SHM

Guided waves have been studied since the late eighteenth century with Rayleigh studies [114]. During the last century, instead, Lamb [115], Love [116] and Stoneley [117] made the biggest contribution in understanding guided waves physical phenomena. A Guided Wave (GW) is essentially an ultrasonic mechanical wave that propagates through bounded structural media. The nature of the bounded configuration which acts as a waveguide leads to multi–modal, dispersive and attenuated propagation. On the bright side, GWs can travel at large distance, enabling many different application possibilities. Several types of GWs exist [118]. Among them, surface waves propagate on the surface of a structure and, depending on the structural stress and boundary conditions can be listed in different categories. For instance, Rayleigh waves are GWs whose propagation is confined in an elastic half–space. Although Rayleigh waves are not dispersive for uniform materials, their propagation is complex, following an ellipse shape particles movement. Moreover, waves amplitude and velocity might be affected by coupling effects between the propagation surface and a medium surrounding the structure. In general, Rayleigh waves are exploited to detect surface defects [119, 120]. Love waves can be also addressed as surface

waves travelling in layered materials. In particular, Love waves are horizontally polarized shear waves that also exist on the surface. They feature highly dispersive characteristic and high–velocity propagation. Love waves are not usually exploited for damage detection and characterization, with few exceptions such as [121], being more suitable for seismology [122]. Finally, Lamb waves propagate in thin plate–like structures with parallel free boundaries,*i.e.* the top and bottom of the plate [123]. Propagation through curved structures with shallow curvatures is allowed as well. Lamb waves were used for the first time for detecting damage in 1961 by Worlton [124]. Nowadays, they are seen as a prime candidate in damage detection and characterization of damages in composite structures due to their capability to propagate over a long distance even in materials with high attenuation, such as Carbon Fibre Reinforced Plate (CFRP), thus enabling the analysis of large structures [125]. Moreover, Lamb waves can easily detect damages due to their high sensitivity to interference in the propagation path. The thickness of the laminate, instead, can be interrogated by multiple Lamb modes, enabling the possibility to spot internal damages. For such reasons, Lamb waves are widely exploited in many fields, such as automotive, nautical and aerospace for non–destructive testing.

4.1 Lamb waves dispersion curves

Lamb waves are essentially made by the superimposition of longitudinal and shear waves. The resulting pattern can be divided into two main categories. In particular, by observing the wave across the thickness of the plate–like structure, a stationary pattern that features symmetric or anti–symmetric mode w.r.t. a longitudinal symmetry line at half of the thickness can be identified. The symmetric S_n and anti–symmetric A_n modes, where n is the number of

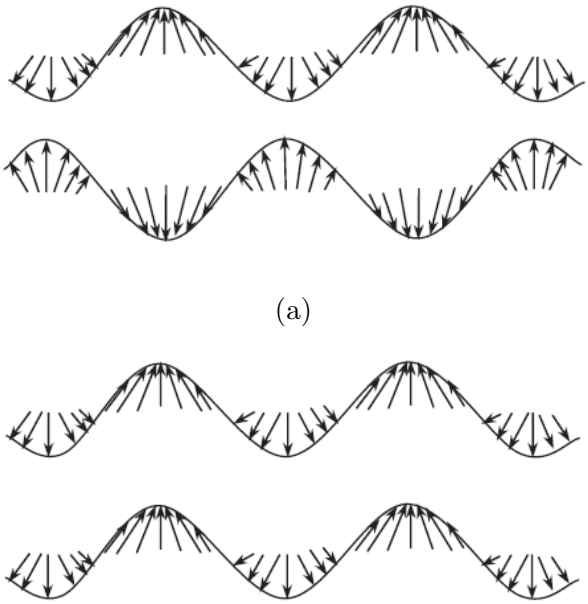

(a)

(b)

Figure 4.1: Symmetric (a) and anti–symmetric (b) modes [123]

inflection points [126], are dispersive. Moreover, at any possible frequency value, multiple modes can exist, making the GWs analysis not trivial. From a mathematical point of view, the analytical dispersion curves for symmetric modes can be written as:

$$\frac{tan(qh)}{tan(ph)} + \frac{4k^2qp}{(k^2-q^2)^2} = 0 \tag{4.1}$$

For the anti–symmetric mode, instead, the dispersion curves can be defined as follows:

$$\frac{tan(qh)}{tan(ph)} + \frac{(k^2-q^2)^2}{4k^2qp} = 0 \tag{4.2}$$

where:

$$p^2 = \frac{\omega^2}{c_L^2} - k^2, \qquad q^2 = \frac{\omega^2}{c_T^2} - k^2, \qquad k = \frac{2\pi}{\lambda} \tag{4.3}$$

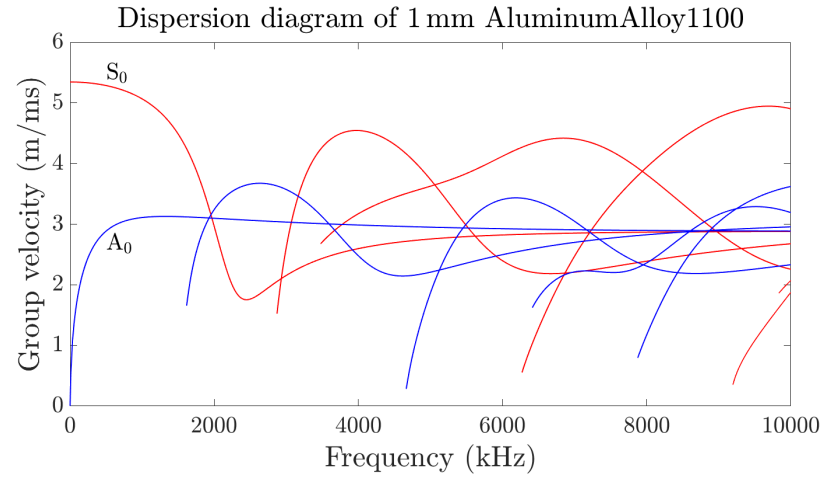

(a)

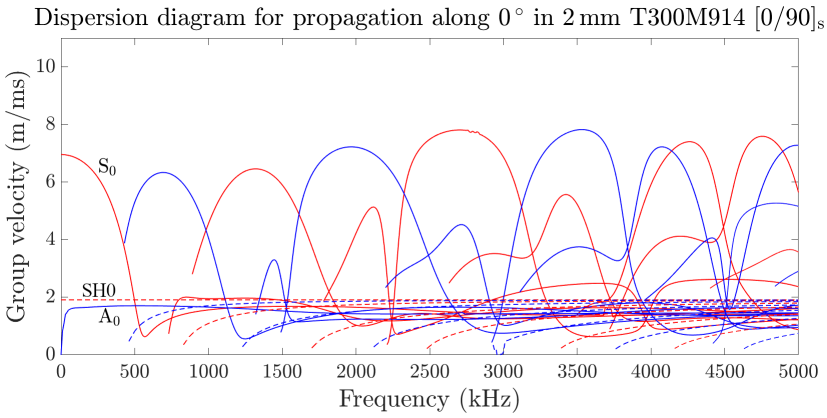

(b)

Figure 4.2: Group velocity dispersion curves for an aluminium Alloy1100 plate (a) and a CFRP T300M914 with layup $[0/90]_s$ (b).

In particular, p and q are placeholder variables, h is the half thickness of the plate, k, λ and ω are the wavenumber, wavelength and angular frequency, respectively. The longitudinal and shear velocities, instead, are addressed as c_L and c_T and defined by the following relationship:

$$c_L = \sqrt{\frac{E(1-\nu)}{\rho(1+\nu)(1-2\nu)}} \tag{4.4}$$

$$c_T = \sqrt{\frac{E}{2\rho(1+\nu)}} \tag{4.5}$$

where E, ν and ρ are the Young's modulus, the Poisson's coefficient and the material density, respectively. The multimodal behaviour of Lamb waves is determined by the multiple roots which solve Eq.4.1 and 4.2. Usually, the analytical dispersion curves equations are solved by exploiting numerical methods. Thus, the relationship between wavenumber, phase velocity and group velocity w.r.t. frequency can be obtained and plotted in dispersion curves diagrams. For instance, in Figure 4.2a the group velocity dispersion curves of an aluminium plate are depicted w.r.t. frequency. In particular, the plate is an aluminium Alloy1100 plate of thickness 1 mm, density $\rho = 2.71\,{}^{kg}/_{\mathrm{cm}^2}$, Poisson's ratio and Young modulus of $\nu = 0\,33$ and $E = 69\,\mathrm{GPa}$, respectively. The $A0$ and $S0$ modes are labelled since usually these modes are predominant, especially at lower frequencies, *i.e.* below 1 MHz, but multiple higher modes can be observed. In the case of plates made of laminates, the propagation is more complex due to the dependence of the waves modes on the laminate layup, the interface conditions and the heterogeneity of the constituents. Moreover, a shear motion perpendicular to the plane of wave travel, which differs from normal vertical shear waves, propagates between layers. This waves mode is addressed as Shear Horizontal (SH) mode, and usually is treated together with Lamb modes although it is a Love wave. In general, SH propagation is not extensively exploited in SHM, although studies in composite plate–like struc-

tures and composite pipe–like structures seem promising [127]. In Figure 4.2b, dispersion curves for a 4 layers CFRP plate T300M914 with layup $[0/90]_s$ are depicted. SH modes are represented as dotted lines, while anti–symmetric and symmetric modes are continuous blue and red lines, respectively. As it can be observed, the multimodal propagation is extremely complex, especially above 500 kHz. In this case, the plate is a transversely isotropic laminate, *i.e.* its physical properties are symmetric about an axis that is normal to a plane of isotropy. In general, anisotropy introduces many propagation phenomena in the composite structure, such as direction–dependent speed and difference between phase and group velocities. Following [128], a composite laminate made of N layers can be mathematically described by means of its displacement field u, by solving the Navier's displacement equations within each layer:

$$\mu^n \nabla^2 u^n + (\lambda^n + \mu^n)\nabla(\nabla \cdot u^n) = \rho^n \frac{\partial^2 u^n}{\partial t^2} \qquad (n = 1, 2, ...N) \tag{4.6}$$

where λ^i, μ^i and ρ are the Lamé constants and the density of the layer i. In general, the solution of the above–mentioned equation is computed by numerical and simulation tools. In particular, four main methods can be addressed: Finite Element Method (FEM), Finite Difference Method (FDM), Semi-Analytical Finite Element (SAFE) and Local Interaction Simulation Approach (LISA). FEM exploits the discretization of the material into small parts to create a mesh. In such a way, Partial Differential Equation (PDE) related to each discretization can be approximated by a numerical model, simplifying the mathematical approach. FEM is widely exploited in both commercial software [129] and research studies [130, 131]. The main idea of FDM, instead, is to substitute PDEs with finite difference equations. Usually, the method is exploited in a regular grid and rectangular shapes [132]. On the other hand, SAFE methods require only the discretization of the cross–section of the wave which can be modelled by analytical description. For instance, Marzani [133]

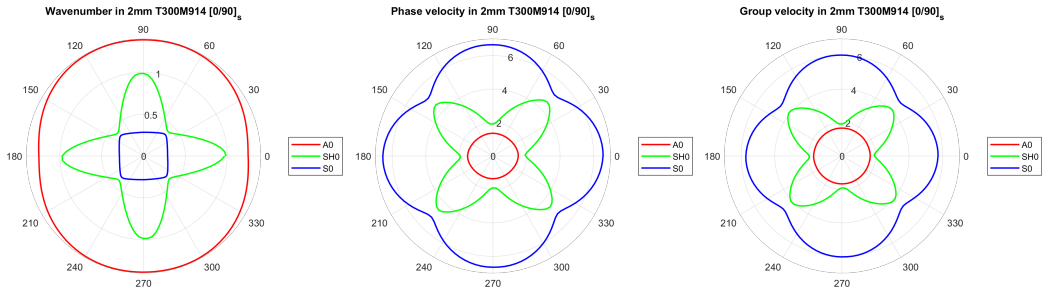

(a) (b) (c)

Figure 4.3: Wavenumber (a), phase velocity (b) and group velocity (c) profiles at 300 kHz in a 2 mm CFRP.

and Bocchini [134] developed a Graphical User Interface for Graphical User Interface for Guided Ultrasonic Waves (GUIGUW) based on SAFE simulations. The core code which derives from the studies [135–138], has been extended in a user–friendly tool able to deal with guided waves propagation in different materials of different shapes. Finally, LISA is essentially a FDM variant. LISA exploits iterative equations taken from elastodynamic equilibrium to model the displacements at a given point based on those at their neighbours at past time steps. Examples of studies that used this technique are [139, 140]. Once the propagation characteristics are computed along a specific direction, the analysis can be extended to anisotropic plates by repeatedly extracting the dispersion curves along with multiple directions. Thus, the direction–dependant characteristics of the waves propagation can be addressed. For instance, in Figure 4.3, the wavenumber, phase and group velocity propagation characteristic is shown for a T300M914 plate of thickness 2 mm and layup $[0/90]_s$ at 300 kHz.

4.2 Sensing and actuation of Lamb waves

Once the plate is theoretically characterized, an experimental analysis can be carried on. The experimental validation of the plate structural integrity has been addressed in many research studies by means of different methods [141–144]. Usually, an actuator is exploited to generate the Lamb wavefield in the structure which will be captured by one or multiple passive sensors. Then the signal is digitized by an acquisition system and stored. Finally, the plate condition can be addressed by signal processing. The type of excitation signal is fundamental for obtaining an advantageous signal–to–noise ratio, reducing dispersion and separating different modes in time or frequency domain. In particular, signals characterized by both short duration and narrow frequency band limit dispersion effects [125]. In particular, the main idea is to exploit narrowband characteristic to focus the signal at a specific frequency where dispersion, *i.e.* the variation of the velocity in the band, is minimized. Moreover, narrowband excitation signals are usually windowed in time domain. In fact, the time window is used to concentrate the energy of the signal thus reducing broadening. The most common windows are Hann [145], Gaussian [146] and Gaussian pulse [147] windows. To generate and then receive Lamb waves, many different strategies and sensors can be exploited, depending on the type of damage, inspection and material properties. Conventional ultrasonic probes have been widely used both to actuate and acquire ultrasonic signals due to their precision and the possibility to tune the angle perspex wedges [148]. In this case, GWs are actuated by the probe obliquely to the plate by exploiting a wedge. Both pressure and shear waves are generated. Nevertheless, this technology is heavy and expensive, thus not suitable in an SHM scenario [149]. Non contact probes, *i.e.* air–coupled [150], fluid–coupled [151] and EMATs [152, 153], have been introduced lately. Anyway,

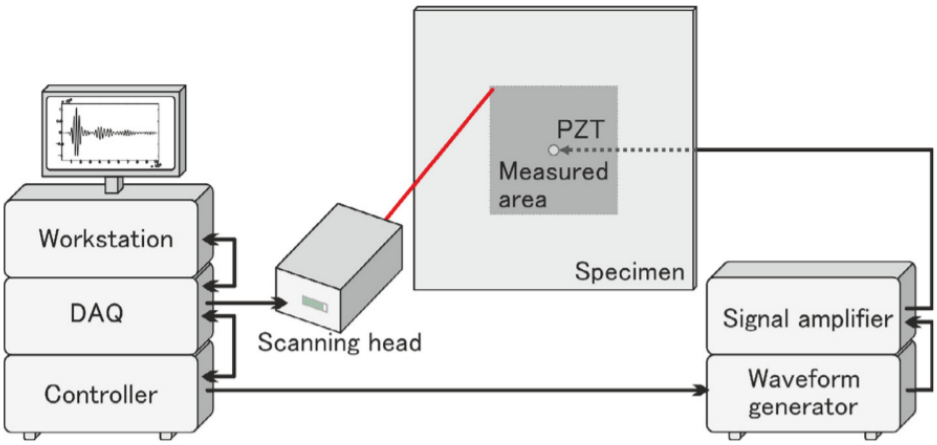

Figure 4.4: Laser Doppler Vibrometer setup [155]

similar issues w.r.t. conventional probes affect these technologies which are limited in practical scenarios. As an alternative, Laser Doppler Vibrometer (LDV) is a non–contact instrument that exploit the Doppler shift principle to measure the velocity of a moving object. In particular, LDVs compare the frequency of the light reflected by the object with a reference, *i.e.* the frequency of the emitted light [154]. Thus, LDV provides a series of images that represent wave propagation and interaction in time and space. For a more accurate measurement, each point of the grid can be acquired multiple times and averaged to increase the signal–to–noise ratio. For instance, in Figure 4.4 a typical LDV setup is shown. The interface between the user and the instrument is the workstation, which exploits the LDV software for the configuration. Then, the scanning head which generates the laser is connected to a Data AQuisition (DAQ) enabling the wavefield acquisition. The synchronization between the signal actuation and the acquisition is handled by the controller. Finally, the signal is generated by a waveform generator and an amplifier, connected to a PZT sensor placed at the centre of the specimen. Due to the LDV measurement

accuracy, a wide range of applications can be addressed [156]. For instance, Staszewski et al. [157] demonstrated the LDV potential in fatigue crack detection in metallic structures. Duflo et al. [158], instead, characterized defects in the bonding of two carbon epoxy composite plates by means of laser vibrometer measurements. Although LDV measurements permit accurate and complete analysis with high–quality images, this approach is time–consuming and expensive. Recently, different techniques based on Compressive Sensing (CS) have been presented to speed up the acquisition phase. Di Ianni et al. [159] demonstrated that the reduction of the measurement locations required for accurate signal recovery is less than 34% w.r.t. the original measurement grid by using CS. Similarly, Mesnil et al. [160] presented a CS technique for reconstructing the Lamb wavefield by using propagation dispersion properties of the plate. Harley et al [161–163], instead, introduced a sparse wavefield analysis for reconstructing the wavefield in isotropic and anisotropic plates exploiting suitable dictionaries. Nevertheless, the most exploited technology so far for inspecting plate–like structures are piezoelectric sensors due to many different reasons, such as small volume, low weight, easy integration, good mechanical strength, different frequency responses depending on the PZT type (resonators, flat band, wide band etc.), and low cost. Generally, PZT elements are manufactured in thin wafers of piezoelectric material. In such a case, they are addressed as Piezoelectric Wafer Active Sensors (PWAS). Another sensing technology, instead, are interdigital transducers, such as PolyVinyliDene Fluoride (PVDF) piezoelectric polymer film. PVDFs usually feature good flexibility such as higher dimensional stability. Moreover, by changing the space between interdigital electrodes, it is possible to select a specific wavelength [164]. Nevertheless, their application is quite limited so far [165]. In general, the main principle of piezoelectric materials relies on the cause–effect

relationship between the material shape and the electrical voltage which can be imposed/measured at the PZT electrodes. If the PZT transducer is subjected to an electrical voltage, the material changes its shape. Thus, if a signal is applied, the sensor vibrates accordingly, generating Lamb waves. Conversely, if the sensor is hit by a Lamb wave that mechanically deforms the PZT, a proportional voltage is generated at the electrodes. As a consequence, PWAS can be exploited for both generating and sensing Lamb waves. The relationship between electrical and mechanical properties of PWAS can be expressed as:

$$\begin{aligned} S_{ij} &= s^{E}_{ijkl} T_{kl} + d_{kij} E_k \\ D_j &= d_{jkl} T_{kl} + \epsilon^{T}_{jk} E_k \end{aligned} \tag{4.7}$$

where S_{ij}, T_{kl}, E_k and D_j are the mechanical strain, mechanical stress, electrical field, and electrical displacement, respectively. Moreover, s^{E}_{ijkl} and d_{jkl} are the mechanical compliance of the material at $E = 0$ and $T = 0$, and the piezoelectric coupling effect, respectively. By considering a PWAS of length l, width b and thickness h, where $h << b << l$, the above equations can be simplified assuming one–dimensional case:

$$\begin{aligned} S_1 &= s_{11} T_1 + d_{31} E_3 \\ D_3 &= d_{31} T_1 + \epsilon_{33} E_3 \end{aligned} \tag{4.8}$$

In the case of active PWAS configuration, the actuated strain which follows the application of a harmonic voltage $V(t) = \overline{V} e^{i\omega t}$ at the electrodes can be defined as:

$$S_1 = d_{31} \frac{V(t)}{h} \tag{4.9}$$

Conversely, in the case of passive PWAS configuration, let's assume longitudinal expansion u_1. As a result of harmonic vibration, harmonic voltage at the same natural frequency ω can be assumed. Thus, Eq.4.8 can be rewritten

using Newton's notation for derivatives as:

$$\begin{aligned} \dot{S}_1 &= s_{11}\dot{T}_1 + d_{31}\dot{E}_3 \\ \dot{D}_3 &= d_{31}\dot{T}_1 + \epsilon_{33}\dot{E}_3 \end{aligned} \tag{4.10}$$

where the harmonic regime in one dimension is assumed. As a consequence of harmonic strain, an AC current is generated if the sensor is plugged in a suitable sensing circuit:

$$\begin{aligned} I &= \dot{D}_3 A \\ I &= V Y_e \end{aligned} \tag{4.11}$$

where Y_e is the admittance of the circuit connected to the PWAS, and A is the PWAS area. By exploiting Kirchhoff's equations, it is possible to obtain the corresponding generated voltage following the passages shown in [166]:

$$V = \frac{1}{Y_e + (1 - k_{31}^2)Y_0} A \frac{d_{31}}{s_{11}} \dot{S}_1 \tag{4.12}$$

Both PWAS and conventional ultrasonic transducers [167] employ piezoelectric materials, but they differ for some fundamental aspects. At first, PWAS can be strongly attached to the structure by means of adhesive bonds, resin, glue or even directly embedded in the structure itself during the manufacturing process [168]. On the other hand, conventional ultrasonic sensors are usually coupled using gel, water or air. Another important difference between PWAS and ultrasonic sensors is their frequency response. In fact, the former features non–resonant broad–band response, while the latter presents a resonant narrow–band frequency characteristic. Moreover, it's worthy to underline the possibility to selectively tune PWAS into certain Lamb modes. The tuning between PWAS and Lamb waves has been extensively studied by Giurgiutiu in both metallic plates [149, 168, 169] and composites [170]. The main concept is that the PWAS mechanical deformation properties depend on the excitation frequency. This leads to the stimulation of a certain preferential guided

wave mode which depends on the excited frequency. This aspect is fundamental since specific propagation modes are more sensitive to specific defects. Generally, the selection of A_0 and S_0 mode is used, depending on the application case. Although S_0 is the preferred in many studies [171], A_0 selection is highly recommended for the detection of delaminations and transverse ply cracks [172–174].

4.3 SHM techniques with Piezo transducers

Thanks to the characteristics mentioned in the previous section, piezoelectric sensors are widely exploited for many SHM needs. An SHM strategy is to exploit near–field damage detection by using piezoelectric sensors for high–frequency impedance method. This technique is based on the ElectroMechanical Impedance (EMI) principle [175]. When a piezoelectric sensor is bonded to a structure, it is possible to detect changes in the mechanical properties of the structure by measuring the electrical impedance of the transducer [176]. In particular, an accurate model of the interaction between the PWAS and the structure is fundamental to predict the impedance behaviour and thus identify damage. For instance, Giurgiutiu at al. [177] modelled a thin isotropic circular plate with a PWAS surface mounted at its centre. Nevertheless, accuracy limitation rise between the model and the real application case, thus models are mostly applied only to simple structures such as beams, shells and plates. For such a reason, recently Finite–Elements based simulations are usually exploited, such as in [178–180]. After the definition of the model, the impedance signatures are acquired and analysed. Among the many different methods, Root Mean Square Deviation (RMSD), Mean Absolute Percentage Deviation (MAPD), covariance and Correlation Coefficient (CC) are the

most used [181–183]. Other examples of EMI applied to SHM can be found in [184–187]. Nevertheless, the difficulties to migrate this kind of analysis from a controlled environment, *i.e.* laboratory, to a real case scenario, where temperature, PZT durability - especially if not protected by a proper case - and bonding layer deterioration can affect the impedance signature lead to questions regarding their potential in real–life applications. On the other hand, the most common NDT strategy which employs PZT sensors is the active ultrasonic inspection by means of Lamb waves. By using *active-passive* sensor networks, where the plate–like structure is sensorized with both active and passive transducers, it is possible to accurately detect, localize and characterize damages [188]. In this configuration, a guided wave source generated by a PZT actuator stimulates stress waves that propagate through the material. The two main actuation–reception strategies are pulse–echo and pitch–catch methods [189]. In pulse–echo mode, the same sensor acts as both actuator and receiver, by switching the role in a well–temporized dance [190]. In pitch–catch configuration, instead, a single sensor is used as actuator while one or multiple transducers are exploited as receivers. This configuration can be static, or, as an alternative, each sensor can act in turn as actuator in a round–robin fashion, where each transducer of the network acts as transmitter for a turn before giving the role to another sensor [AP5]. In such a way, the entire structure area is interrogated from a variety of angles, maximizing the probability of damage detection. The main idea is to exploit the unique scattering waves and mode conversion generated by damages. Since scatters are usually low signal–to–noise ratio, array of PWAS specifically designed are exploited. The optimal sensors configuration to minimize undesired edges reflections which might affect the measurement and at the same time increase the SNR of the signals which actually provide information is not trivial. For example, Lee et al. [131]

analysed the sensor positions by local interaction simulations made on an aluminium plate with a rectangular damage slot and a fatigue crack. Fendzi et al. [191], instead, enhanced the damage detectability by optimizing the sensors placements with a Genetic Algorithm (GA). Another strategy to increase the signal to noise ratio of ultrasonic signals is to exploit constructive interference among multiple excited signals delayed by a specific phase [192]. Nevertheless, this method is difficult to practically implement, thus conventional pitch–catch measurements are usually preferred. In this case, to overcome signal–to–noise limitations sophisticated signal processing techniques are required to analyse GWs signals. Fourier Transform [193], wavelet decomposition [194], statistical based methods [195] and machine learning methods [196] are only few techniques which might be used for detecting and localizing the damage. Conversely, a *only-passive* sensor network can be adopted by exploiting AE [197]. Usually, the GW sources are impacts or material discontinuities such as cracks or corrosion events, which generate sudden energy release. Data acquisition relies on acquiring a continuous data stream by the sensing elements. Then, signals are stored after the crossing of a pre–determined threshold. Similarly to *active–passive* ultrasonic inspection, it is possible to detect [198], localize [199, 200] and discriminate damages [201] in different types of structures by AEs as well.

In the next section, both *passive–only* and *active–passive* network approaches will be investigated. In particular, damage localization methods are addressed.

Chapter 5

Ultrasonic Guided Waves localization techniques

Ultrasonic guide waves have increasingly been adopted in SHM of plate-like structures because of their effectiveness and versatility. Usually, arrays of spatially distributed piezoelectric transducers are exploited for damage detection, localization and quantification. In particular, damage localization can be carried on by several different techniques depending on the data acquisition strategy *i.e.* *passive–only* or *active–passive* inspection. The former usually exploits strategies based on Time-of-Flight (ToF) [202] between the acquired waves since actuation time is unknown. For instance, hyperbolic positioning algorithms can perform impact or crack localization by calculating the ToF of the wavefronts acquired by different sensors. Other approaches exists, such as neural networks [203], genetic algorithms [204] or wavelet analysis [205]. In active–passive networks, instead, receivers can be triggered on exact actuation time. Thus, ToF between the transmitter and the receivers can be estimated by exploiting specific procedure to extract the time of arrival [206]. The presence of damages, indeed, generates scattering waves and echoes, which can be

detected and manipulated to characterize and localize the damage. Thus, defects are generally located by triangulation procedures [207], statistical–based approaches [208] or Elliptical algorithm [209].

In this chapter, different localization algorithms and approaches are investigated. In particular, a Lamb waves localization algorithm based on wavelet decomposition for *passive–only* networks is introduced. The approach is validated by means of an experimental setup and enhanced by a calibration procedure enabling high precision waves Direction of Arrival (DoA) estimation. Similarly, damage localization algorithms for *active–passive* networks are investigated as well. By exploiting pitch–catch measurements in a round–robin fashion acquisition strategy, beamforming imaging techniques are introduced. Specifically, two DAS–family imaging techniques are presented, *i.e.* the Delay Multiply and Sum (DMAS) and the Double-Stage Delay Multiply and Sum (DS-DMAS). Moreover, a filtering procedure called Fresnel filtering has been implemented to further enhance artefacts suppression. The proposed algorithms testing has been carried out on an online, freely available Guided Waves dataset *Open Guided Waves* (`http://openguidedwaves.de/`) that collects piezoelectric guided waves signals travelling through a *quasi*-isotropic composite plate in different damage conditions.

5.1 Impact localization in passive-only networks

Literature offers many strategies for evaluating the impact localization over a sensorized material by Lamb waves passive inspection. The most common method is based on the conjunction of conventional passive monitoring systems [205, 210–213] and hyperbolic positioning algorithms. The main idea is to exploit the Difference Time of Arrival (DToA) of the wavefronts ac-

quired by multiple sensors. Then, knowing the transducers position and the group velocity of the propagating waves, by geometric considerations it is possible to determine the hyperbolae on which the impact or crack point must lie [214,215]. As a drawback, a precise and reliable DToA estimation is not trivial [216, 217]. Usually, threshold–based procedures [211, 218], peak detection methods [219,220] and cross–correlation based techniques [221,222] are mostly used. Anyway, guided waves dispersion might affect the precision of the DToA estimation. To tackle this aspect, Azaria et al. [223] exploited generalized correlation methods to enhance the receiver frequency band thus reducing the DToA estimation. However, the proposed approaches are most effective only in the case of non-perfect dispersion compensation or in reverberating structures. Thus, Perelli et al. [224] enhanced conventional generalized cross–correlation methods with a two-step processing framework. In the firsts step a dispersion compensation based on warped frequency transform [188, 225] is performed. Then, DToA is estimated by wavelet decomposition of cross–correlating signals. In fact, the wavelet coefficients in the warped distance-frequency domain can estimate accurately the guided wave DToA between two sensors. Another strategy, instead, is based on the exploitation of inverse optimization processes. Park et al. [213] used the transfer functions in the system-identification technique able to identify the location and force time history of an impact event on a structure. The bright side of this approach is the capability to accurately estimate the impact position without full–scale structural model or excessive training data. Xu [226], instead, investigated extreme learning machine, *i.e.* a learning algorithm for single-hidden layer feedforward neural network, and least squares support vector machine for structural impact localization. Morse et al. [227], instead, exploited ANN in conjunction with Bayesian updating and Kalman filter techniques to improve the reliability of the detection algorithm.

Furthermore, Coverley and Staszewski [228] used a genetic optimization of the sensor triangulation procedure. Finally, the extraction of useful information for impact localization can be directly addressed by *ad–hoc* transducers, specifically designed to estimate the damage position or the waves' direction of arrival. Matt and Lanza di Scalea [229] exploited composite piezoelectric rosettes for acoustic source location in anisotropic or geometrically complex structures. Romanoni et al. [230] synthesised the beam steering by exploiting interference phenomena due to the periodic structure and activation time of the designed sensor array. Thus, directional scanning among 4 different propagation directions can be enabled by properly selecting the appropriate excitation frequency. Bavarelli et al. [231, 232], instead, were able to achieve arbitrary beam steering directionality in the [0°-180°] angular range by means of a shaped array with a spatial distribution that defines a spiral in the wavenumber space. Following the same design concepts, De Marchi et al. [233] developed a piezoelectric sensor made of two patches of different shapes able to retrieve the Lamb waves direction of arrival. The same author extended the sensor with another patch for improving the estimation accuracy in [234]. These solutions are supposed to achieve a complexity reduction of passive monitoring systems, reducing signal channels to be recorded and simplifying the related signal processing tasks. As a drawback, the design and fabrication of these sensors are not trivial. In this work, a novel impact localization method that exploits a novel cluster of three piezoelectrics (PZTs) transducers in 60 degrees configuration with dedicated signal processing is presented. Despite the above–cited *ad–hoc* sensors, the proposed cluster is made of round–shape PZT buzzers which are very simple to produce. In fact, the DoA estimation is extracted by geometrical considerations on the PZTs spatial arrangement, reducing the computational cost of the algorithm and without any information about the

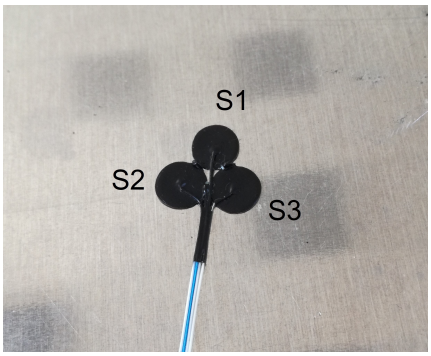

Figure 5.1: PZT Cluster [AP6].

material characteristics. Moreover, a multiresolution DFT-Based Continuous Wavelet Transform (CWT) decomposition applied to the signals acquired is performed. The multiple frequency-based filtering of the signals in the wavelet domain counteracts the dispersive propagation characteristic of the material, enabling a robust and reliable cross–correlation among signals. Subsequently, the angle estimation are applied for each computed scale. The approach is validated by means of an experimental setup on a sensorised aluminium plate. As a further step, a calibration procedure based on a Cubic Spline Interpolation is implemented to significantly reduce the DoA estimation error.

5.1.1 PZT Cluster description

Disclaimer: the following section is an extension of ©2021 IEEE [AP6].

The designed sensor is a cluster of three circular closely-located PZT elements [235] featuring 10 mm of diameter each, forming an angle of 60°. The sensor is shown in Fig.5.1. Moreover, the following considerations can be carried on by considering Fig.5.2. In the picture, PZT areas are outlined as blue dots and addressed as $S1$, $S2$ and $S3$. The distances between their centroid depicted as a black dot are constant and equal to R. Let's assume that an impact occurs

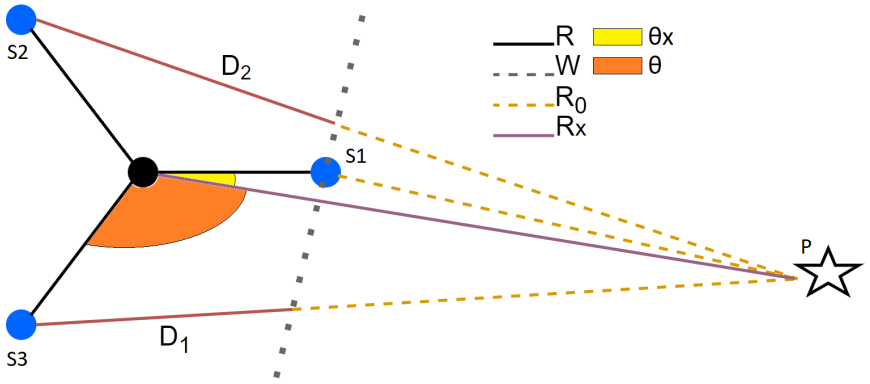

Figure 5.2: Active elements arrangement: the sensors active areas form an equilateral triangle. The GW travels from the right to the left of the figure.

in a generic point P on the plate which has been represented as a star, and the resulting wavefront W propagates from P to the cluster. If the Fraunhofer approximation for far fields is valid, the incident wavefront may be assumed as planar. Then, it is possible to define the following distances:

- R_0 is the distance between the impact point P and the wavefront at the time instant in which reaches the first PZT transducer $S1$;
- R_x is the distance between P and the cluster centroid
- $D1/D2$ are the distances between the wavefront at the time instant in which reaches the first PZT transducer $S1$, and $S3/S2$, respectively.
- $R_1 = D1 + R_0$
- $R_2 = D2 + R_0$

Moreover, two angles are highlighted, θ_x and θ, respectively. If an angle θ_1 is defined as $\theta_1 = \theta + \theta_x$, then the following is valid [236]:

$$\begin{aligned} R_1^2 &= R^2 + R_x^2 - 2RR_x\cos(\theta_1 - \theta_x) \\ (D1 + R_0)^2 &= R^2 + R_x^2 - 2RR_x\cos(\theta_1 - \theta_x) \\ D1^2 + 2D1R_0 + R0^2 &= R^2 + R_x^2 - 2RR_x\cos(\theta_1 - \theta_x) \end{aligned} \tag{5.1}$$

Similarly, R_0 can be expressed using the law of cosines as:

$$R_0^2 = R^2 + R_x^2 - 2RR_x\cos(\theta_x) \tag{5.2}$$

Thus, by using Eq.5.2 in Eq.5.1:

$$\begin{aligned} &D1^2 + 2D1R_0 + R^2 + R_x^2 - 2RR_x\cos(\theta_x) = R^2 + R_x^2 - 2RR_x\cos(\theta_1 - \theta_x) \\ &D1^2 + 2D1R_0 = -2RR_x[\cos(\theta_1 - \theta_x) - cos(\theta_x)] \end{aligned} \tag{5.3}$$

Similarly, the same considerations can be carried out starting from R_2^2 expansion. Thus, the following equation can be written:

$$D2^2 + 2D2R_0 = -2RR_x[\cos(\theta_2 - \theta_x) - \cos(\theta_x)] \tag{5.4}$$

Since the Fraunhofer approximation has been assumed, then $R_0 > 0$, ${}^{D1}/_{R0} < 1$ and ${}^{D2}/_{R0} < 1$. Consequently, if both terms in Eqs.5.3 and 5.4 are divided by R_0^2, the following approximation can be computed:

$$\begin{aligned} {}^{2D1}/_{R_0} &\approx -2{}^{RR_x}/_{R_0^2}[\cos(\theta_1 - \theta_x)\cos(\theta_x)] \\ {}^{2D2}/_{R_0} &\approx -2{}^{RR_x}/_{R_0^2}[\cos(\theta_2 - \theta_x)\cos(\theta_x)] \end{aligned} \tag{5.5}$$

Finally, by dividing each other the two main equations in 5.5, the ${}^{D1}/_{D2}$ relationship is highlighted:

$$\begin{aligned} \frac{D1}{D2} &\approx \frac{\cos(\theta_1 - \theta_x)\cos(\theta_x)}{\cos(\theta_2 - \theta_x)\cos(\theta_x)} \\ &\approx \frac{\cos(\theta_1)\cos(\theta_x) + \sin(\theta_x)\sin(\theta_1) - \cos(\theta_x)}{\cos(\theta_2)\cos(\theta_x) + \sin(\theta_x)\sin(\theta_2) - \cos(\theta_x)} \end{aligned} \tag{5.6}$$

Because of the spatial distribution of the PZT transducers, we can assume that $\theta_1 = -\theta_2 = 120°$. The minus sign on θ_2 is due to orientation convention. Thus:

$$\begin{aligned}\frac{D1}{D2} &\approx \frac{-1/2\cos(\theta_x) + \sqrt{(3)}/2\sin(\theta_x) - \cos(\theta_x)}{-1/2\cos(\theta_x) + \sqrt{(3)}/2\sin(\theta_x) - \cos(\theta_x)} \\ &\approx \frac{-3/2\cos(\theta_x) - \sqrt{(3)}/2\sin(\theta_x)}{3/2\cos(\theta_x) + \sqrt{(3)}/2\sin(\theta_x)} \\ &\approx \frac{1 - 1/\sqrt{3}\tan(\theta_x)}{1 + 1/\sqrt{3}\tan(\theta_x)}\end{aligned} \tag{5.7}$$

Finally, θ_x can be extracted:

$$\begin{aligned}\tan(\theta_x) &\approx \left(\sqrt{3}\,\frac{1 - {}^{D_1}/_{D_2}}{1 + {}^{D_1}/_{D_2}}\right) \\ \theta_x &\approx \operatorname{atan}\left(\sqrt{3}\,\frac{1 - {}^{D_1}/_{D_2}}{1 + {}^{D_1}/_{D_2}}\right)\end{aligned} \tag{5.8}$$

where ${}^{D1}/_{D2} \in [0, 1]$ and $\theta_x \in [0, 60°]$. Because of the strict relationship between the distance travelled by the stress wave, its velocity and the time taken to cover such distance, 5.9 can be rearranged in terms of the DToAs $\Delta t_{1,2}$ and $\Delta t_{1,3}$. Let's consider a rotation of 30° for a more convenient coordinate reference system. Thus, $\overline{\theta} = \theta_x - 30°$, with $\overline{\theta} \in [-30°, 30°]$. Starting from the first equation of 5.9, the following can be derive:

$$\begin{aligned}\tan(\overline{\theta} + 30°) &\approx \sqrt{3}\,\frac{1 - {}^{D_1}/_{D_2}}{1 + {}^{D_1}/_{D_2}} \\ \frac{\tan(\overline{\theta}) + \tan(30°)}{1 - \tan(\overline{\theta})\tan(30°)} &\approx \sqrt{3}\,\frac{1 - {}^{D_1}/_{D_2}}{1 + {}^{D_1}/_{D_2}} \\ \frac{tan(\overline{\theta}) + \frac{1}{\sqrt{3}}}{1 - \frac{1}{\sqrt{3}}\tan(\overline{\theta})} &\approx \sqrt{3}\,\frac{1 - {}^{D_1}/_{D_2}}{1 + {}^{D_1}/_{D_2}} \\ \sqrt{3}\frac{1 + \sqrt{3}\tan(\overline{\theta})}{3 - \sqrt{3}\tan(\overline{\theta})} &\approx \sqrt{3}\,\frac{1 - {}^{D_1}/_{D_2}}{1 + {}^{D_1}/_{D_2}} \\ \frac{1 + \sqrt{3}\tan(\overline{\theta})}{3 - \sqrt{3}\tan(\overline{\theta})} &\approx \frac{1 - {}^{D_1}/_{D_2}}{1 + {}^{D_1}/_{D_2}}\end{aligned} \tag{5.9}$$

For lightening the expression, $^{D1}/_{D2}$ can be addressed as x and $\sqrt{3}tan(\overline{\theta})$ as k.

$$\begin{aligned}(1-x)(3-k) &= (1+k)(1+x)\\ 3-3x-k+xk &= 1+k+x+kx\\ k &= 1-2x\end{aligned} \tag{5.10}$$

Finally, by expanding x and k, the final expression can be written:

$$\begin{aligned}\sqrt{3}\tan(\overline{\theta}) &= 1-2\frac{D1}{D2}\\ \overline{\theta} &= \text{atan}\left(\frac{1-2\frac{D1}{D2}}{\sqrt{3}}\right)\\ \overline{\theta} &= \text{atan}\left(\frac{1-2\frac{\Delta t_{1,3}}{\Delta t_{1,2}}}{\sqrt{3}}\right)\end{aligned} \tag{5.11}$$

where:

$$\begin{aligned}\Delta t_{1,2} &= \frac{D2}{v_g(\overline{\theta},f)}\\ \Delta t_{1,3} &= \frac{D1}{v_g(\overline{\theta},f)}\end{aligned} \tag{5.12}$$

It is worthy to underline that the group velocity $v_g(\overline{\theta},f)$, where f is the frequency dependence of the velocity which mathematically explains dispersion, is suppressed in the final equation 5.11 under the far field approximation due to the ratio $^{D1}/_{D2}$. In fact, due to the close position of the sensors, $v_g(\overline{\theta},f)$ can be supposed with a good approximation the same for both the signals that hit the sensors. Thus, the method does not require any *a–priori* information about the group velocity. Nevertheless, a precise estimation of the difference in the time of arrivals between the PZT sensors is still required.

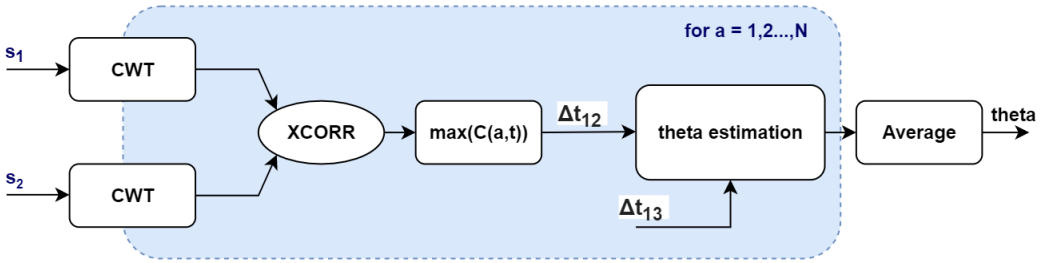

Figure 5.3: DoA estimation algorithm

5.1.2 DoA estimation algorithm

Disclaimer: the following section is an extension of ©2021 IEEE [AP6].

The precision of the impact DoA $\overline{\theta}$ estimation is strictly related to the DToA evaluation. Nevertheless, conventional cross-correlation techniques in the time domain usually lack in accuracy in a real case scenario. In fact, stress waves are affected during their propagation by dispersion, where signals broaden due to the different velocities of different wave harmonics. Thus, the DToA evaluation by just cross–correlating the PZT raw signals results to be not sufficiently accurate. A multiresolution isofrequential analysis employing DFT-Based CWT is adopted to limit the dispersion effect. In practical terms, the algorithm performs narrow band filtering by exploiting CWT decomposition as a filtering technique. Thus, cross–correlation is applied recursively for each narrowband frequency band defined by the multiresolution analysis to estimate the DToA and then, DoA, multiple times. Finally, once the procedure is concluded, an averaging procedure on the estimated angles for each computed scale is performed. The continuous wavelet transform is usually exploited to investigate non–stationary signals in time–frequency domain. By exploiting windows of variable width, it is possible to tune the resolution analysis for a specific time–frequency characteristic. For instance, long time windows permit

the extraction of more precise low–frequency information, conversely, shorter windows permit the extraction of high–frequency information. To do that, a function called *mother–wavelet* characterized by two main parameters, the translating parameter b and the scaling factor a must be synthesised. Thus, the mother wavelet can be defined as:

$$\psi_{ab}(t) = |a|^{-\frac{1}{2}} \psi \left(\frac{t-b}{a} \right) \tag{5.13}$$

where b defines the time shift of the window, meanwhile a is strictly related to the wavelet dilatation. $|a|^{-\frac{1}{2}}$, instead, is an energy normalized factor due to the fact that the energy of the wavelet must be the same for different a values of the scale. To be classified as a wavelet, $\psi_{a,b}(t)$ must have finite energy. Let $s_i(t)$ be the signal associated to the i-th active area S_i of the PZT cluster, then the CWT, addressed as W_i, can be written:

$$W_i(\psi; a, b) = \int_{-\infty}^{+\infty} s_i(t) \psi^*_{ab}(t) \; dt = < s_i(t), \psi_{ab}(t) > \tag{5.14}$$

As an inverse transformation, it is possible to obtain again the original signal s_i by the following relationship:

$$s_i(t) = \frac{1}{C_\psi} \int \int_{-\infty}^{+\infty} \frac{1}{a^2} W_i(\psi; a, b) \psi_{ab}(t) \; da \; db \tag{5.15}$$

where C_ψ is a finite constant defined as the integral of the square value of the mother wavelet in absolute terms in the Fourier domain, divided by the angular frequency:

$$C_\psi = \int_0^{+\infty} \frac{|\Psi(\omega)|^2}{\omega} \; d\omega < \infty \tag{5.16}$$

The convergence of C_ψ is ensured if $\Psi(0) = 0$. Thus, the wavelet mother must be a zero–mean signal. To reduce the computational complexity of the Wavelet Transform, it is possible to rearrange 5.14 following the convolution theorem. In fact, the wavelet transform given 5.14 can be viewed as the convolution of

the signal with a wavelet function. Thus:

$$W_i(\Psi; a, b) = \frac{1}{2\pi} \int_{-\infty}^{+\infty} S_i(\omega) \Psi^*_{a,b}(\omega)\ d\omega \tag{5.17}$$

where $\Psi^*_{a,b}(\omega) = \sqrt{a}\psi^*(a\omega)e^{i\omega b}$. Moreover, the product between the signal in the frequency domain and $\Psi^*_{a,b}(\omega)$ can be read as a band pass filtering of the signal in the frequency domain. By Cross-correlating the CWT coefficients for each scale a, the DToA between two PZT sensors is extracted, as shown in the following equations.

$$C_{i,j}(a, t) = \int_{-\infty}^{+\infty} W^*_i(\Psi, a, b) W_j(\Psi, a, t + b)\ db \tag{5.18}$$

$$\Delta t_{i,j}(a) = \max_t (C_{i,j}(a, t)) \tag{5.19}$$

Then, the DoA is estimated by applying Eq.5.11 for each a value. Finally, the dependence on the scale factor is overcome by means of an averaging procedure that provides to the user the final estimation of the DoA in angular terms [237, 238]. The algorithm is outlined in the diagram of Fig.5.3.

5.1.3 Experimental investigation and results

Disclaimer: the following section was previously published by ©2021 IEEE [AP6] and [AP7]

The methodology has been tested in a laboratory experimental setup. An aluminium square plate 1000 mm wide and 3 mm thick was sensorized with the PZT cluster, as shown in Fig. 5.4a. Signals from the cluster were acquired by a Tektronix 3014 digital oscilloscope at a sampling frequency of 10 MHz. For a complete characterization of the DoA estimation algorithm, two approaches were tested. In the first one, the impact was mimicked by a buzzer connected to a function generator and an amplifier. In particular, an Agilent 33220A function generator and a Tegam 2350 amplifier were used to obtain repeatable, precise and accurate control on the actuated signals. A burst of one sine wave

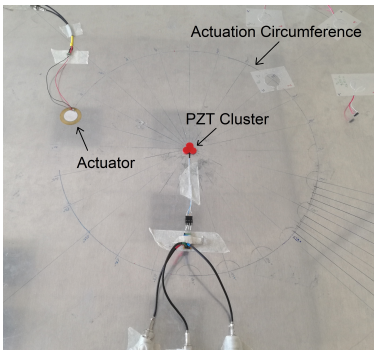

(a) Experimental Setup

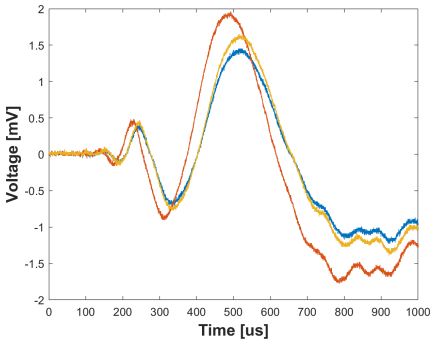

(b) PZT Cluster output Signals

Figure 5.4: The experimental setup exploited to test the DoA estimation algorithm (left) and the acquired waveforms (right) [AP6].

at 1 V_{pp} at 4 kHz was emitted by the function generator every 50 ms to simulate impacts on the plate. Then, the generated sinusoidal pulses were amplified by the Tegam 2350 with a gain factor of 50. The PZT actuator was placed along a circumference of radius 20 cm centred at the cluster position. The circle was divided into 24 angular intervals, each one 15° wide. GWs were made of 128 sinusoidal bursts at each angle of the quantized circumference. Thus, an average among all the 128 acquisitions was performed automatically by the oscilloscope to enhance the signal to noise ratio. An acquisition example after the average procedure is depicted in Fig.5.4b. Finally, the signals so obtained were processed by the localisation algorithm and the DoA was estimated for each actuation angle. The result of the localisation is shown in Fig.5.5, where the estimated DoA are depicted as small red circles. By comparing the actual DoA with the estimated angle, the high level of accuracy achieved by the algorithm is evident. In fact, the maximum error observed was 1.74°, with an average error of 1.15°. It's worthy to notice that, the DFT-based CWT implementation approach permits to reduce the computational cost of the entire algorithm, which has been executed in just 0.2 s for the estimation of all

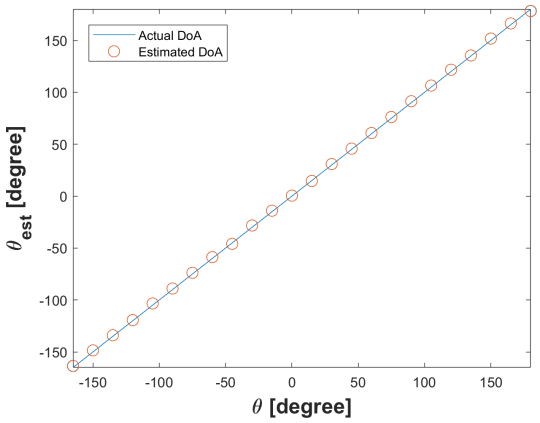

Figure 5.5: DoA estimation [AP6].

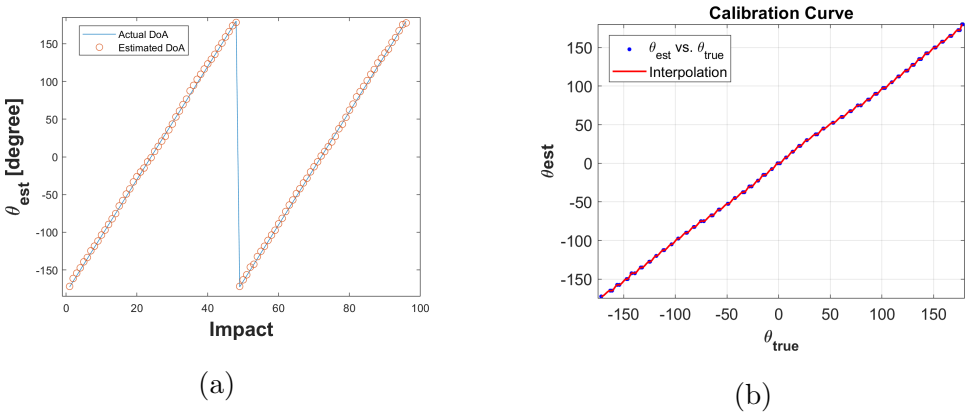

(a) (b)

Figure 5.6: (a) Calibration phase results. (b) Calibration curve [AP7].

the 24 angles of arrival. Afterwards, a second test was conducted by exploiting actual impacts on the aluminium plate generated by a metallic screw. Thus, GWs were generated by hitting the plate with the screw along a circumference of radius $R \approx 20\,\text{cm} \gg D_{1,2}$ centred at the PZT cluster position in order to satisfy the far–field approximation. The circle was divided into 48 angular intervals, each 7.5° wide. At first, a calibration procedure was implemented to compensate intrinsic inaccuracies which may occur if a real screw impact is used as a GWs source. Two cycles of impacts were generated on each angle of

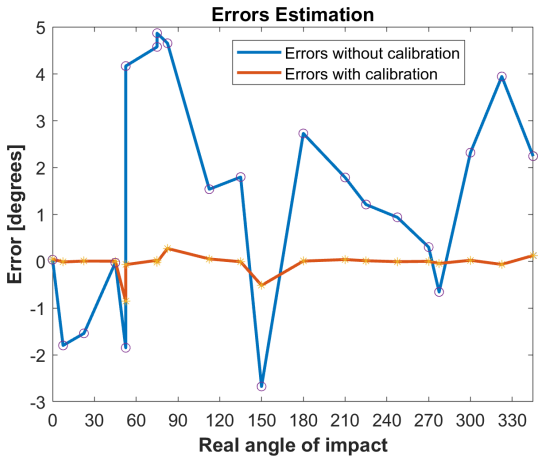

Figure 5.7: DoA estimation error before (blue line) and after (red line) the calibration procedure [AP7].

the quantized circumference, for a total of 96 training impacts. Signals from each impact were acquired and processed. Thus, the DoA is estimated for each point. In Fig. 5.6a, the estimated DoA for each impact position is depicted w.r.t. the actual DoA. At this stage, the maximum absolute error was around 5° with an average error of about 2°. Afterwards, a calibration procedure was conducted. The calibration curve was computed by associating the actual DoAs with the estimated ones by means of a Cubic Spline Interpolation (CSI) [239]. The calibration curve obtained is depicted in Fig.5.6b. During the test phase, another dataset of 21 randomly distributed impacts was acquired. The modalities, the instrumentation and the setup exploited are identical to the previous experiment. Thus, DoA and its relative error were computed for each impact before applying the calibration. The average error achieved was around 1.4°, with a maximum error of 4.8°. As expected, the performance of the DoA estimation algorithm is consistent with the estimation carried out during the calibration phase results. Finally, DoAs are tuned by means of the computed calibration curve. As a result, the average error from 1.4° drops to 0.0517°,

while the maximum error decreases from 4.8° to 0.8°. Fig.5.7 shows in detail the error trend. As expected, the estimation of the GW DoA, in conjunction with an appropriate calibration procedure, is able to perform reliable and accurate evaluations of the angle of arrival, with a resolution of less than one degree. As a final consideration, it is also worthy to mention that the computational time of the entire algorithm is just 0.13 seconds, due to the DFT-based Wavelet approach.

5.2 Damage localization in active–passive networks

Disclaimer: the following section is an extension of ©2022 IEEE [AP5].
Many imaging procedures have been developed for characterizing and localizing the damage in active–passive NDT and SHM fields [240]. In particular, correlation–based methods, probability imaging methods [241, 242], model–based methods, and Delay and Sum (DAS) family methods can be mentioned. In correlation–based methods, the image is synthesised by correlating the acquired signals with theoretical predictions computed on each point of a defined spatial grid. Since this approach is strongly dependent on the accuracy of the propagation model, hybrid empirical/analytical models have been recently proposed. Quaegebeur et al. [243] introduced an axisymmetric analysis of guided wave generation by a circular piezoceramic, where the complex shear and normal interfacial stress profiles between the transducer and the host structure were considered. In this study, excitation terms are estimated empirically by exploiting a best-fit model and a function derived from measured admittance. Ostiguy et al. [244], instead, compared delay–and–sum, dispersion compensation and correlation–based techniques in unidirectional transversely isotropic

laminate to quantitatively evaluate the robustness of the models which rule these techniques.

Probability imaging techniques, instead, such as Reconstruction Algorithm for the Probabilistic Inspection of Damage (RAPID), merge the Signal Difference Coefficient (SDC) which can be defined as the probability of the damage existence between the transmitter-receiver pair usually computed by baseline subtraction. Gao et al. [245] sensorized a wing of an E2 aircraft and computed different tomography algorithms based on SDS for damage localization, such as the back–projection method, Algebraic Reconstruction (ART) and Multi-resolution Algebraic Reconstruction Technology (MART). Hay et al., [195] exploited RAPID algorithm for comparing Lamb wave tomography approaches. This work demonstrated that tomographic images generated by fan-beam back–projection are less sensitive to material loss w.r.t. SDC methods. Afterwards, different solutions were presented as RAPID modifications for improving the algorithm performance. For instance, Azuara et al. [246] presented a geometrical modification of conventional RAPID method addressed as RAPIG–G. The proposed approach reduces the influence of the intersection points between sensor paths, thus improving the damage localization accuracy. Similarly, Dziendzikowski et al. [247] generalized RAPID approach for different PZT networks geometries. As a result, the estimated damage location is less biased by inhomogeneous distributions of sensing paths.

Model–based methods, instead, exploit the Green's function solution of the GWs propagation model in conjunction with the measured scattered wavefield. Neubeck et al. [248] recently proposed a unified framework of model–based imaging algorithms. In particular, results for different operators, *i.e.* Kirchhoff-Migration operator and Reverse Time Migration (RTM) operator, and solvers, *i.e.* joint or conventional solution, the Least-Squares Method

(LSM), the Orthogonal Matching Pursuit (OMP) and the SPGL1, are compared for a typical SHM experimental setup made of a sensorized aluminium plate and drilled holes as artificial defects.

Finally, DAS beamforming is based on back–propagating the signals residuals by exploiting the transmitter-receiver Time-of-Flight (ToF) estimation, knowing the group velocity. Residuals are computed by means of a baseline subtraction, where the baseline is acquired when the material is in pristine conditions. Usually, each transducer of the sensor array acts both as transmitter and receiver in a round robin fashion. Thus, one element of the array is excited for every transmission event, while all the remaining elements of the array are exploited to acquire the signal and a low–resolution image is computed over a defined spatial grid by a summation operation. This procedure is repeated as many times as the number of the transducers in the array, by changing the transmitter at each transmission event. Due to its low computational cost which permits real–time evaluation, its simple implementation and overall good performance, DAS is one of the most commonly adopted methods [249, 250]. As a drawback, DAS shows a limited imaging resolution and contrast which degrades with the decrease of the number of sensors. Moreover, DAS is sensitive to dispersive and multimodal behaviour of Lamb waves, as well as to noise and temperature variations in the baseline subtraction. To overcome these aspects, literature offers many different DAS modifications, which can be grouped into two main approaches. The former approach rely on pre–processing techniques such as dispersion [251, 252] and temperature [253, 254] compensation, sensors placement optimization [255] and sparse representation [256]. In the latter, instead, DAS resolution and SNR limitations are tackled by the development of modifications of the DAS approach. For instance, Lu et al. [257], proposed the multi–delay–and–sum imaging algorithm

which suppresses artefacts and reduces damage localization errors. The main idea is to exploit not only the ellipsis with the actuator and the receiver as foci, but also the hyperbola with two foci at two different receivers positions to compute a more robust damage localization. Another common strategy is to use specific fixed or adaptive beamforming weighting coefficients to improve image reconstruction. For instance, in the Minimum Variance (MV) [258, 259] method, DAS weighting coefficients are adaptively computed at each point of the spatial grid. Zhang et al. [260], instead, computed a sparse matrix of weights via a multiple sparse Bayesian learning. Delay Multiply and Sum (DMAS), instead, recently introduced in the SHM field by [AP8] and [248], aims to improve the conventional DAS imaging by combinatorially coupling and multiplying the backscattered signals before the final summation. In such a way, better contrast resolution, object definition and dynamic range can be achieved. DMAS was originally introduced by Lim et al. [261] in confocal microwave imaging, and then successfully applied to ultrasound B-mode medical imaging [262] and photoacoustic microscopy [263]. Nevertheless, it has been demonstrated that conventional DAS and DMAS algorithms can be outperformed (in terms of noise suppression, image resolution and dynamic range) by the so–called Double-Stage Delay Multiply and Sum (DS-DMAS) procedure in both medical ultrasounds [264] and photoacoustic imaging [265]. Afterwards, DS-DMAS has also been applied to radar-based microwave breast imaging for breast cancer localization [AP9]. Conversely, DS-DMAS has never been applied to NDT and SHM fields. In this work, DS-DMAS is introduced in an SHM application scenario. An exhaustive theoretical overview of DAS, DMAS and DS-DMAS is presented in the next section. Then, both medical imaging (i.e. breast cancer localization) and SHM imaging applications are presented and discussed highlighting the pro and cons of the techniques.

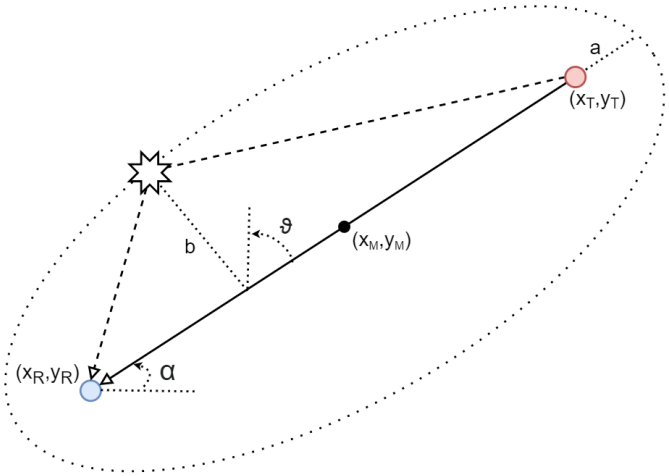

Figure 5.8: Schematic representation of the relationship between damage location and a single transmitter–receiver sensors pair.

5.2.1 Elliptical algorithms

The relationship between a damage location and a single transmitter-receiver pair of PZT transducers in an isotropic plate-like structure is depicted in Fig.5.8 The transmitter and receiver transducers are the red and blue circles, respectively, while the damage is represented as a star. The direct path of the propagating wave is the continuous arrow of length $\overline{TR}$ and azimuth angle θ between the transmitter and the receiver, while the scattering wave path is depicted as a dotted arrow which goes from the transmitter to the damage location and then, from the damage location to the receiver. As described in Moll et al. [266], it is possible to determine the length of the travel path of the scattering wave $\overline{TDR}$ as a function of the scattering wave Time of Flight ToF_s in the case of an isotropic plate given the waves group velocity c_g, :

$$\overline{TDR} = \overline{TD} + \overline{DR} = ToF_s * c_g \tag{5.20}$$

where $\overline{TD}$ and $\overline{DR}$ are the transmitter/damage location and damage location/receiver propagation distances, respectively. Nevertheless, the knowledge

of $\overline{TDR}$ and ToF_s is not enough for localizing the damage, since an infinite locus of points which lie in an ellipsis passing through the damage location with the transmitter and receiver sensors positions as foci satisfies 5.20. In particular, the ellipse equation can be written as follows:

$$\begin{aligned} x &= x_M + a * cos(\alpha)cos(\theta) - b * sin(\alpha)sin(\theta) \\ y &= y_M + a * sin(\alpha)cos(\theta) + b * cos(\alpha)sin(\theta) \end{aligned} \tag{5.21}$$

where a and b are the semi-axes and (x_M, y_M) are the coordinate of the middle point of the wave direct path. The angle α and the semi–axes a and b, instead, can be defined as:

$$\begin{cases} a = \frac{\overline{TDR}}{2} \\ b = \sqrt{a^2 - \left(\frac{\overline{TR}}{2}\right)^2} \end{cases} \tag{5.22}$$

$$\alpha = \begin{cases} arctan\left(\frac{y_R - y_T}{x_R - x_T}\right) & \text{if } x_R < x_T \\ arctan\left(\frac{y_R - y_T}{x_R - x_T}\right) + \pi & \text{otherwise} \end{cases} \tag{5.23}$$

where $\overline{TDR} \geq \overline{TR}$, and $[(x_T, y_T), (x_R, y_R)]$ are the transmitter and receiver coordinates, respectively. Thus, multiple transmitter-receiver pairs are required to determine uniquely the damage position. Several signal processing techniques can be adopted for evaluating the acquired signals and extract useful information, such as DAS, DMAS and DS-DMAS approaches.

5.2.2 DAS

In the Delay–And–Sum imaging algorithm, a low–quality image is synthesised for each transmission event. Usually, pitch–catch strategies can be exploited for generating and acquiring signals. If the actuator–receiver distance and the wave velocity are known, it is possible to focus the ultrasonic beam at each

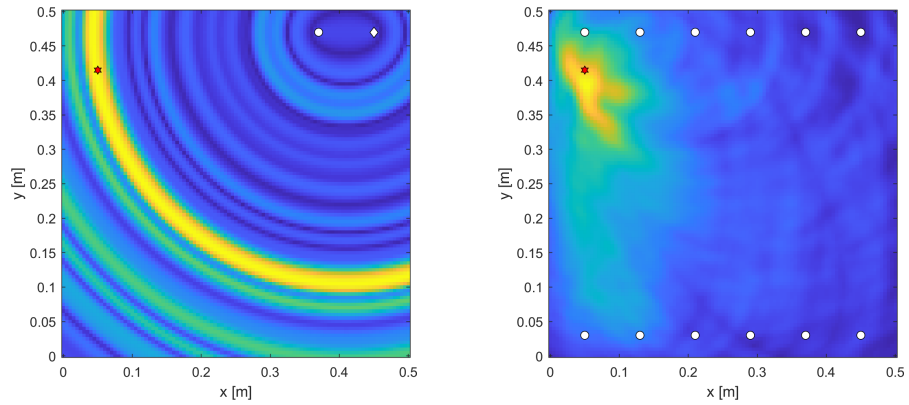

(a) (b)

Figure 5.9: DAS output images in a plate–like structure. (a) Single transmitter–receiver pair. Diamond and circular markers are the transmitter and receiver sensors, respectively. Meanwhile the red star represents the damage. (b) Final DAS output after the summation. White dots are the PZT sensors.

point of the spatial grid by applying appropriate phase sets for the compensation of the differences in time of arrivals (backpropagation). A baseline dataset acquired in pristine conditions can be exploited as a reference for enhancing scatters contribution. In particular, following Eq.5.21, ellipses will be drawn in the resulting image if one or more discontinuities exists. For instance, in Fig.5.9a the ellipse generated by a scatter point in a plate–like structure is depicted in yellow. The red star represents the damage position, while the diamond and circular markers are the transmitter and receiver sensors, respectively. Finally, the images obtained for each transmission event are summed together in order to reveal the scatter location, as depicted in Fig.5.9b. From a mathematical point of view, the general DAS main equation can be expressed

as:

$$y_{DAS}(x,y) = \sum_{i=1}^{N_T} \sum_{j=1}^{N_R} w_{ij} s_{ij}(\tau_{ij}^{xy}) \tag{5.24}$$

where N_T and N_R are the number of transmitters and receivers, respectively. $s_{ij}(\tau_{ij}^{xy})$ is the delayed time signal related to the $i{-}th$ transmitter at coordinates (x_i, y_i) and the $j-th$ receiver in (x_j, y_j). It's worthy to notice that $N_R = N_T - 1 = N - 1$ if pitch catch measurements in round–robin fashion are exploited, where N is the total number of sensors. The propagation time delay τ_{ij}^{xy} of a GW, instead, that travels from the transmitter to the receiver passing through a generic point located at (x, y) can be defined as:

$$\tau_{ij}^{xy} = \frac{\sqrt{(x_i - x)^2 + (y_i - y)^2} + \sqrt{(x_j - x)^2 + (y_j - y)^2}}{c_g} \tag{5.25}$$

where c_g is the GW group velocity that in anisotropic media depends on the propagation direction. Finally, w_{ij} is a weighting function. In conventional DAS $w_{ij} = 1 \forall (i,j)$. Nevertheless, many weighting strategies are adopted in literature for improving image reconstruction. For instance, Michaels et al. [267], exploited w_{ij} to compensate the reduction in amplitude with the square root of the distance, such as reductions in amplitudes due to transducers bonding variations. Zhang et al. [268], instead, defined the weighting factors as sparse coefficients in time-domain specific to the *i-th* transmitter and *j-th* receiver for reducing the influence of interference waves. Regarding the propagation time delay, Eq.5.25 shows the dependency between the propagation time and the group velocity. In general, the *a–priori* knowledge of the group velocity is not trivial in some application cases, since dispersion and multimodal propagation of Lamb waves affect signals integrity. If the material properties are partially or not known and it is not possible to simulate the GWs behaviour by means of numerical tools, such as SAFE models [134], experimental extraction of the group velocity can be performed. Threshold cross-

ing [267] and threshold–based double–peak techniques [220], cross–correlation methods [269], and time–frequency methods [270] can be exploited to determine the wave time of arrival and thus, the group velocity. Alternatively, dedicated measurement strategies can be performed to address this task. In particular, Semi-Analytical Finite Element (SAFE) measurements have been widely exploited for extracting the dispersion curves of materials. Among all the different signal processing techniques, Matrix Pencil Methods [271, 272], DRLSE method [AP10] and genetic algorithms [155] can be addressed for this purpose. In isotropic and *quasi*–isotropic materials, the experimentally estimated group velocity of the fundamental wave mode can be directly included in the propagation model. In non–isotropic plates, instead, velocity compensation is required to address the propagation complexity of Lamb waves. As a result, the elliptical model fails, since non–elliptical or *quasi*–elliptical curves characterize the relationship between each transmission–receiver pair and the damage position [266] [273]. Another aspect to take into account is the sensitivity of the algorithm to different environmental and operational conditions. In particular, DAS usually relies on baseline subtraction to enhance the scatter contribution w.r.t. measurements on the plate in pristine conditions. The method is straightforward and very simple to implement. As a drawback, baselines measurements are affected by fluctuations due to temperature and humidity variation over time. In particular, thermal effects such as thermal expansion and temperature-induced changes to the transducers and their bonds might significantly reduce the quality and reliability of the beamforming approach. To tackle this issue, multiple labelled baselines signals over a range of temperatures can be acquired [274]. Thus, the Optimal Baseline Subtraction (OBS) can be applied in the baseline subtraction knowing the temperature during the inspection measurement. Nevertheless, the method requires large

datasets. As an alternative, compensation strategies can be applied. Baseline Signal Stretch (BSS) modifies a single baseline time signal to match the current time signal. Croxford et at. [275] compared the performance of BSS and OBS. Then, a methodology that exploits both OBS and BSS is introduced, demonstrating that the combination of the two techniques is a robust and practical solution for temperature compensation. Salmanpour et al. [276], studied the performance of DAS applied to a plate subjected to vibration and temperature variations. The same author proposed a baseline signal stretch method with an improved minimum residual allowing temperature correction over a larger temperature range [277]. Nokhbatolfoghahai et al. [278], instead, evaluated the robustness of DAS under multiple environmental and operational conditions, such as temperature–variation, boundary–reflection, SNR, error in sensor placement, error in the calculation of wave-speed and number of PZTs. In particular, a methodology based on the Taguchi method was exploited. As a final consideration, dispersion has to be considered. In fact, dispersion directly affects the accuracy of the time of arrival of the GWs by generating broadening of the uncertainty zone of the DAS ellipse which leads to fuzzy final image reconstruction. Usually, narrowband excitation frequencies [224] are exploited to reduce the dispersion effect. On the other side, compensation techniques can be adopted. For instance, Fu et al. [279] computed DAS in conjunction with the dispersion compensation method based on Warping Frequency Transform developed by De Marchi et al. [188], demonstrating the enhancement of the final result w.r.t. conventional DAS and time-reversal method. Moll et al. [252] estimated signals time of arrival exploiting dispersion compensation based on Warping Frequency transform as well. Then, compensated signals were used for comparing four different beamforming techniques, *i.e.* delay and sum, weighted coherence-factor, channel rank and Capon beamformer. Finally,

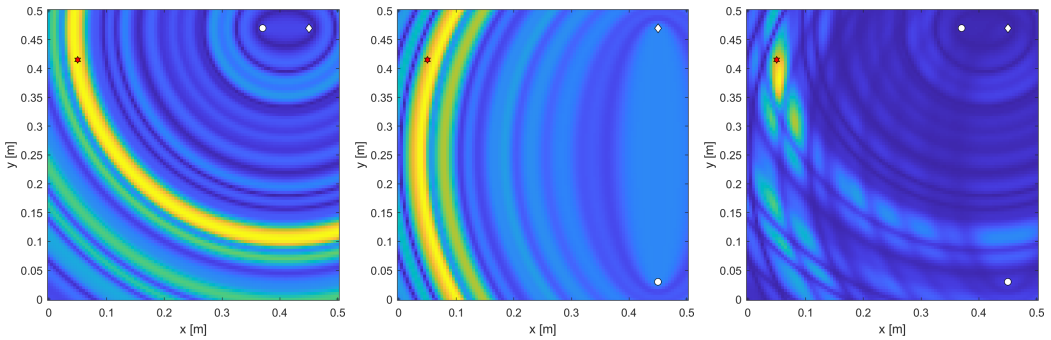

(a) (b) (c)

Figure 5.10: DMAS output images in a plate–like structure for a specific Tx–Rx pair. (a) First Tx–Rx pair imaging output; (b) Second Tx–Rx pair imaging output; (c) Imaging output after multiplication.

a nonlinear data-fusion technique that takes as input the results of the previous methods was presented. Hall et al. [280], instead, demonstrated the significant imaging performance that can be achieved by incorporating phase information into the imaging algorithm and the necessity for adaptive parameter compensation. In fact, conventional imaging algorithms usually are restricted to using the envelope of narrowband signals which feature minimally dispersive characteristics. By exploiting adaptive dispersion estimation obtained from *in–situ* measurements, it is possible to use the phase information for achieving better imaging quality.

5.2.3 DMAS

DMAS can be considered as an improved version of the classic DAS algorithm. In particular, a nonlinear multiply operation among combinatorially coupled signals is performed before summation. As a result, uncorrelated samples are lowered, reducing noise and artefact. On the other hand, correlated samples are intensified enhancing the scatter contribution. In such a way, DMAS achieves

better imaging resolution, contrast and image dynamic range. For sake of clarity, in Fig.5.10, DMAS main idea is shown. In Fig.5.10a and Fig.5.10b, the imaging outputs for the transmitter i and two generic receivers (j, k), respectively, are depicted. The single pairs (Tx_i, Rx_j) and (Tx_i, Rx_k) draw an ellipse passing through the damage position, as expected. The imaging result after the multiplication of these contributions is shown in Fig.5.10. By exploiting the multiplication operation, the damaged area is significantly shrunk, while noise is reduced. If a single transmitter i is exploited, DMAS–beamformed output for any point (x, y) can be written as:

$$y^i_{DMAS}(x,y) = \sum_{j=1}^{N_R-1} \sum_{k=j+1}^{N_R} s^w_j(\tau^{xy}_j) s^w_k(\tau^{xy}_k) \tag{5.26}$$

where $s^w_{j,k}(t^{xy}_{j,k}) = w_{j,k} s_{j,k}(t^{xy}_{j,k})$ are the weighted back propagated signals referred to the j-th and k-th receivers, respectively, passing through (x, y). Moreover, it's worthy to mention that in Eq.5.26 auto-product terms are not considered and the coefficients are halved due to reciprocity [281]. By extending the method for all the transmitter–receiver pairs, Eq.5.26 becomes as follows:

$$y_{DMAS}(x,y) = \sum_{i=1}^{N_T} \sum_{j=1}^{N_R-1} \sum_{k=j+1}^{N_R} s^w_{ij}(\tau^{xy}_{ij}) s^w_{ik}(\tau^{xy}_{ik}) \tag{5.27}$$

In the case of pitch–catch measurements in round–robin configuration, $N_R = N_T - 1 = N - 1$.

Finally, the same considerations as in the DAS case can be raised. The weighting function can be defined as $w = 1$ in conventional DMAS, but many different exceptions can be addressed as already discussed. Similarly, the estimation of the group velocity, the sensitivity to environmental and operational conditions such as multimodal and dispersive behaviour of Lamb waves can affect the final imaging output. In this work, DMAS is introduced for NDT and SHM application fields. The capabilities of the method are quantitatively

characterized and compared with conventional DAS by means of metrics in the following.

SHM experimental setup

Disclaimer: the following section was previously published in [AP8]

The DMAS validation in an SHM scenario has been carried on data from the online platform Open Guided Waves described in Moll et al. [145]. The specimen is a Carbon Fibre Reinforced Plate (CFRP) plate based on prepreg material Hexply M21/34%/UD134/T700/300 with dimensions 500 mm x 500 mm x 2 mm and layup $[45/0/-45/90/-45/0/45/90]_S$. Twelve DuraAct lead-zirconate-titanate (PZT) circular disk transducers of 0.2 mm in thickness and 5 mm in diameter were attached on the plate as depicted in Fig.5.12 (white circles). During the signals acquisitions, the plate was placed in a climate chamber at a controlled constant temperature of 23° and 50% RH. Data has been acquired in round–robin pitch–catch configuration, exploiting a ±100 V, 5 cycles, Hann-filtered sine wave as excitation signal. A reversible defect model made of an aluminium disk of 10 mm of diameter is mounted on the surface of the CFRP plate by a tacky tape to mimic a damaged condition. The entire dataset is composed of 60 baseline and 28 different damage position measurements for each narrowband excitation frequency. In particular, excitation frequencies from 30 to 240 kHz with a frequency step of 20 kHz were exploited. In particular, the 60 kHz excitation dataset has been used for characterizing the DMAS performance at this stage.

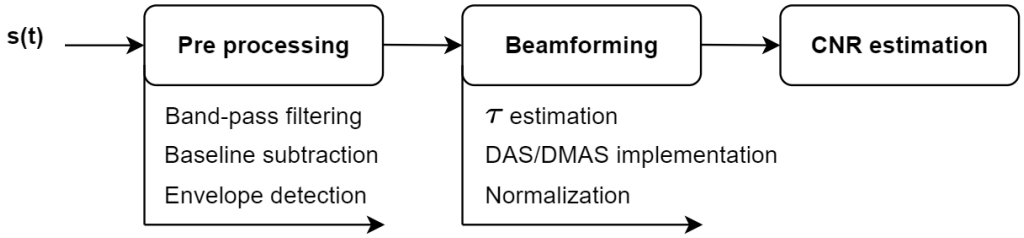

Figure 5.11: Algorithm chain [AP8]

Processing

Disclaimer: the following section was previously published in [AP8]
Since the described algorithms are sensitive to many different factors (*e.g.* environmental variation, dispersion, multimodal propagation etc.), some preliminary observations must be carried out. Single A0 mode propagation was supposed since the wavelength tuning behaviour of the PZT transducers peaks at 80 kHz for the A0 mode as demonstrated in [145]. Then, due to the *quasi*–isotropic behaviour of the material, the A0 group velocity has been considered in the first approximation as constant and estimated by SAFE simulations. Moreover, dispersion and noise have been limited by exploiting a bandpass filter centred at 60 kHz, from 40 to 80 kHz. Finally, specific temperature compensation was not required since the CFRP was placed in a controlled environment, i.e. a climate chamber.

The algorithm steps adopted for processing raw data is schematically depicted in Fig. 5.11. In the first block, after filtering, signals are subtracted with a reference signal, a.k.a. baseline, acquired in pristine conditions to highlight the mismatch when damage occurs. Then, the Hilbert transform has been performed to obtain envelope–detected differenced signals. In fact, during the sum operation in the beamforming algorithm, signals might be affected by phase cancellation even if the signal envelopes are in alignment due to dis-

persion [282]. After the pre–processing phase, the beamforming techniques are applied, providing as output the normalized images which represent the health condition of the plate in spatial coordinates.

As a final step, DAS and DMAS are directly compared by the Contrast to Noise Ratio (CNR) which was used as a metric to assess the damage image quality. The CNR can be defined as:

$$CNR = \frac{\mu_D - \mu_B}{\sigma_B} \tag{5.28}$$

where μ_D is the spatial average computed in the damaged area, μ_B and σ_B are the spatial average and standard deviation of the undamaged area, respectively. In order to compute the CNR metric, a circular region centered at the actual reversible defect model with radius 5 cm has been considered as damaged area. The complementary region has been considered as undamaged.

Results

Disclaimer: the following section was previously published in [AP8]
Results from the beamforming outputs are presented in Fig.5.12 for different damage positions. These results lead to some considerations. At first, DMAS improves the damage reconstruction in comparison with the DAS output by shrinking the colour gradient around the actual damage position, depicted as a black circle, and thus, both highlighting the damaged zone and reducing noise elsewhere. In fact, an increase of 18%, 22% and 14% of the CNR for damages D1, D9 and D22 respectively is achieved. It's worthy to notice that in the case of the damage D1 (Fig.5.12(a,b)), the images show a well–localized damaged zone, shifted on the left w.r.t. the actual damage position. The error is both due to the approximated constant group velocity used in the algorithms and the effect of reflections of the edges of the plate. Nevertheless, these aspects

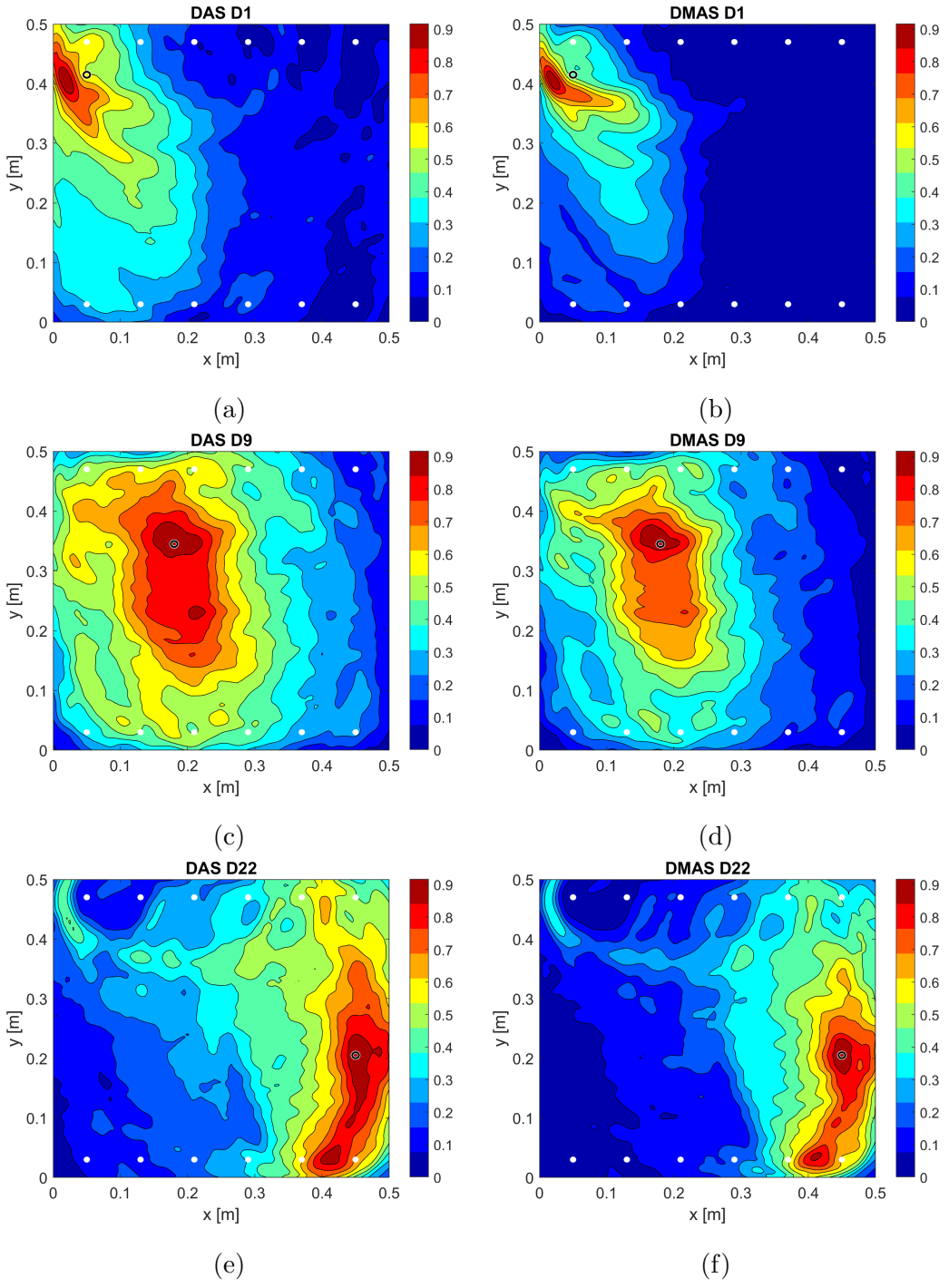

Figure 5.12: DAS (left column: a,c,e) and DMAS (right column: b,d,f) image output [AP8].

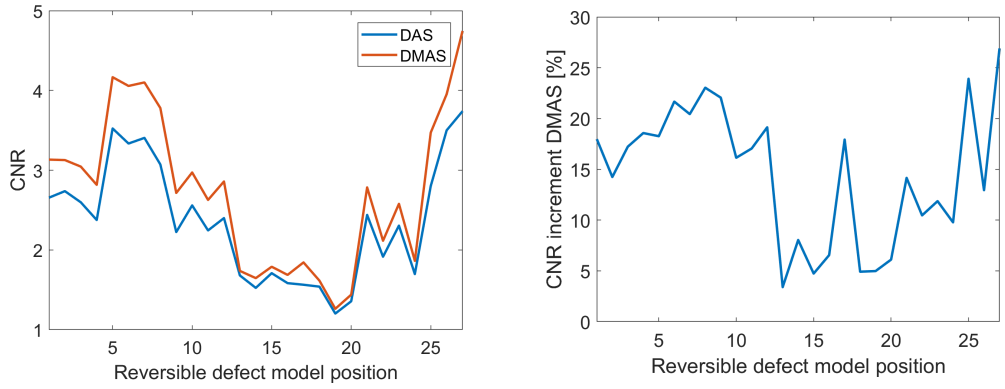

(a) (b)

Figure 5.13: (a) Comparison between DAS and DMAS CNR in terms of absolute value and (b) percentage increment of DMAS CNR with respect to DAS [AP8].

do not affect the considerations related to the DAS and DMAS capabilities comparison. Regarding the D9 imaging results (Fig.5.12(c,d)), instead, the damage region is wider and less focused with respect to the other cases presented, but still, the DMAS approach achieves better CNR w.r.t. DAS, with an increase of 22%. As a further step, the analysis has been carried out on the entire dataset in order to validate the algorithm for all 28 damage positions. Results are shown in Fig.5.13(a) where CNR values for each damage position are plotted for both DAS and DMAS cases. Moreover, the DMAS percentage increment in comparison with DAS is shown in Fig.5.13(b). Attention may be drawn to the fact that the DMAS algorithm provides a better CNR for each damage condition, with a mean increment of 14.5 % and a peak of 27 %.

The results achieved prove the suitability of the DMAS algorithm in the GWs based SHM application, by enhancing the image reconstruction in terms of contrast and resolution with respect to the DAS approach.

5.2.4 DS–DMAS

DS-DMAS is based on exploiting DMAS algebra by combinatorially coupling and multiplying the DMAS expansion terms. As a result, blurring would be prevented, and the effects of noise in the reconstructed images would be reduced w.r.t. conventional DAS and DMAS. Let's start from the expansion of DMAS main equation for a single transmitter i as follows:

$$\begin{aligned} y^i_{DMAS}(x,y) &= \sum_{j=1}^{N_R-1}\sum_{k=j+1}^{N_R} s^w_j(\tau^{xy}_j)s^w_k(\tau^{xy}_k) \\ &= \underbrace{[s^w_1 s^w_2 + s^w_1 s^w_3 + ... + s^w_1 s^w_{N_R}]}_{\alpha_1} \\ &+ \underbrace{[s^w_2 s^w_3 + s^w_2 s^w_4 + ... + s^w_2 s^w_{N_R}]}_{\alpha_2} \\ &+ ... \\ &+ \underbrace{[s^w_{N_R-1} s^w_{N_R}]}_{\alpha_{N_R-1}} \end{aligned} \tag{5.29}$$

The $y^i_{DMAS}(x,y)$ expansion has been divided into $N_R - 1$ terms addressed as α which are summed together. Thus, DMAS–beamformed main equation for a single transmitter can be rewritten in a more compact notation as:

$$y^i_{DMAS}(x,y) = \sum_{j=1}^{N_R-1} \alpha_j \tag{5.30}$$

Eq.5.30 reveals that DMAS exploits DAS algebra between its expansion terms α. The main idea of DS-DMAS, instead, is to use DMAS algebra between the DMAS expansion terms. Thus, the DS-DMAS beamforming main equation can be defined as:

$$y^i_{DS-DMAS}(x,y) = \sum_{j=1}^{N_R-2}\sum_{k=j+1}^{N_R-1} \alpha_j \alpha_k \tag{5.31}$$

Finally, by considering multiple transmitters i, Eq.5.32 can be rewritten:

$$y_{DS-DMAS}(x,y) = \sum_{i=1}^{N_T} \sum_{j=1}^{N_R-2} \sum_{k=j+1}^{N_R-1} \alpha_j \alpha_k \tag{5.32}$$

The same considerations of DAS and DMAS cases can be addressed for DS-DMAS. In fact, the algorithm requires the estimation of the group velocity and it is sensitive to dispersion, multimodal propagation and environmental effects in the baseline subtraction.

In this work, DS-DMAS has been tested and characterized in two different application scenarios. In the former, DS-DMAS is introduced for radar–based microwave breast imaging in 3–dimensional case. The algorithm has been tested and validated by comparing the imaging results w.r.t. DAS and DMAS approaches. In the latter, instead, DS-DMAS is applied to NDT/SHM case, demonstrating the method suitability even in this application scenario. Moreover, a filtering technique for artefacts suppression is presented to further enhance the imaging quality.

5.2.5 Radar–based microwave breast imaging

Disclaimer: the following section was previously published in ©IEEE [AP9].
Breast cancer is the most common cancer which affects women worldwide. Early–stage diagnosis is fundamental for a successful treatment. Nowadays, X–ray mammography, ultrasound and Magnetic Resonance Imaging (MRI) are the most exploited techniques for cancer detection and evaluation. Each technique can be characterized by many factors, such as radiation exposure, sensitivity and costs. Anyway, other approaches have been investigated as well. In particular, one of the most promising alternative methods is broadband microwave radiation [283]. In fact, Microwave-based Imaging (MI) detection techniques are inexpensive, non–invasive, non–ionizing, and are an overall

comfortable form of treatment. Moreover, MI provides high–resolution images able to detect small tumours. The main idea is to exploit the contrast of electrical properties, *i.e.* permittivity and conductivity, between healthy and tumourous tissues. In particular, radar–based techniques use an external microwave source to illuminate breast tissue with Ultra-Wideband (UWB) signals. Scattering signals are then exploited to detect breast tumours. The diagnosis accuracy depends on how signals obtained from Multiple Inputs Multiple Outputs antennas, *i.e.* MIMO approach, are transferred to a meaningful medical image. Thus, the effort of many studies has been focusing on the development and optimization of confocal image reconstruction techniques. Among many, DAS [284], DMAS [285], Difference Time of Arrival (DToA) [286], channel–ranked beam–forming [287] and also compressed sensing based image reconstruction techniques [288,289] have been investigated in literature. In this work, the DS-DMAS is introduced for microwave biomedical imaging in a 3–dimensional case. In particular, the image quality is quantitatively evaluated against conventional DAS and DMAS using metrics such as Signal-to-Noise Ratio (SNR), Contrast-to-Noise Ratio (CNR), and Contrast Ratio (CR).

Simulation setup and Results

Disclaimer: the following section was previously published in ©IEEE [AP9]. The available dataset proposed in [286] has been exploited for characterizing the algorithms. The arrangement of the 15 transmitters and 15 receivers is shown in Fig. 5.14. Moreover, a point–like radar target depicted as an 'x' models the tumour, which is supposed to be located in a homogeneous dielectric environment with fibroglandular tissue properties. Each transmitter sends a spread spectrum waveform based on a Gold sequence of length 2^8-1 at a carrier frequency of 2 GHz. All receiver elements demodulate the recorded

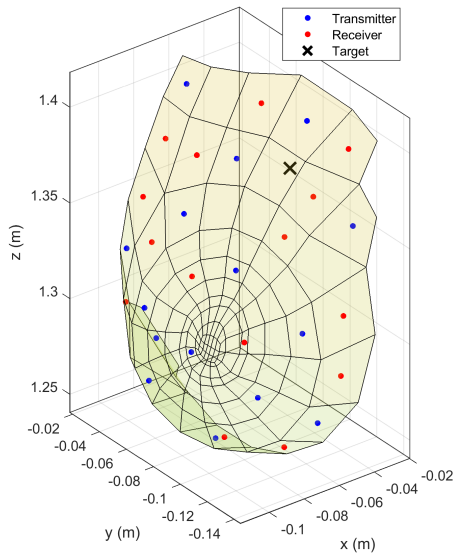

Figure 5.14: Visualization of the imaging domain showing the transmitters, receivers and the tumour (modeled as a point target) [AP9].

signal mixture by a matched filter to obtain the echo signals $s(t)$ that are used subsequently during image reconstruction.

In Fig. 5.15, instead, the imaging outputs for DAS, DMAS and DS-DMAS beamforming are shown. Three breast sections are depicted, *i.e.* along with $x - y$ dimension in the first column, $x - z$ in the second column and $y - z$ in the third column. Conversely, the imaging outputs in the same row were generated by the same imaging technique. In particular, DAS, DMAS and DS-DMAS outputs are shown in the first, second and third row starting from the top, respectively. It can be observed that DAS output features high levels of artefacts, blurring and noise which are significantly reduced in the DMAS imaging. Nevertheless, DMAS is still characterized by noise mostly around the tumour point. Conversely, DS-DMAS output shows an overall improvement in terms of resolution, noise reduction and artefacts suppression. Thus, DS-

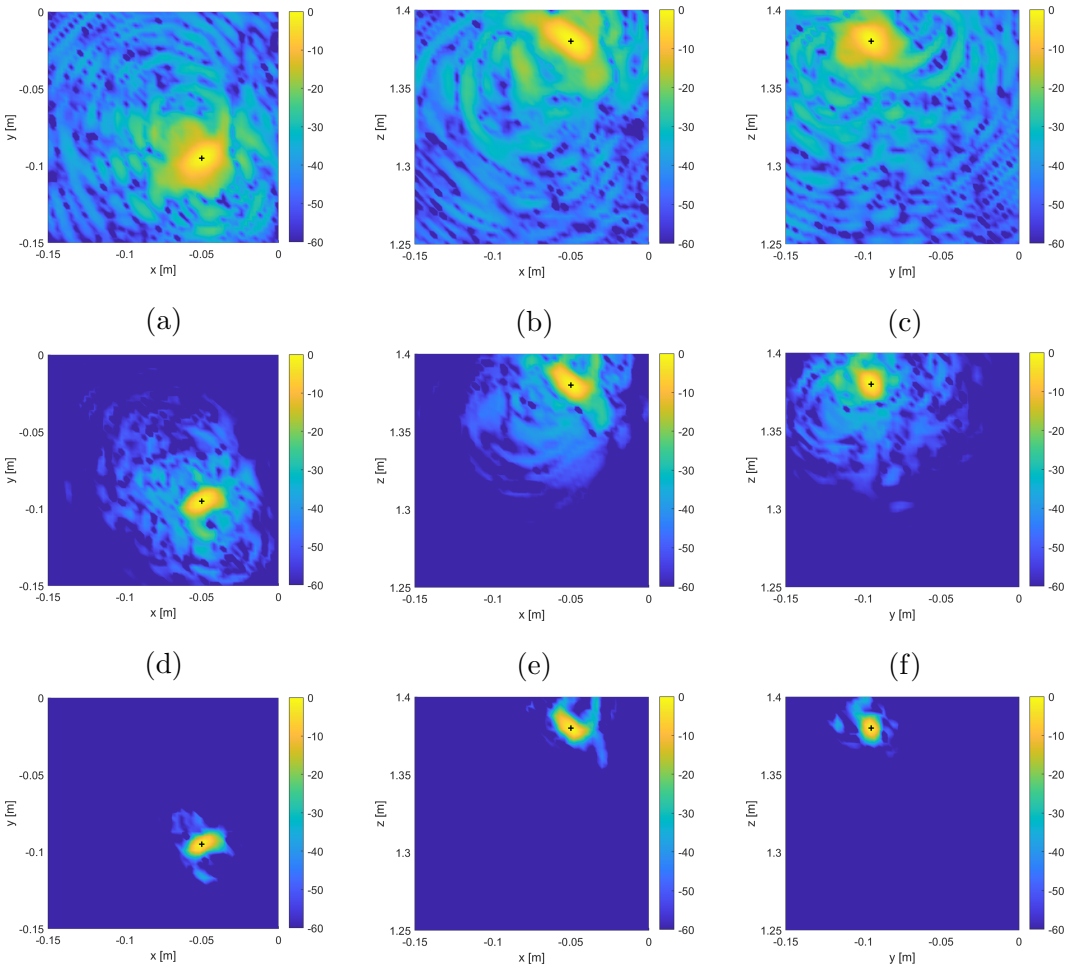

Figure 5.15: Imaging output at three different breast sections, *i.e.* x-y, x-z and y-z. In particular, DAS (a,b,c), DMAS (d,e,f) and DS-DMAS (g,h,i) outputs are shown. The black cross is the actual tumour position [AP9].

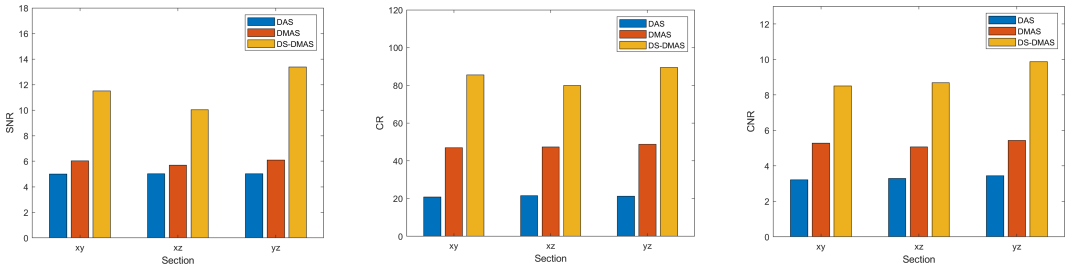

(a) (b) (c)

Figure 5.16: SNR (a), CR (b) and CNR (c) values at each breast section for DAS, DMAS and DS-DMAS approaches [AP9].

DMAS output is the most performative in terms of tumour recognition from an external observer. To quantitatively describe the performance of the methods, three classic metrics were adopted: SNR, CR and CNR. At first, a circular region around the point-like target is defined as Region of Interest (RoI). RoI radius is 5 mm of radius, which is in the order of the tumour size that should be detected in this microwave frequency range. Thus, metrics can be computed following [290]:

$$SNR = \frac{\mu_i}{\sigma_o} \tag{5.33}$$

$$CR = 20 * log_{10}(\frac{\mu_i}{\mu_o}) \tag{5.34}$$

$$CNR = \frac{|\mu_i - \mu_o|}{\sqrt{\sigma_i^2 + \sigma_o^2}} \tag{5.35}$$

where $[\mu_i, \sigma_i]$ and $[\mu_o, \sigma_o]$ are the expectation and the variance values of the pixels intensity inside and outside RoI, respectively. In Fig. 5.24 the main results are depicted. The trend is the same in all the three metrics, in which DMAS outperforms DAS while DS-DMAS outperforms both DAS and DMAS. The average improvements among different sections between DS-DMAS w.r.t. DMAS and DAS are summed up in TABLE 5.1. According to these results,

SNR		CR		CNR	
DAS	DMAS	DAS	DMAS	DAS	DMAS
127.5%	95.4%	300.8%	78.1%	171.7%	71.1%

Table 5.1: Percentage improvement of the DS-DMAS approach w.r.t. DAS and DMAS for each metric

the overall better performance of DS-DMAS in terms of image contrast, noise suppression and image resolution is evident.

5.2.6 DS–DMAS imaging in SHM

In this section, DS-DMAS has been implemented and compared with DAS and DMAS algorithms in an SHM case as well. A multi–frequency analysis is carried on to provide a robust characterization of the techniques. Results are presented both as imaging outputs, to visually evaluate the localization capabilities of the methods, and by means of metrics to quantitatively characterize the images.

Setup

The online free data set for guided waves inspection (http://openguidedwaves.de/) which collects piezo pitch–catch 5 cycles, Hann-filtered sine wave signals travelling through a *quasi* isotropic CFRP at different actuated frequencies and damage positions has been used in this work. The plate and the experimental setup is described in Section 5.2.3. Nevertheless, in this case, datasets from 160 kHz to 240 kHz with a frequency step of 20 kHz were exploited for a deepening investigation. In particular, the specific frequency range has been chosen in order to have a single–mode with a predominant symmetric S0 mode prop-

agation which leads to a *quasi* isotropic plate behaviour, as described in [145].

Processing and Results

Disclaimer: the following section was previously published in ©IEEE [AP5]. The beamforming algorithms were applied to the datasets. In particular, 60 baselines of each dataset were averaged to synthesise a more robust baseline. In fact, by averaging the baselines, outliers and non–correlated noise are minimized. Thus, no optimal baseline selection method was required. Similarly, no dispersion compensation was needed, since a narrowband excitation signal was exploited [224]. Due to the wavelength tuning behaviour of the PZT transducers, a single S0–mode propagation was assumed. Then, the S0 polar group velocity profile at the excitation frequency $c_g(\theta, f_{ex})$ was computed by SAFE simulation [134]. Due to the *quasi*–isotropic velocity profile of the S0 mode at the excitation frequencies, a constant velocity obtained by averaging $c_g(\theta, f_{ex})$ was considered as a fitting approximation.

Under these assumptions, DAS, DMAS and DS-DMAS beamforming methods were performed. At first, signals were filtered in a frequency band from $f_c - {}^{f_c}/_4$ to $f_c + {}^{f_c}/_4$ for reducing noise and dispersion effects. Then, residuals are computed by baseline subtraction. Finally, beamformers are applied and a spatial damage influence map is synthesized. For instance, in Figs.5.17a, 5.17b and 5.17c the normalized imaging outputs of the three algorithms in the case of excitation frequency of 200 kHz are shown. The white dots represent the sensors placed on the plate, while the black circle is the damage location. It is evident that the noise suppression capabilities improve from the DAS approach, which is the noisiest, to DS-DMAS case which shows a low noise level. In Figs.5.17d, 5.17e and 5.17f, instead, the damaged area is magnified for a better visualization of this region. It can be noticed that the resolution and

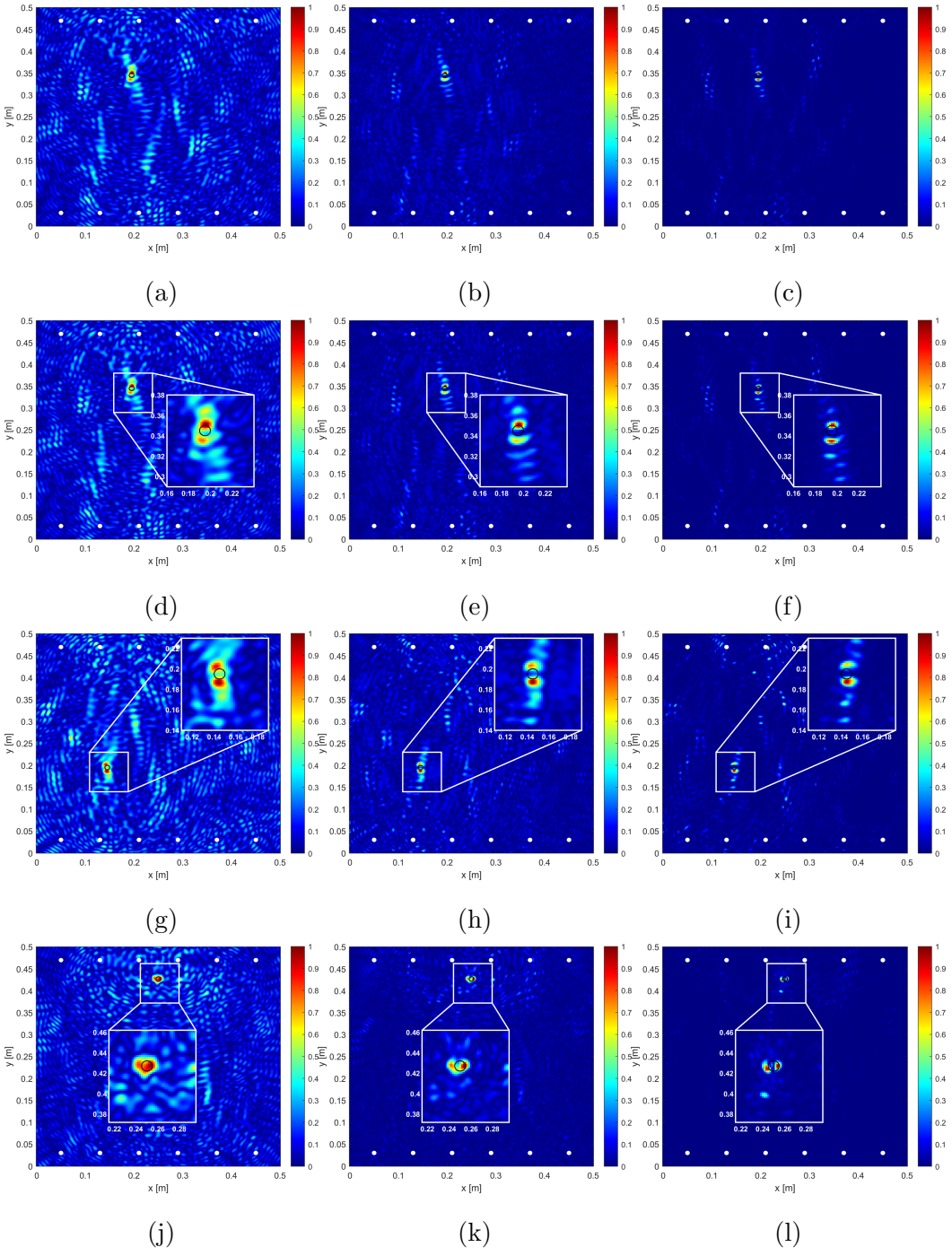

Figure 5.17: In the first row, (a) DAS, (b) DMAS and (c) DS–DMAS at the excitation frequency of 200 kHz are shown. In the second row, the same results are depicted with the damaged zone magnified. In the third and fourth rows, (g,j) DAS, (h,k) DMAS and (i,l) DS–DMAS are computed for two different damage positions. [AP5]

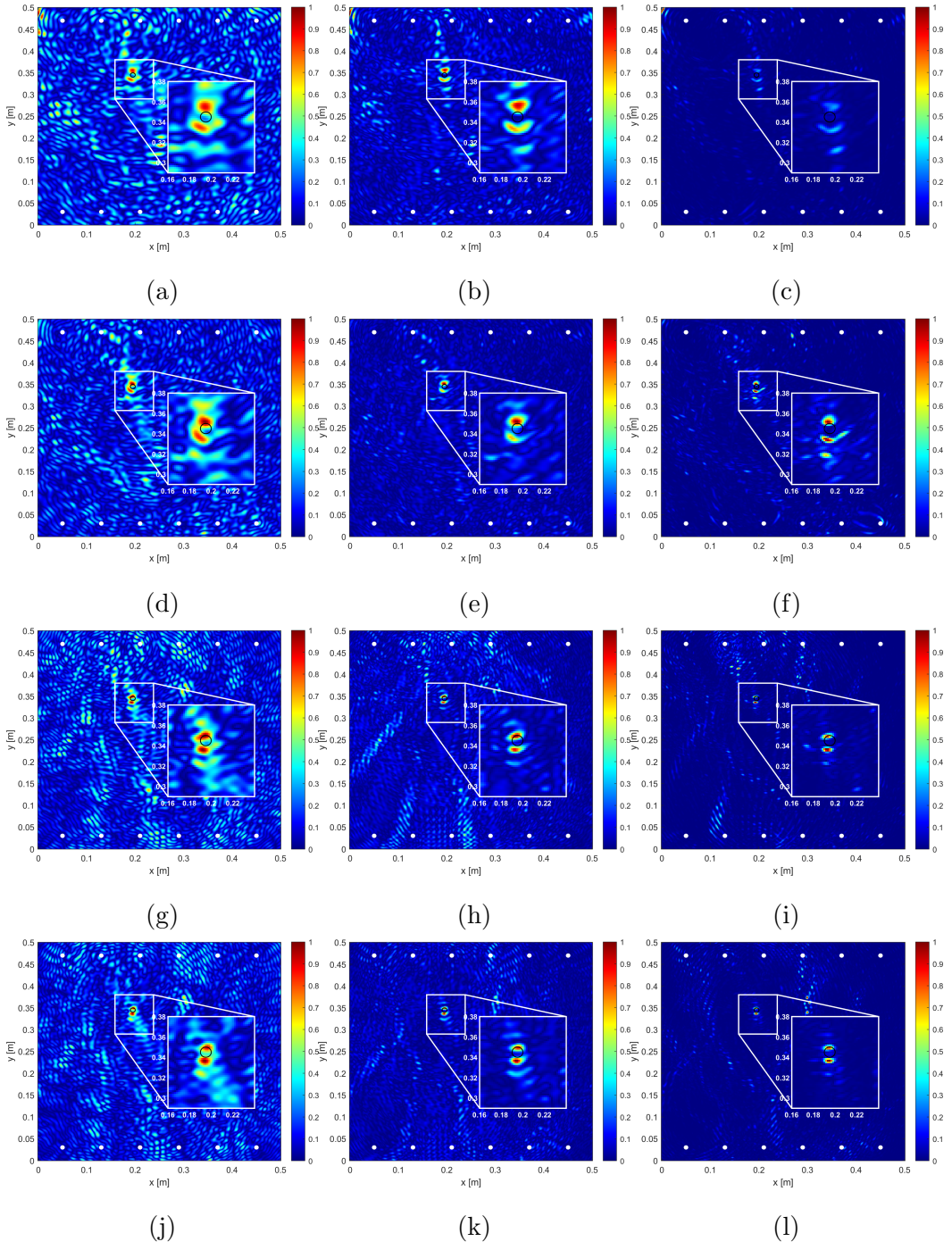

Figure 5.18: Imaging outputs at different excitation frequencies. das, DMAS and DS–DMAS are plotted in the first, second and third column from left to right, respectively. Beamforming output from datasets at excitation frequencies of 160 kHz (a,b,c), 180 kHz (d,e,f), 220 kHz (g,h,i) and 240 kHz (j,k,l) are plotted.

damage detection capabilities are enhanced as well, due to stronger contrast and a shrink of pixels at a high intensity around the damage. In fact, the beamformings are seemingly able to map the impedance discontinuities of the reversible defect model, a.k.a. the edge of the aluminium disk, especially in the DS-DMAS case where noise is minimized. The same considerations can be addressed for Figs. 5.17g, 5.17h, 5.17i.5.17j, 5.17k and 5.17l, where the imaging results for damages at different positions at 200 kHz are shown. Nevertheless, even if noise is almost fully suppressed in the DS-DMAS output, some artefacts are still present. In this case, artefacts are intrinsic to the experimental setup, since they are mostly due to the reflections of scattered waves, which are generated by the damage, along the plate edges.

In Fig.5.18, instead, it is possible to observe the imaging outputs for datasets at different excitation frequencies. DAS, DMAS and DS-DMAS imaging outputs are depicted in subplots of the first, second and third column from left to right, respectively. Meanwhile, subplots along rows belong to datasets at excitation frequencies of 160 kHz, 180 kHz, 220 kHz and 240 kHz, from top to bottom respectively. The imaging results are overall coherent with the expectations and the same considerations of the 200 kHz case can be raised. In general, the imaging results seem to be more precise and effective at 200 kHz and above, due to a more isotropic behaviour of the S0 mode. For this reason, at 180 and 160 kHz the resolution is lower and a blurry effect can be observed. Anyway, the damage can be perfectly localized and it does not affect the final result. The only exception is Fig.5.18c where DS-DMAS can not provide a satisfactory result. In fact, due to the highly non–linear characteristic of the method, DS-DMAS drawback is the more accentuated sensitivity to inaccuracies of group velocity estimation and mismatches of the baseline due to operational and environmental conditions. By applying specific filtering tech-

niques, this aspect can be tackled. By using the same filters, artefacts can be suppressed as well. In this work, the Fresnel Zone Filtering (FZF) technique is introduced. The main idea is to transform the ideal ultrasonic ray which passes through the transmitter–receiver positions and the scatterer point, which can be easily defined by the standard ray–tracing theory, into a physical ray of finite thickness. Thus, the waves backpropagation can be restricted in the constructive inference zone of scattered waves, a.k.a. the first Fresnel zone, by means of weighting coefficients. This technique is an adaption of the Fresnel volume migration which is commonly adopted for reconstructing subsurface structures from seismic wavefields [291, 292].

Fresnel Zone Filtering

Disclaimer: the following section was previously published in ©IEEE [AP5].
The Fresnel zone filtering consists in focusing the ultrasonic beam around the actual scatterer, by restricting the backpropagation region. The conventional Fresnel migration method for seismic imaging as described in [291], can not be directly applied to an SHM application scenario. In fact, in plate–like structures edges reflections such as multimodal and dispersive propagation of Lamb waves do not permit a reliable and accurate migration procedure based on cross–correlation methods [293] or slowness analysis [294]. Thus, an adaption of Fresnel Migration for SHM imaging is implemented as follows. The beamforming algorithm is performed twice. In the first run, the damage location is estimated, enabling the focus on that damage point. The ray between the receiver, the reflection point and the virtual source, defined as the point where the wave would start if it propagates in a straight line along with the receiver–damage line, is determined. Then, the Fresnel zone is computed on this ray. The first Fresnel zone radius in a homogeneous medium can be ex-

pressed as [292]:

$$r_F = \sqrt{\frac{3}{4}\frac{\lambda x(L-x)}{L}} \tag{5.36}$$

where λ is the wavelength of the direct wave, L is the transmitter–receiver distance and x is the length of the projection of a generic scatterer on the wave direct path. From the Fresnel zone radius, the Fresnel weighting function can be computed as [291]:

$$w_{FZF} = \begin{cases} 1 & d \leq r_F \\ 1 - \frac{d-r_F}{d} & r_F < d < 2r_F \\ 0 & d \geq 2r_F \end{cases} \tag{5.37}$$

where d is the distance between the image point and its nearest point on the previously determined ray. FZF limits the beamforming imaging in the first Fresnel zone where any scatterer point interferes constructively with the direct wave. In such a way, both beamforming artefacts and noise are attenuated and the damage scattering profile is enhanced. Neubeck et al. [295] introduced this concept for model–based beamforming in SHM field, but it has never been applied in conjunction with DMAS and DS-DMAS techniques.

Beamforming with Fresnel Zone Filtering approach

Disclaimer: the following section was previously published in ©IEEE [AP5]. A comparative analysis has been carried on to validate and characterize the Fresnel zone filtering. FZF is divided into two phases which are addressed as localization phase and filtering phase. In the localization phase, the beamforming algorithm is performed with a constant weighting factor $w = 1$. Then, an estimation of the damage position is computed. In particular, pixels intensity of the beamforming imaging output which are above a certain threshold are selected. By considering a normalized swing $[0, 1]$, a threshold of 0.8 has been

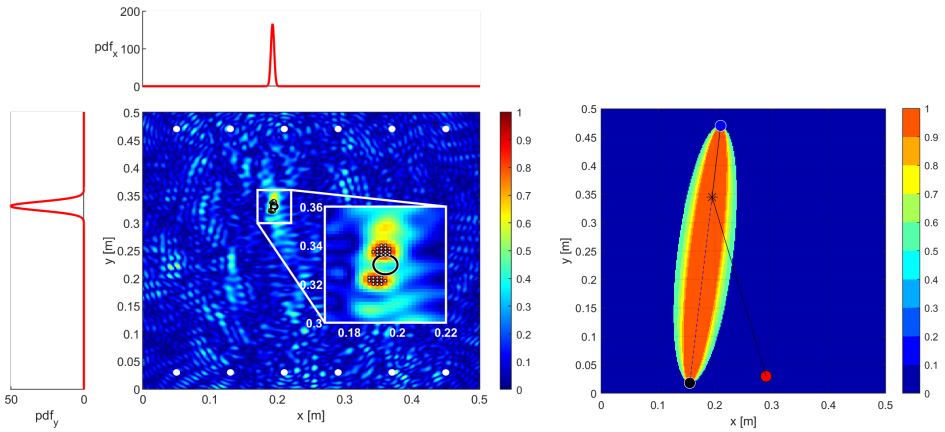

(a) (b)

Figure 5.19: (a) Localization method: DAS output where over-threshold intensity pixels are depicted as grey dots. The distributions of these pixels along x and y axes are shown on the top and left, respectively. (b) Fresnel weighting function in Cartesian coordinates [AP5].

used in this work for all the beamforming algorithms. Afterwards, probability density functions of the distribution of the selected pixels along each axis are derived. In particular, a normal distribution has been exploited. Finally, the damage position is estimated as the location of the peaks of the distributions. In Fig.5.19a a localization example is depicted. The figure shows the DAS output where the damaged area is magnified. Pixels whose intensity is above the threshold are highlighted with grey dots. On the top and on the left, the probability density functions of the grey dots distribution along the x–axis, pdf_x, and y–axis, pdf_y are shown, respectively. The difference between the peak values of the two distributions can be explained by considering the spatial pixel density which is higher along x–axis. Once the damage position is estimated, the FZF can be implemented in the filtering phase. At first, the Fresnel zone and its corresponding weighting function w_{FZF} are computed for

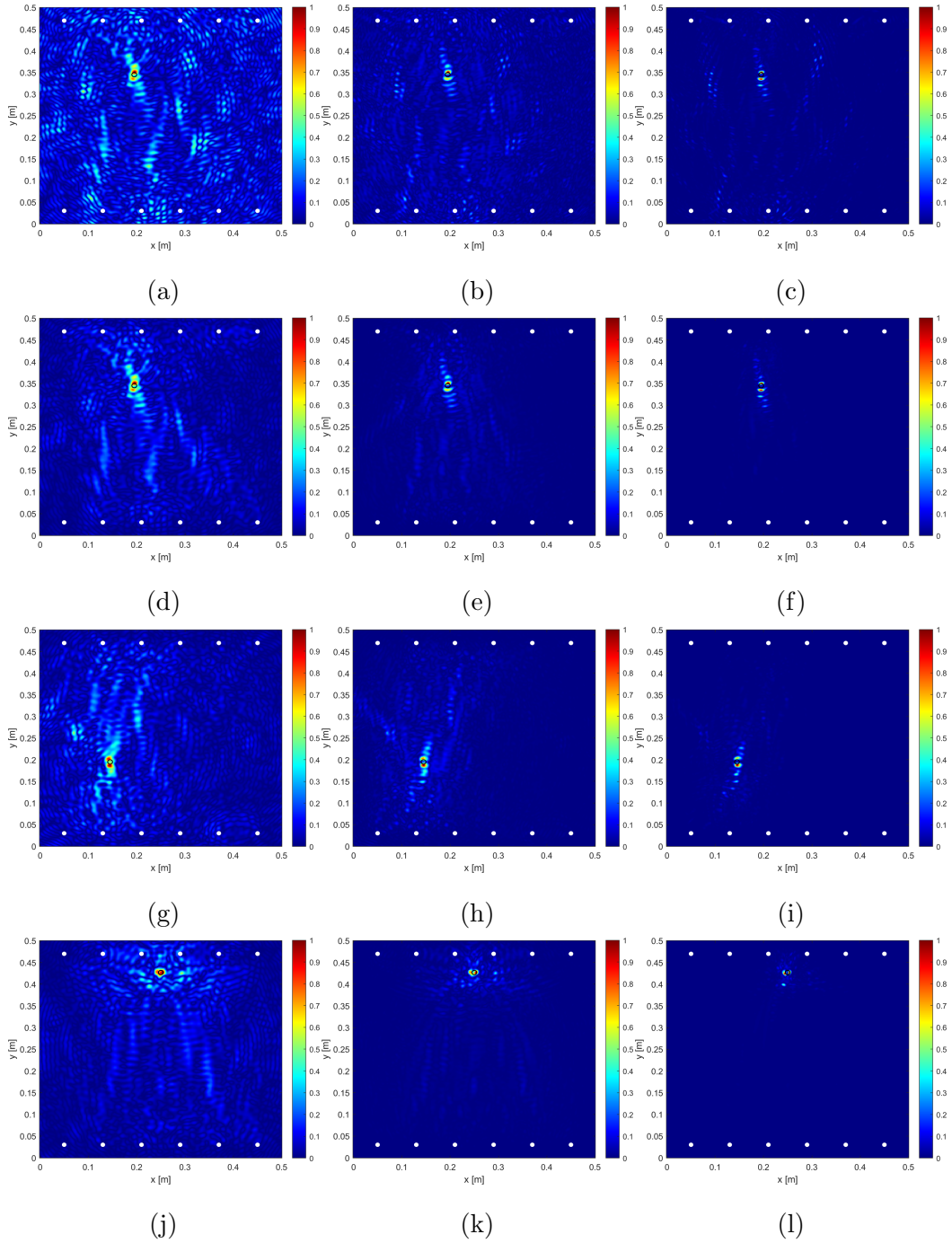

Figure 5.20: DAS, DMAS and DS–DMAS are shown in columns from left to right, respectively. Rows are organized as follows. In the first and second rows, imaging outputs without and with FZF are depicted, respectively. In the third and fourth rows, instead, imaging output at two different damage positions are plotted. The excitation frequency of the dataset is 200 kHz [AP5].

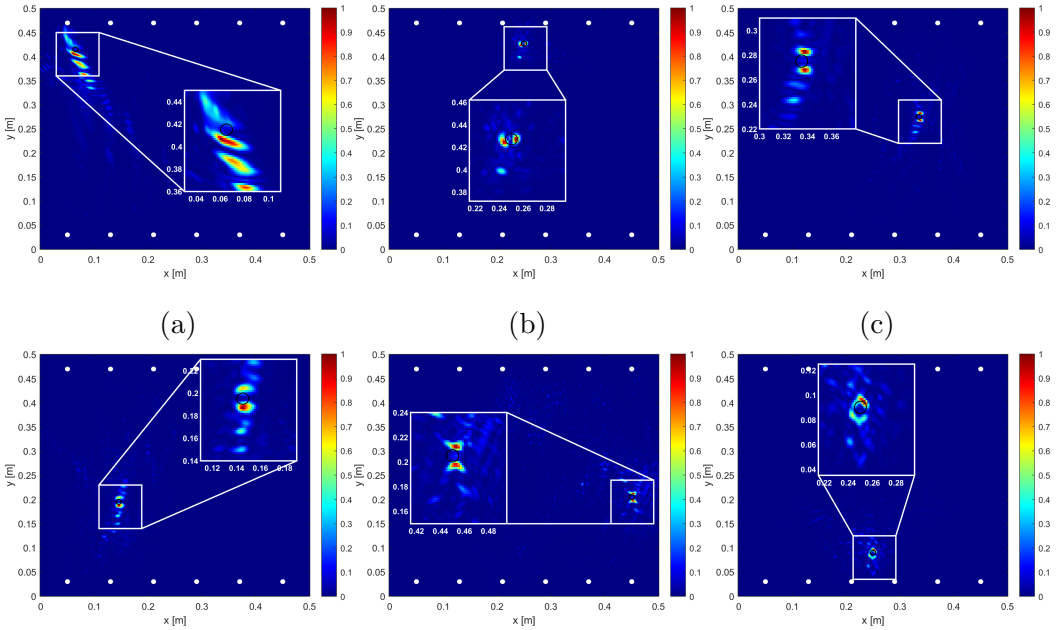

Figure 5.21: DS–DMAS with FZF imaging results for six different damage locations at the excitation frequency of 200 kHz [AP5].

each Tx–Rx pair and the estimated damage position. Then, the imaging algorithm is carried on again by using $w = w_{FZF}$ in the beamformer main equation. An example of a 2D Fresnel zone is depicted in Fig.5.19b. The receiver sensor, such as the actual and the virtual sources are superimposed as full–filled blue, red and black circles, respectively. The black asterisk, instead, is the estimated damage position computed in the localization phase. Moreover, the actual and virtual propagation paths are highlighted in continuous black and dotted blue lines, respectively. To reduce the computational cost of the entire procedure, DAS is exploited in the localization phase to estimate the damage position, while either DAS, DMAS or DS-DMAS beamforming methods were applied in the filtering phase. In Fig.5.20, results achieved by beamformers in conjunction with FZF at the excitation frequency of 200 kHz are shown.

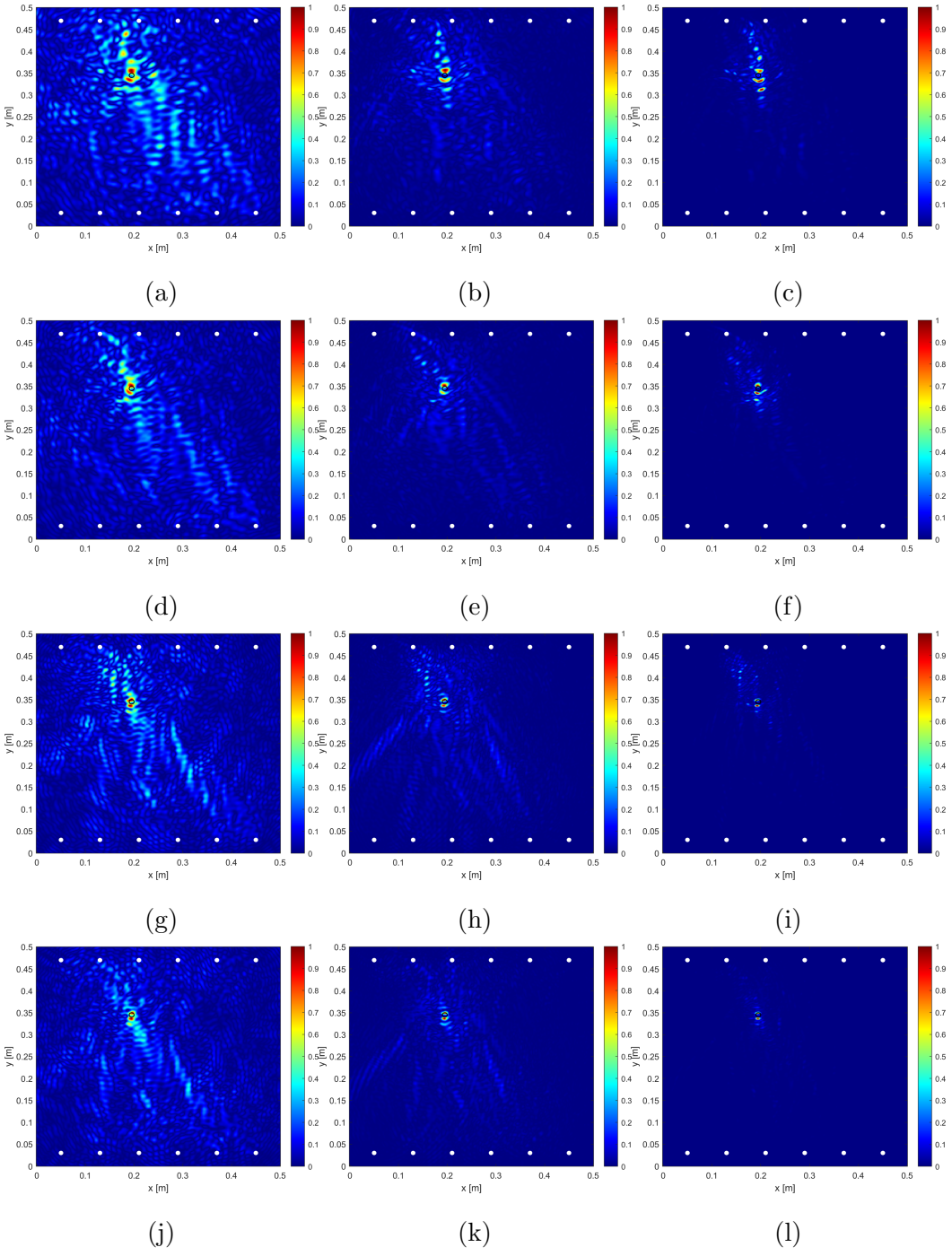

Figure 5.22: Imaging outputs at different excitation frequencies. DAS, DMAS and DS–DMAS are plotted in the first, second and third column from left to right, respectively. Beamforming output from datasets at excitation frequencies of 160 kHz (a,b,c), 180 kHz (d,e,f), 220 kHz (g,h,i) and 240 kHz (j,k,l) are plotted.

For a clear comparison, the first and second rows of the figure include DAS, DMAS and DS-DMAS outputs (from left to right) without and with FZF for the same damage position, respectively. The images with the FZF show a reduction of both noise and artefacts, thus highlighting the damaged region of the plate, as expected. In the third and fourth row of Fig.5.20, instead, the beamforming images computed with FZF at 200 kHz for two different damage positions are depicted. Also in these cases, the FZF method enhances the beamforming algorithms performance, as it can be observed by comparing Fig.5.20 with Fig.5.17, in which the beamforming outputs without FZF are shown for the same damage positions and excitation frequency. Similarly, DS-DMAS with FZF results at different damage positions are summed up in Fig.5.21. It is evident that the images feature well–defined sparkles close to the actual damage position. Moreover, almost the entire information refer to the damage influence, with no significant noise and artefacts. To complete the visual characterization, beamforming outputs at different excitation frequencies computed with FZF can be observed in Fig.5.22. Frequencies from 160 kHz to 180 kHz with a frequency step of 20 kHz are considered at each row, from top to bottom. As usual, DAS, DMAS and DS-DMAS outputs are plotted in each column from left to right, respectively. By comparing Fig.5.22 and Fig.5.18, it is possible to clearly evaluate the improvements of the FZF methods. In particular, it's worthy to notice that the DS-DMAS output at 160 kHz was not able to locate the defect in Fig. 5.18c. Meanwhile, the damage location is perfectly identifiable if the FZF method is applied, as Fig.5.22c demonstrates.

Nevertheless, it's worthy to notice that FZF is sensitive to the precision of the damage location estimated during the first phase. Thus, a robust localization leads to high performative FZF. Conversely, high error in the localization estimation may focus the beams in the wrong plate area leading to poor results.

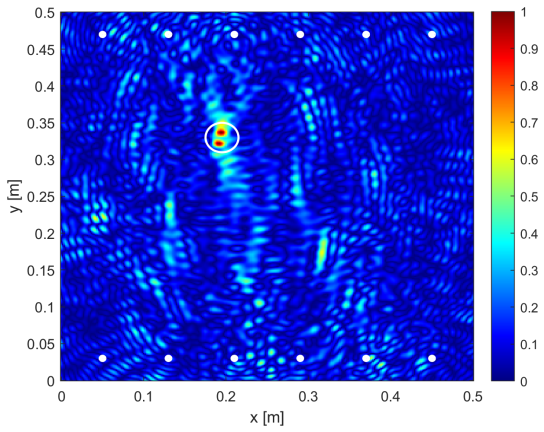

Figure 5.23: DAS output in which ROI is depicted as a white circle [AP5].

Results

Disclaimer: the following section was previously published in ©IEEE [AP5]. The beamforming algorithms have been characterized in order to quantitatively compare the imaging results. Three metrics were adopted for the analysis, *i.e.* the Contrast Ratio (CR), Peak Signal-to-Noise ratio (PSNR) and the generalized Contrast-to-Noise ratio (gCNR). CR is defined as follows:

$$CR = 20 * log_{10}(\frac{\mu_i}{\mu_o}) \tag{5.38}$$

where μ_i and μ_o are are the average pixel intensity inside and outside a defined Region of Interest (RoI), respectively. In particular, RoI was defined as the circular region centered in the actual damage position with a radius of 20 mm. In this work, we have considered a RoI bigger w.r.t. the actual damage area dimensions to take into account the finite spatial resolution imposed by the narrowband actuation in the heat map, and to ensure a representative measurement of the figures of merit. In Fig.5.23, the RoI is depicted as a white circle which surrounds the damaged area.

The PSNR, instead, is the ratio between the signal peak and the power

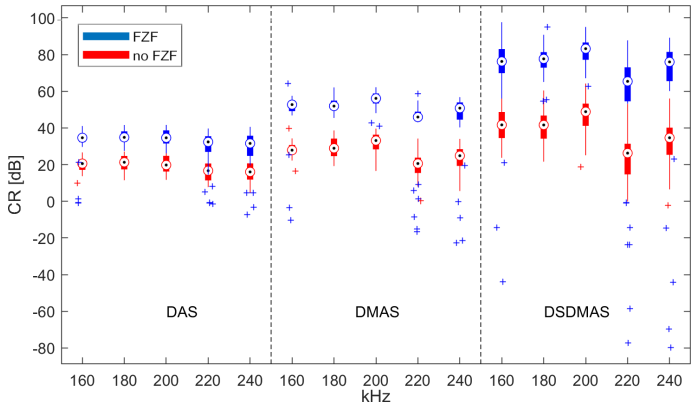

(a)

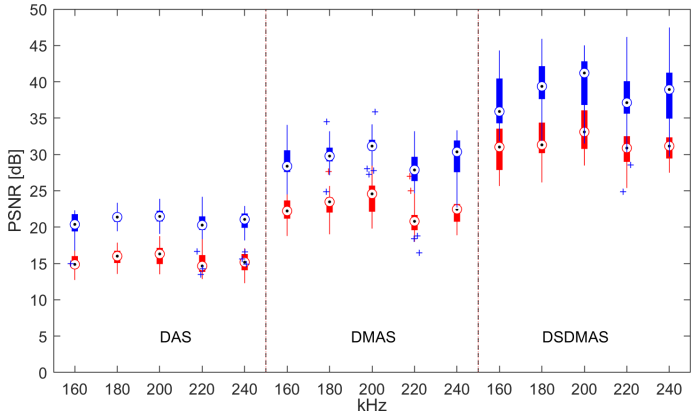

(b)

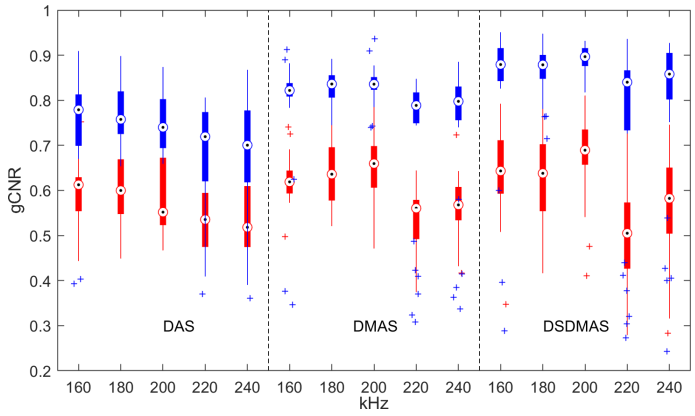

(c)

Figure 5.24: Metrics used to characterize the imaging outputs: (a,b,c) CR, PSNR and gCNR boxplots, respectively. Blue and red boxes refer to the beamforming with and without the FZF, respectively. Each plot is divided into three sections: DAS, DMAS and DS–DMAS, respectively. In each section, metrics are depicted in relation to specific datasets at different excitation frequencies, from 160 kHz to 240 kHz [AP5].

noise signal P_{Noise}:

$$PSNR = 10 * log_{10}(\frac{Peak^2}{P_{Noise}}) \tag{5.39}$$

Assuming that noise affects the imaging output outside the RoI, P_{Noise} can be computed as [296]:

$$P_{Noise} = \frac{1}{M}\sum_{i=1}^{M}\left|{x_i}^2\right| \tag{5.40}$$

where x_i is the $i-th$ pixel value out of M pixels located outside the RoI.

Finally, gCNR is a metric recently introduced by Rodriguez–Molares et al. [297, 298] and used in photoacoustic imaging [290] and medical ultrasound imaging [299]. gCNR is supposed to overcome limits of conventional Contrast-to-Noise Ratio (CNR) [300] in quantifying the damage detectability. In non–linear imaging algorithms characterized by high contrast or high dynamic range, conventional CNR decreases because of the sharper speckle pattern due to the variance rise [301]. gCNR, instead, is more robust to dynamic range alterations and less influenced by speckle noise. The histogram-based expression for the gCNR is [302]:

$$gCNR = 1 - \sum_{k=0}^{B-1} min\{h_i(l_k), h_o(l_k)\} \tag{5.41}$$

where h_i and h_o are the histograms related to the intensity of the pixels inside and outside the RoI, respectively. They both feature the same number of bins B centered at intensity levels $[l_1, l_2, l_3, ..., l_{B-1}]$. In particular, in this work, 512 bins were used to compute the metric.

gCNR aim is to measure the capability to distinguish if a certain image pixel represents damage from an ideal observer perspective [297]. $gCNR = 0$ means that the beamforming imaging output does not give any information about the plate conditions, while $gCNR = 1$ leads to perfect pixel classification.

In Fig.5.24 metrics are shown by means of boxplots, which are a compact statistical visualization of the data. In particular, each dataset at a specific fre-

quency is represented by a box in which the central mark is the median, while the bottom and top edges of the box represent the 25^{th} and 75^{th} percentiles, respectively. Outliers, instead, are plotted as cross marker symbols. To sum up, in TABLE 5.2, instead, the median values computed on all the datasets from 160 kHz to 240 kHz for all the different beamforming techniques are shown. For a compact notation, the metrics median values will be addressed as $\overline{CR}$, $\overline{PSNR}$ and $\overline{gCNR}$. As a general definition, CR points out the contrast level of the imaging outputs. By looking at Fig. 5.24a, DS-DMAS features higher CR valuers w.r.t. DAS and DMAS independently to the use of the FZF. Similarly, DMAS CR is higher than DAS. If we analyse the FZF impact, the $\overline{CR}$ improvement w.r.t. the corresponding algorithm without the use of the FZF can be estimated with an increase of 75 %, 86.2 % and 83.2 % for DAS, DMAS and DS-DMAS, respectively. Similarly, PSNR boxplot shows a clear rise of the metric between DAS, DMAS and DS-DMAS. PSNR is strictly related to artefacts and noise level of the imaging outputs. The higher the PSNR, the lower is the noise outside the RoI. As expected, DMAS outperforms DAS, while DS-DMAS features a better performance of both DAS and DMAS. Moreover, FZF procedure is able to further enhance the image quality in all the different methods. In TABLE 5.2, the $\overline{PSNR}$ values demonstrate the effectiveness of the proposed methodology. In fact, in the case of FZF the $\overline{PSNR}$ values increase from 21.07 dB to 29.78 dB till 38.94 dB, for DAS, DMAS and DS-DMAS respectively. By considering the imaging improvement carried on by the FZF, instead, the enhancement in the $\overline{PSNR}$ value is 34.5 %, 32.6 % and 25 % for the DAS, DMAS and DS-DMAS, respectively. Finally, gCNR can be associated with the probability of damage detection in ultrasound images. Thus, gCNR is intended to determine if the damage is actually detectable from an ideal observer. In Fig.5.24c the gCNR boxplot is depicted. All the beamforming

	FZF Y/N	DAS	DMAS	DS-DMAS
$\overline{CR}$	Y	34.62	51.92	76.27
	N	19.78	27.88	41.62
$\overline{PSNR}$	Y	21.07	29.78	38.94
	N	15.18	22.46	31.16
$\overline{gCNR}$	Y	0.74	0.82	0.88
	N	0.55	0.62	0.64

Table 5.2: CR, PSNR and gCNR median values for all the imaging outputs analysed with and without FZF. The median is performed using all the datasets from 160 kHz to 240 kHz [AP5].

algorithms with the FZF have $\overline{gCNR} > 0.7$ with maximum of $\overline{gCNR} = 0.88$ for the DS-DMAS. The results demonstrate the overall good performance of the FZF which is able to significantly enhance the damage recognition. In fact, by considering the imaging without the FZF, $\overline{gCNR}$ ranges between 0.55 and 0.64, which is a quite poor result. The improvement of the $gCNR$ metric between the beamforming output with and without the FZF is about 34.5 %, 32.2 % and 37.5 % for DAS, DMAS and DS-DMAS, respectively. Moreover, gCNR confirms the general trend which has been highlighted by other metrics. In particular, the results show that DS-DMAS generates a better image than DMAS, which, similarly, outperforms DAS.

Future works will investigate the behaviour of this approach in a more complex SHM scenario, such as the open dataset described in Marzani et al. [303], which provides GWs propagating on a composite panel of a full–scale aeronautical structure in non controlled environmental conditions. In this case, temperature and humidity variations, the complexity of multimodal propa-

gation and different operation conditions will be challenging tasks to address in order to extend the capabilities and robustness of the proposed method. Moreover, velocity compensation techniques will be investigated to improve the localization precision by exploiting accurate velocity models. In particular, since FEM and SAFE models are usually not accurate in non–homogeneous structures such as in real case scenarios where the structural properties are partially, or not known, a precise experimental estimation of the velocity model is fundamental to achieve good beamforming results. Even if the literature offers many research studies about the experimental extraction of dispersion curves, the proposed techniques are usually limited by investigating the structure along a single direction, which is not sufficient in anisotropic contexts. Very few examples of direct methods for the extraction of the velocity along all the propagation directions at a given frequency exist. This consideration is the basis of the work introduced in the next chapter, where novel wavefield analysis tools for the extraction of the dispersion curves in polar coordinates will be provided.

Chapter 6

Dispersion curves characterization

Disclaimer: the following section was previously published by ©2021 IEEE [AP10].

Due to the complex behaviour of Lamb waves propagation, the experimental characterization of Lamb waves dispersion curves in plate–like structures is fundamental for a precise and reliable SHM/NDT inspection. Anyway, even if many different techniques exist for the dispersion curves extraction in a single propagation direction when an anisotropic material has to be characterized, a multi–direction analysis must be carried on. This can be done by repeatedly extracting the dispersion curves along multiple directions [304–306] which is extremely expensive from a computational point of view. Unfortunately, very few examples in literature with the aim of a complete and efficient Lamb waves analysis along with multiple directions of propagation simultaneously are present.

In this chapter, two techniques for the extraction of the wavenumber profile from Scanner Laser Doppler Vibrometer (SLDV) measurements are intro-

duced. The first approach is based on an image segmentation algorithm called Distance Regularized Level Set method which is extensively exploited in image processing and computer vision. The second, instead, relies on a compressive sensing technique addressed as 2D sparse wavenumber analysis. Once the wavenumber profile is obtained, the velocity dispersion curves are computed accordingly by numerical methods. The proposed approaches have been tested on three different CFRP with different degrees of non-isotropy properties. The results show the effectiveness of the two methods, highlighting the advantages and disadvantages of both.

6.1 Introduction

The complex behaviour of Lamb waves which propagates through the material is not trivial to be precisely predicted. Thus, waves propagation is usually modelled by Finite Element Method (FEM) [307] or SAFE [134, 308] formulations, such as boundary elements [309, 310], spectral elements [311], transfer matrix methods [312] and global matrix methods [313]. Although these methods are fundamental for a first characterization, a complete and precise analysis can not be achieved due to:

- models approximations;
- material non idealities;
- material non-homogeneity
- uncertainties or deviations of material parameters;
- material parameters unknown.

Thus, experimental characterization, *i.e.* extraction of the dispersion curves, of the structure under investigation is fundamental to support and integrate the preliminary analysis carried on with modelling tools. Different approaches exist for this task, such as different technologies. One of the most exploited is wavefield imaging, in which ultrasonic guided waves which propagate through a specific area are acquired and mapped in a spatial 2D coordinate system. As a result, a series of images showing the waves propagation at different instants is obtained. The wavefield can be generated and acquired by various types of technologies. Usually, a source at a fixed position is exploited to generate the mechanical waves, while a scanning receiver acquires data. For instance, SLDV or Air coupled probes can be used to collect the wavefield on a spatial sampling grid and generate images. In particular, SLDV can measure the displacement of the test object by a laser beam and records the data across a large number of grid points within a short time. To focus the beam, SLDV can exploit either the mechanical motion of the laser head or high precision controlled mechanical mirrors [314]. As a drawback, automatic measurements might take several hours to be completed, since usually measurements are repeated multiple times for each scan point and then averaged to enhance signal–to–noise ratio. Depending on the SLDV technology, different information can be extracted from the measurement. For instance, 1–D SLDV can measure only the out of plane wave component, if a plate–like structure is placed normal to the laser beam. Thus, this SLDV technology is suitable for investigating A0 mode propagation. On the other hand, 3–D SLDV provides 3-D wave components along X, Y and Z components, respectively, which enables the complete characterization of complex multimodal propagation patterns. Swenson et al. [315] performed a comparison between 1–D and 3–D SLDVs wavefield measurements using lead zirconate titanate (PZT) transducers, highlighting differences between these

systems. In [156], instead, an exhaustive and complete description of Laser ultrasonics techniques and their applications are provided. In general, SLDV for full wavefield measurements have been used in many research works [316–320]. The most common approach is to generate the ultrasonic waves by exploiting PZT actuators while the SLDV acquires the displacements associated with the motion of the elastic waves in space and time domains. Once the full wavefield is acquired, several characterizations can be carried on. For instance, SLDV measurements enable solid damage detection and localization in NDT field. Sohn et al. [321] presented signal and image processing algorithms to automatically detect delamination and disbond in composite plates from wavefield images. Ruzzene et al. [322], introduced a full wavefield data technique able to perform damage detection, visualization and characterization in the wavenumber/frequency domain. Mesnil et al. [323], instead, presented an exhaustive comparison between two imaging methods, *i.e.* instantaneous and local wavenumber damage quantification techniques.

SLDV measurements can also be exploited for characterizing the guided waves dispersion curves. Malladi et al. [324] were able to experimentally extract the frequency response functions (FRFs) which were used to develop data–driven models, and then, dispersion curves. Ma and Yu [325], instead, extracted the A0 dispersion curves of an aluminium plate by exploiting 2D Fourier Transform from full wavefield data. In fact, Lamb waves dispersion curves are usually drawn out by exploiting the Fourier Transform in order to depict the waves in the frequency–wavenumber domain. Then, the extraction of the wavenumber characteristic can be performed by Matrix Pencil Method [271, 272] and ridge detection algorithms [326, 327]. Therefore, the velocity profiles, *i.e.* phase and group velocities can be computed accordingly. Depending on the experimental setup and instrumentation involved, different

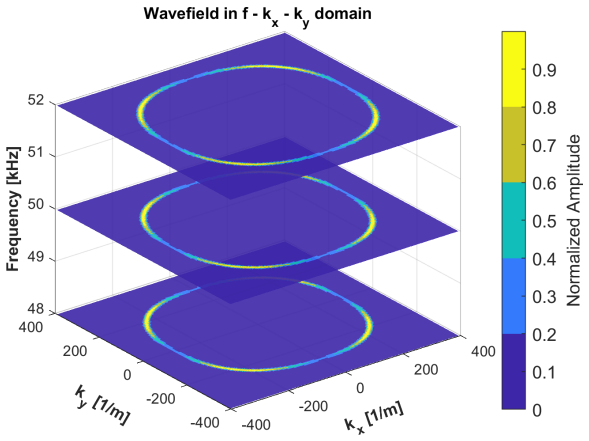

Figure 6.1: Wavefield representation in the 3D Fourier Domain [AP10].

types of analysis can be carried on. For instance, Harb and Yuan [208] used an air-coupled transducer and an LDV to compute the dispersion curves by means of Snell laws. Hernandez et al. [328], instead, extracted the dispersion curves by determining the phase difference and time lag between two pulses acquired by two transducers at different distances w.r.t. the active sensor. In the case of anisotropic materials, instead, the characterization of the waves propagation along with a single direction is no longer sufficient [304–306]. Moreover, conventional time–frequency based methods might be affected by complex geometries such as multi–path interference which can lead to artefacts and noise. To tackle these limitations, a multi–direction analysis in the wavenumber-frequency domain can be addressed, especially in the case of SLDV measurements. The main idea is to compute the Fourier Transform multiple times to transform the original SLDV measurements from $t - x - y$ into $f - k_x - k_y$ domain, where t is time, (x, y) are the spatial directions, f is frequency and $(k_x k_x)$ are the wavenumbers. In particular, a 3D Fourier Transform, or 3D-DFT is required. In the case of wavefield analysis, the 3D-DFT

can be defined as follows:

$$U(\omega, k_x, k_y) = \sum_{t=1}^{N} \sum_{x=1}^{M_x} \sum_{y=1}^{M_y} u(t, x, y) e^{-j(\omega t + k_x x + k_y y)} \tag{6.1}$$

where N and (M_x, M_y) are the number of temporal and spatial samples acquired, respectively. The wavefield in the transformation domain can be viewed as in Fig.6.1, where each slice at a fixed frequency is addressed as k-space or 2D wavenumber domain.

Thus, the wavenumber profile of the most energetic propagation mode is clearly revealed along with all the different propagation directions [329]. Moreover, the results show the possibility to perform many signal processing techniques, such as mode separation [322], wavenumber filtering [330] and wavefield manipulation [321]. Multiscale representations such as those generated by multidimensional Wavelet [331] or Curvelet transforms [332] allow to better track non-stationary effects. Nevertheless, the extraction of the wavenumber profile for a defined f_i is not trivial, due to the closed–loop shape which inhibits the exploitation of conventional ridge detection algorithms [333]. In general, very few research studies addresses this aspect. Ma and Yu [334], for instance, exploited a maximum–tracking based technique, in which, after the conversion from the Cartesian $U(f_i, \mathbf{k})$ to the polar $U(f_i, r, \theta)$ plane, for each angle θ the radius at the maximum wavenumber index value was extracted. Anyway, this technique is highly sensitive to noise. An interesting perspective among full wavefield signal processing techniques is provided by Sabeti et al. [335, 336]. Due to the sparse wavefield representation in the k-space, they exploited compressive sensing techniques for reconstructing the time-space wavefield from sub-sampled SLDV acquisitions. Since the wavefield reconstruction is based on the dispersion curves computation, the method implicitly estimates the wavenumber curves. In the case of anisotropic plates, the Anisotropic Sparse

Wavefield Analysis (ASWA) and the 2DSWA can be exploited. The former features very high levels of compression, although it is not suitable for characterizing scatters and edge reflections, such as multimodal propagation. The latter, instead, even if features lower compression rates, is able to properly handle reflections and multi-mode propagation.

6.2 The Distance Regularized Level Set Evolution

Disclaimer: the following section was previously published by ©2021 IEEE [AP10].

Level Set algorithms for image processing can determine contours of highly–complex images without any parametrization [337]. By defining a Level Set Function (LSF) $\phi : \Omega \rightarrow \Re$ as a three dimensional curve in the xyz-surface, the zero level set can be expresses as $\phi(x, y) = c$, where $\phi(x, y) = c$. Thus, the zero level set can be thought of as a horizontal slice of the graph at height $z = c$ in which a closed–loop shape divides two distinct regions. Starting from the zero level set, the evolution of the level set, *i.e.* the evolution of the closed–loop shape, can be synthesised following a curve evolution expression:

$$\frac{\partial \phi}{\partial t} = F|\nabla \phi| \tag{6.2}$$

where F is the speed function that controls the contour motion. Unfortunately, this formulation is affected by irregularities of the LSF which rise during the evolution process. Distance Regularized Level Set Evolution (DRLSE) formulation, instead, by exploiting a distance regularization term and an external energy term, can achieve better performance overcoming conventional LS algorithms limits. Thus, the level set evolution is derived as a gradient flow that

minimizes an energy functional $\mathcal{E}(\phi)$:

$$\mathcal{E}(\phi) = \mu\mathcal{R}_p(\phi) + \lambda\mathcal{L}_g(\phi) + \alpha\mathcal{A}_g(\phi) \tag{6.3}$$

where $\mathcal{R}_p(\phi)$ is the level set regularization term, $\mathcal{L}_g(\phi)$ and $\mathcal{A}_g(\phi)$ are energy functionals, $\mu > 0$, $\lambda > 0$ and $\alpha \in \Re$ are constant coefficients for $\mathcal{R}_p(\phi)$, $\mathcal{L}_g(\phi)$ and $\mathcal{A}_g(\phi)$ respectively. In particular:

$$\mathcal{R}_p(\phi) = \int_\Omega p(|\nabla\phi|)\, dx \tag{6.4}$$

where $p : [0\,\mathrm{inf}) \rightarrow \Re$ is the potential function which features two minimum points (double well points) $p(|\nabla\phi|) = 1$, in the proximity of the zero level set, and $p(|\nabla\phi|) = 0$, otherwise. As a consequence, a strong smoothing effect and an accurate computation during the level set evolution is ensured. $\mathcal{L}_g(\phi)$, instead, reaches its minimum value when the zero level contour of ϕ and the actual image contour overlap. It is defined as:

$$\mathcal{L}_g(\phi) = \int_\Omega g\delta(\phi)|\nabla\phi|\, dx \tag{6.5}$$

where g is an edge indicator function whose value is smaller at the target image boundary and δ is the Dirac function. Finally, $\mathcal{A}_g(\phi)$ is the energy functional introduced for speeding up the convergence:

$$\mathcal{A}_g(\phi) = \int_\Omega gH(-\phi)\, dx \tag{6.6}$$

where H is the Heaviside function. Then, the minimum of Eq.(6.3) can be obtained by resolving the gradient flow equation [338] defined as:

$$\frac{\partial\phi}{\partial t} = -\frac{\partial\mathcal{E}(\phi)}{\partial\phi} \tag{6.7}$$

where $\frac{\partial\mathcal{E}(\phi)}{\partial\phi}$ is the Gâteaux derivative of the functional $\mathcal{E}$, which can be developed as:

$$\frac{\partial\phi}{\partial t} = \mu div(d_p(|\nabla\phi|)\nabla\phi) + \lambda\delta(\phi)div(g\frac{\nabla\phi}{|\nabla\phi|}) + \alpha g\delta(\phi) \tag{6.8}$$

given an initial $\phi(x,0) = \phi_0(x)$ and d_p is a function defined as:

$$d_p(s) = \frac{p'(s)}{s} \tag{6.9}$$

In practical terms, Eq.(6.8) is an edge-based geometric active contour model, in which, once the steady–state is found, the contour of the figure is extracted (for a more in–deep mathematical presentation, see [337]).

6.3 2DSWA based method

Disclaimer: the following section was previously published by ©2021 IEEE [AP10].

Although SLDV is capable to perform high precision measurements in SHM field, the data acquisition process is highly time–consuming as well. To tackle this limitation, many research papers address signal processing techniques to make the process faster, such as continuous-wave excitations [339, 340], multi-point laser vibrometry [341] and global-local sensing [342]. Recently, Compressive Sensing (CS) techniques have been rising as the most promising methodology to make SLDV measurements faster. To effectively perform CS, a few requirements are needed. At first, the acquired signals must feature sparsity, *i.e.* with only a few nonzero coefficients in a transformation domain in order to be fit by a linear superposition of a few atoms of an appropriate basis. Then, the samples must be incoherent, *i.e.* the elements of the sparsifying basis are not or poorly correlated with the acquired samples. If the requirements are satisfied, CS techniques permit to sub–sample signals below the Nyquist sampling rate without losing information [343, 344]. Thus, by exploiting the sparse signal representation in the Fourier domain, it has been demonstrated that CS is able to accurately reconstruct the full wavefield on a dense regular grid from a reduced number of actual measured signals acquired randomly.

Di Ianni et al. [159] investigated the most suitable CS bases to recover the full wavefield on both aluminium and composite plates. The experimental results validated the CS effectiveness with a reduction of the measurements points to less than 34 %. Esfandabadi et al. [344], instead, presented a damage detection and localization method in conjunction with CS. In such a way, a complete damage characterization has been carried on achieving high performance by removing up to 80 % of the Nyquist sampling grid. The same authors in [345, 346], combined CS with Super-Resolution Convolutional Neural Network (SRCNN) schemes to achieve high-resolution images from low-resolution wavefield images. Finally, Sabeti et al. [335] presented a comparative study on compressing sensing techniques for full wavefield reconstruction addressed as Sparse Wavefield Synthesis. In particular, the comparison was carried on among ASWA [163], 2DSWA [347], and Fourier reconstruction. As a result, they found that:

- Fourier reconstruction is a valid and reliable tool if the spatial Nyquist sampling rate is affordable.
- 2DSWA can accurately reconstruct wavefields with low compression rate. The bright side is that the 2DSWA model is flexible and do not require any assumptions on the location of the wave source, single-mode propagation, material isotropy and material shape or geometry, *i.e.* reflection properties.
- ASWA is highly performative and can achieve high compression rates. Nevertheless, ASWA model can not handle reflections, inhomogeneities, multi-mode propagation. Moreover, ASWA requires *a-priori* knowledge of the source location.

In this work, 2DSWA was exploited to extract the wavenumber profile from

sub-sampled wavefield measurements. In fact, the sparse wavefield reconstruction by means of 2DSWA described in [347] is based on the extraction of the dispersion curves in the frequency wavenumber domain.

At first, let's define random sub–sampled wavefield measurements $y \in R^m$:

$$\mathbf{y} = \Phi\mathbf{x} \tag{6.10}$$

where $\Phi \in R^{m\times n}$ represents the measurement matrix and $x \in R^n$ is the wavefield without sub–sampling. Since, $\mathbf{x}$ has a sparse representation in some model basis $\Psi \in R^{n\times n}$, (6.10) can be reorganized as follows:

$$\mathbf{y} = \Phi\Psi\mathbf{s} = \Theta\mathbf{s} \tag{6.11}$$

where $\mathbf{s}$ is the sparse representation of $\mathbf{x}$ in the *f-k* domain, and Θ is called *dictionary* [335]. It's worthy to notice that $\mathbf{s}$ contains the dispersion curves information if the frequency-wavenumber domain is exploited as transformation domain. To determine the most suitable dictionary, the analytical Lamb waves model is considered. As a starting point, let's consider the ideal Lamb wave propagation model in the frequency domain for isotropic plate expressed by [161]:

$$\mathbf{y}(\mathbf{r},\omega) = \sum \sqrt{\frac{1}{k_n(\omega)r}} G_n(\omega) e^{-jk_n(\omega)r} \tag{6.12}$$

where r is the actuator–receiver points distance, ω is the angular frequency, $k_n(\omega)$ the n–th mode wavenumber dispersion curve and $G_n(\omega)$ is the complex wavenumber amplitude. Equation 6.12 can be viewed as a linear combination of a set of bases that constitute the wavefield. Thus, the dictionary Θ can be defined accordingly:

$$\Theta = \sqrt{\frac{1}{k_n r_m}} e^{-jk_n r_m} \tag{6.13}$$

To solve the undetermined system of equations (6.11) a sparse recovery algorithm, such as the Orthogonal Matching Pursuit (OMP) technique [348] can

be used. In such a way, the wavenumber profile can be extracted in the transformation domain. Nevertheless, the Lamb waves model in Equation (6.12) is only valid in the frequency-wavenumber domain for isotropic plates. To extend the approach to anisotropic materials, the following considerations have to be carried on. In Fig.6.1, the wavefield in the 3D Fourier domain is depicted. It clearly shows its sparse nature where almost the entire representation is characterized by zero or *quasi* zero values. Thus, the 3D Fourier domain can be exploited as a transformation domain for the CS procedure. Since the computation of a 3D CS which starts from the time-space domain and lands in the 3D Fourier domain is not trivial, the procedure can be simplified by starting from the frequency-space domain. In such a way, a 2D transformation is required to correctly land in the k-space. Accordingly, Eq.(6.11) can be rearranged as follows:

$$\mathbf{Y_i} = \Theta_1 \mathbf{S_i} \Theta_2^T \tag{6.14}$$

where $\mathbf{Y_i} \in M_y \times N_x$ is the frequency-domain wavefield (f_i, x, y) and $\mathbf{S_i} \in M_y \times M_x$ is the 2–D sparse representation of the wavefield in the $f_i - k_x - k_y$ domain. $\Theta_1 \in M_y \times N_y$ and $\Theta_2 \in M_x \times N_x$, instead, are the left and right dictionaries, which can be defined as spatial Fourier bases that are synthesized with respect to Cartesian coordinates of the grid points and the wavenumber range in each direction:

$$\Theta_1 = e^{-jyk_y^T} \tag{6.15}$$

$$\Theta_2 = e^{-jxk_x^T} \tag{6.16}$$

This approach is addressed as 2DSWA and can be exploited to deal with non–isotropic Lamb waves propagation. Since the wavenumber information resides in $\mathbf{S_i}$, the wavenumber extraction is possible by solving (6.14). In this case, the solution of the undetermined system of equations can be computed by a modi-

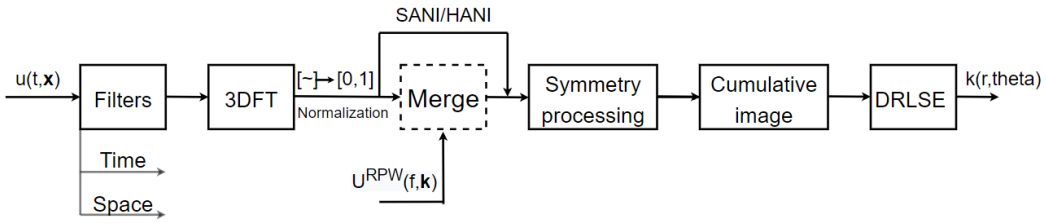

Figure 6.2: DRLSE–based signal processing. $U^{RPW}(f, \mathbf{k})$ is the OGW Reflected Paths Wavefield in the Fourier domain [AP10].

fied 2D version of the OMP algorithm which was presented in [349]. As a result, a point cloud for each frequency of interest is extracted in the 2D wavenumber plane. Thus, the wavenumber polar representation at given frequencies can be extracted enabling the analysis of direction-dependent velocity variations in anisotropic structures [335]. For a more exhaustive perspective of 2DSWA mathematical aspects and performance description in the case of Sparse Wavefield Analysis of both isotropic and anisotropic plates, refer to [347].

Finally, it's worthy to mention that this technique is very effective for low undersampling rates, *i.e.* close to the Nyquist rate. On the bright side, borders and scatter reflections such as multimodal propagation are well characterized.

6.4 Materials and Methods

Disclaimer: the following section was previously published by ©2021 IEEE [AP10].

DRLSE -based approach and 2DSWA for dispersion curves extraction have been tested on SLDV measurements. In particular, three datasets on three different CFRP were exploited. The plates feature different anisotropic properties and different acquisition strategies, for a complete and reliable algorithms validation. The first plate, which is characterized by slightly anisotropic prop-

agation, is described in [155] and addressed in this work as SANI dataset. The second plate, instead, is described in [350]. It features a unidirectional highly anisotropic characteristic. For such a reason it will be addressed as HANI dataset. The last dataset is related to a plate made of quasi–isotropic laminates and it is freely available on the online Open Guided Waves (OGW) website (`http://www.open-guided-waves.de` [145]). For this reason, it will be addressed as OGW dataset.

6.4.1 Experimental setups

Disclaimer: the following section was previously published by ©2021 IEEE [AP10].

The SANI wavefield was acquired on a carbon/epoxy 16-layers laminate made of prepregs GG 205 P (fibres Toray FT 300-3K 200 tex) by G. Angeloni and epoxy resin IMP503Z-HT by Impregnatex Compositi. The specimen dimensions are 1200x1200 mm with average thickness 3.9 mm, weight of 8550 g and density 1522.4 $^{kg}/_{m^3}$. The HANI plate, instead, features 40 layers made of unidirectional carbon/epoxy fibers stacked in one direction (90 degrees). In this case, the plate dimensions are 1200x1200 mm for 2.85 mm of average thickness, weight of 6460 g and density of about 1574 $^{kg}/_{m^3}$. In both cases, a piezoelectric PZT disk of 10 mm diameter was attached at the centre of the CFRP plates and used as actuator. The excitation signal was a narrowband signal centred at 50 kHz. Due to the symmetric characteristic of the plates which yield the same propagation properties in all the four quadrants, only one–quarter of the plate was scanned with the SLDV (Polytec PSV–400) to reduce data acquisition time. In the previous works of Kudela et al. [155] and [350], the SANI and HANI plates were characterized by broadband measurements to extract experimentally the elastic constants of the composites starting from the

C	SANI	HANI
C_{11}	52.55	138.67
C_{12}	6.51	5.72
C_{13}	5.94	6.53
C_{22}	51.83	12.36
C_{23}	5.88	5.99
C_{33}	10.28	11.80
C_{44}	2.93	3.12
C_{55}	2.92	5.11
C_{66}	3.81	4.89

Table 6.1: The optimized elastic constants of the SANI [155] and HANI [350] plates [GPa] [AP10].

measured dispersion curves. Then, by using a genetic algorithm, the best fit between theoretical and experimental curves was extracted. The so obtained elastic constants have been used for reliable and accurate SAFE simulations in order to permit a solid characterization of the results. The elastic constants are shown in TABLE 6.1.

Finally, the last dataset was acquired on a plate made of prepreg material Hexply M21/T700, with dimensions 500x500 mm and 2 mm of thickness. The laminates layup is $[45/0/-45/90/-45/0/45/90]_S$, giving to the laminate quasi–isotropic properties. In this case, a 5 mm diameter PZT sensor was attached at the centre of the plate and used to actuate a narrowband signal centred at 60 kHz. It's worthy to notice that at the plate at 60 kHz shows an anisotropic behaviour with A0 mode propagation which is predominant [145]. The wavefield was acquired by a NDT (Polytec PSV-400) on one–quarter of the plate, with the PZT transducer in the upper right corner. To reduce the

environmental effects, measurements were performed in a climate chamber at 23 °C of temperature and averaged 100 times for reducing noise. In the OGW plate the waves propagation follows central symmetry:

$$u(r, \alpha) = u(r, \alpha + \pi) \tag{6.17}$$

where $u(r, \alpha)$ is the wavefield in time and space domain but in polar coordinates. It's worthy to underline that the wavefield which propagates in only one–quarter of the laminate was acquired. Thus, the propagation characteristic along with 90° was scanned, which is not enough for a plate that features central symmetry, if only the wave direct path is considered. To perform a complete characterization along with 360°, information carried on by edges reflections was exploited. By exploiting a signal processing procedure that isolates the reflections from the plate edges, normalizes and enhances the reflections contribution, a high–resolution wavenumber profile is still achievable along with all the possible directions of propagation. In general, this technique can be applied on both narrowband or broadband measurements, without limitations regarding the central excitation frequency. Nevertheless, the SLDV intrinsic limits have to be considered. For instance, the Polytec PSV-400 shows a quite uniform sensitivity in the range up to about 300kHz. Moreover, at lower frequencies, only A0, S0 and SH0 propagation modes can be captured by the SLDV. Among them, the A0 mode is the most energetic since SLDV mostly measures particle velocities perpendicular to the surface of the specimen, which are dominant in A0 mode. For this reason, only the extraction of the antisymmetric mode A0 will be addressed.

Fourier–DRLSE approach

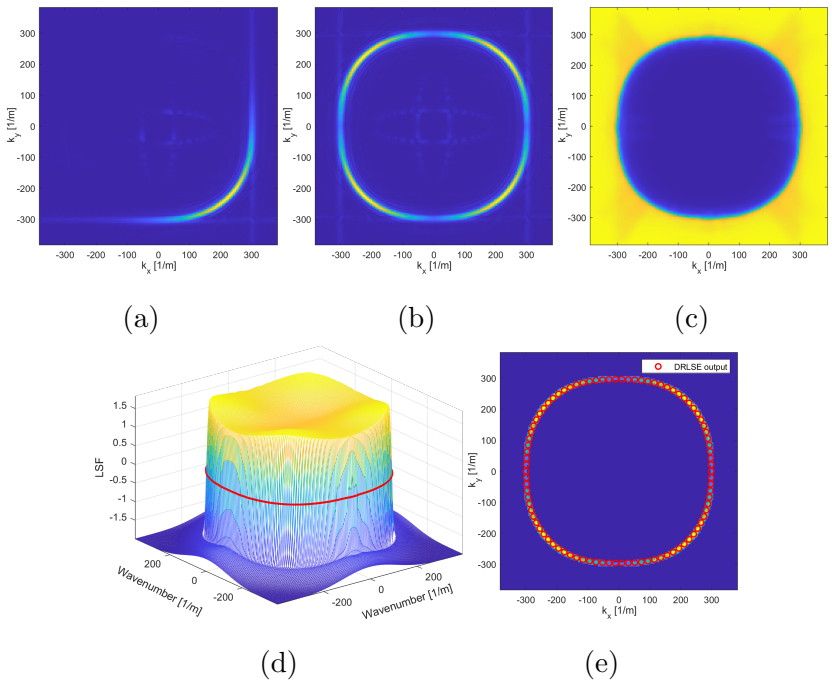

Figure 6.3: SANI wavenumber extraction: (a) SANI 3DFT output at 50 kHz. (b) SANI wavefield in the 2D wavenumber domain after the 'symmetry processing'. (c) SANI cumulative image. (d) LSF obtained after the evolution process. (e) SANI DRLSE output superimposed to the 2D wavenumber domain. (f) HANI DRLSE output [AP10].

In this section, the signal processing which has been developed for extracting the wavenumber characteristic in the k-space by exploiting the DRLSE algorithm is presented. Before applying the DRLSE method, some pre-processing steps have to be implemented to properly manipulate the wavefield in the k-space to let the DRLSE work optimally. The main steps of the Fourier–DRLSE processing are shown in Fig. 6.2. At first, a time window of 500 µs and 600 µs was exploited in the SANI /HANI and OGW cases, respectively, for cancelling noise and undesired plate edge reflections. Then, a spatial 2D

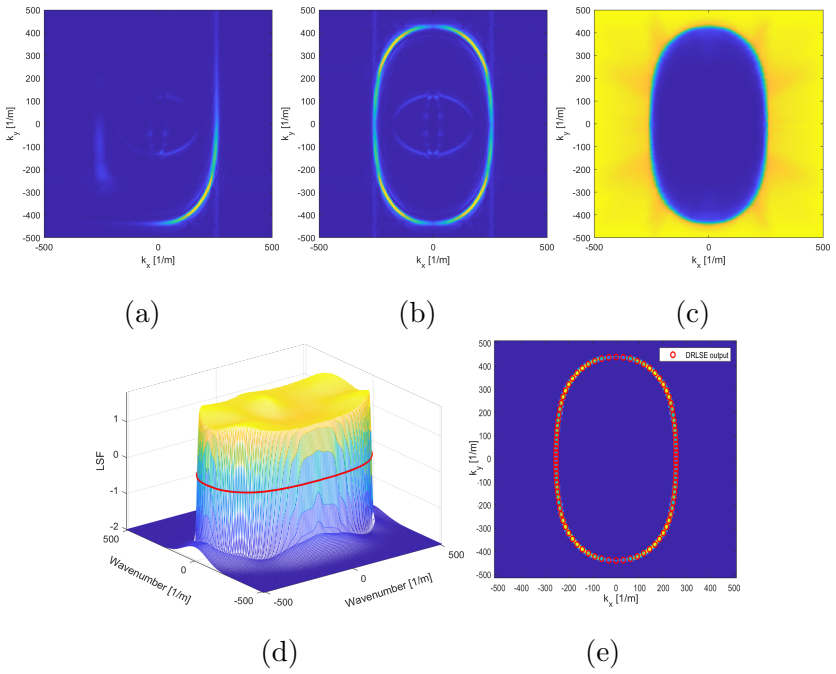

Figure 6.4: HANI wavenumber extraction: (a) HANI 3DFT output at 50 kHz. (b) HANI wavefield in the 2D wavenumber domain after the 'symmetry processing'. (c) HANI cumulative image. (d) LSF after the evolution process. (e) HANI DRLSE output [AP10].

Gaussian filtering is defined as:

$$G(x,y) = \frac{1}{2\pi\sigma^2} e^{-\frac{x^2+y^2}{2\sigma^2}}$$

with standard deviation $\sigma = 0.5$, has been applied to mitigate artefacts in the Fourier domain caused by plate borders. After the 3DFT computation, the Fourier coefficients are normalized in the interval [0,1]. For instance, in Fig. 6.3a, the SANI Wavefield in the 2D wavenumber domain at the fundamental frequency of 50 kHz is shown. The wavefield direct path is the main contribution in the fourth quadrant, which outlines the wavenumber at the excitation frequency. Due to the symmetry properties of the plate, the complete wavenumber characteristic can be synthesised by mirroring the partial

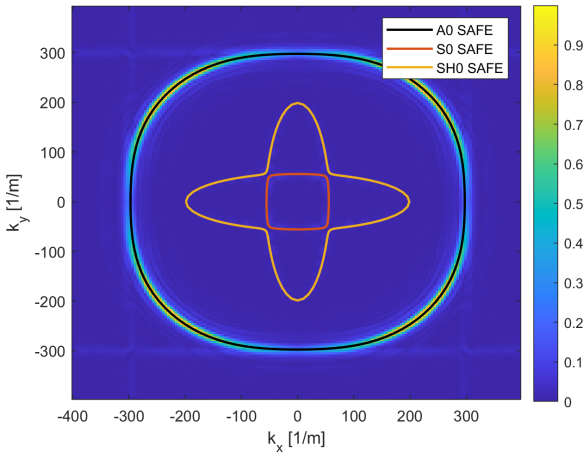

Figure 6.5: SANI wavefield in the 2D Wavenumber domain at 50 kHz. SAFE simulations of the A0, S0 and SH0 modes are superimposed [AP10].

profile revealed by the 3DFT. Similar results are achieved with HANI data. In Figs.6.3b and 6.4b, the SANI and HANI wavefields in the k-space after the described steps are shown. By close observation, the A0, S0 and SH0 modes profiles exist, even if the A0 mode features a higher intensity. For instance, in Fig.6.5, the theoretical dispersion curves are superimposed to the processed wavefield in the 2D wavenumber domain. Nevertheless, DRLSE can handle the contour detection of a single closed–loop shape, making it unable to process multiple modes at the same time. Thus, the S0 and SH0 modes are filtered out by a 2D wavenumber filter. In fact, A0 features a higher signal-to-noise ratio and signal resolution, making it suitable for a reliable algorithms evaluation. Anyway, the procedure can be theoretically carried on similarly to any propagation mode.

The OGW dataset, instead, is more complex and requires some additional steps. To clarify, in Fig. 6.6a, the OGW wavenumber profile in the k–space at 60 kHz is depicted.

The wavefield direct path shapes the wavenumber in just one–fourth quad-

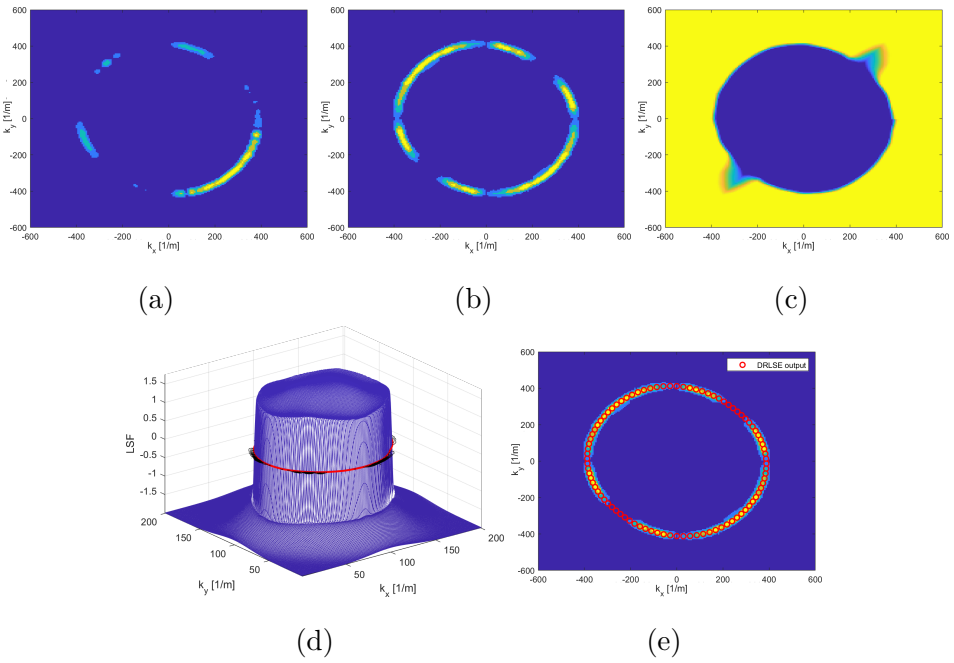

Figure 6.6: OGW wavenumber extraction: (a) 3DFT output at 60 kHz without any pre–processing. (b) $U(f_{60\,\mathrm{kHz}}, \mathbf{k})$ after the 'merge' processing block. (c) Cumulative image. (d) LSF after the evolution process. (e) DRLSE wavenumber output [AP10].

rant as in the previous case. Nevertheless, some information that is carried by edges reflections is barely visible in the other quadrants, even if the profile features with low signal-to-noise ratio and it is not visible in some propagation angles due to the strong signal attenuation. To extract much information as possible, two distinct time domain filters were applied to the raw wavefield to split information related to direct and reflected paths, respectively. In particular, the first interval which contains the wavefield direct path ranges from zero to 400 µs, meanwhile the second interval ranges from 200 µs to 600 µs. An overlap between the two time windows was used to reduce artefacts and maximize the wavefield energy. Afterwards, both the resulting filtered wavefields

were normalized in the [0 1] interval and merged again by selecting for each element of the two matrices the highest intensity value. Finally, the symmetry properties of the plate were exploited to generate a high–resolution image with all directions of propagation. In particular, by using 6.17, the picture depicted in Fig.6.6b has been synthesized. Since the DRLSE algorithm is essentially an edge detection algorithm, the wavefields so far processed have been manipulated in order to generate artificial edges. In particular, the cumulative function of $U(f_i, k_x, k_y)$ along with each propagation angle have been performed and then converted into a cartesian grid. To further enhance the picture edges, a contrast filter has been applied to help the DRLSE convergence. As a result, Figs. 6.3c, 6.4c and 6.6c show the synthesised *cumulative images* for the SANI, HANI and OGW cases, respectively. Afterwards, the DRLSE algorithm has been applied to the processed images. In particular, the resulting level set function which is obtained from the level set evolution is shown in Figs.6.3d, 6.4d and 6.6d. Then, the LSF contour is extracted and the wavenumber profile is drawn. Finally, In Figs. 6.3e and 6.4e the SANI and HANI final wavenumber reconstructions are shown superimposed to the corresponding wavefield Fourier transform, revealing an almost perfect overlap. Similar good results were achieved with the OGW (see Fig. 6.6e) and HANI datasets. In the OGW case, the DRLSE algorithm is able to reconstruct correctly the full wavenumber profile even in a complex scenario, where info is only partially known. In fact, the flexibility in the wavefield pre–processing, which can be customized easily with respect to the specific scenario, allows optimizing the DRLSE convergence even in datasets with low signal–to–noise ratios.

2DSWA based approach

Disclaimer: the following section was previously published by ©2021 IEEE [AP10].

The second approach for extracting the wavenumber profile in polar coordinates from full wavefield measurements is based on the 2DSWA. At first, specific pre–processing is exploited to reduce noise and reflections interference. In particular, a time windowing and a band pass filter have been applied to the wavefield. In particular, the selected frequency band ranges from 42 kHz to 58 kHz for the SANI and HANI datasets, while the spectral content from 50 kHz to 70 kHz have been used in the OGW case. After the pre–processing stage, compressive sensing is implemented. Let's define the sub–sampling ratio R_{UN} defined as follows:

$$R_{UN} = \frac{N_U}{N_{Nyq}} \tag{6.18}$$

where N_U is the number of points on the random sample grid and N_{Nyq} is the number of the points in the Nyquist grid [335]. A random sampling strategy with sub–sampling ratio $R_{UN} = 34.9\,\%$, $R_{UN} = 34.96\,\%$ and $R_{UN} = 83.3\,\%$ have been used for the SANI , HANI and OGW datasets, respectively. Then, the 2DSWA method is applied and the sparse representation of the wavefield is obtained. In Figs. 6.7a,6.7c and 6.7e, the point clouds which are given back by 2DSWA are depicted. Then, points related to the dataset excitation frequencies are selected. In Figs. 6.7b,6.7d and 6.7f, the selected points and their accordance with the corresponding wavefield Fourier transforms are shown for the SANI , HANI and OGW wavefields, respectively. It is evident that 2DSWA approach provides a good tracking of wavenumber profile, especially in the SANI and HANI cases. In the OGW dataset, instead, some propagation angles are not fully populated leading to a loss of information. Finally, due to the discrete nature of the 2DSWA output, a fitting procedure based on the

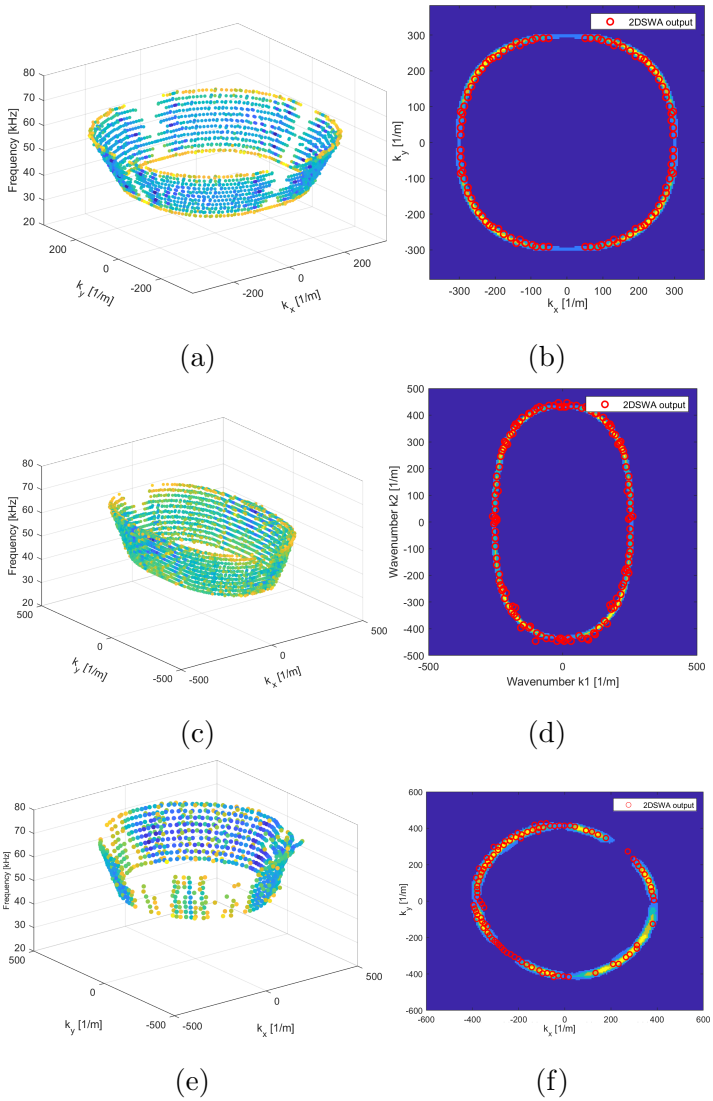

Figure 6.7: 2DSWA approach: (a,c,e) Points cloud obtained by 2DSWA output for the SANI, HANI and OGW datasets. Frequencies from 42 to 58 kHz for the SANI/HANI datasets, and from 50 to 70 kHz for the OGW dataset, are computed. (b,d,f) Points related to the dataset excitation frequency superimposed to the k–space for the SANI, HANI and OGW datasets, respectively [AP10].

Fourier series is used to find a good approximation of the wavenumber polar profile [351], after a mode filtering, if required.

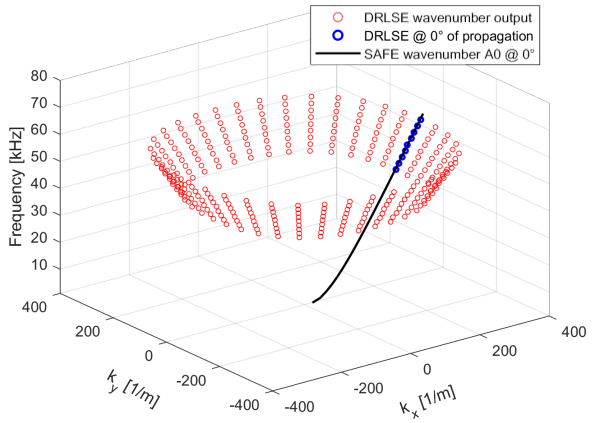

Figure 6.8: Single mode A0 wavenumber reconstruction for frequencies from 42 kHz to 58 kHz with a step of 2 kHz by DRLSE method. In black the theoretical A0 wavenumber along with 0° direction of propagation by SAFE simulation [AP10].

6.5 Results

6.5.1 Wavenumber extraction characterization

Disclaimer: the following section was previously published by ©2021 IEEE [AP10].

$R_{UN}[\%]$	Max$[m^{-}1]$	Average $[m^{-}1]$
83.3	4.72	2.79
41.66	5.47	3.15
31.26	6.63	2.37
23.45	76.46	32.17

Table 6.2: OGW wavenumber reconstruction errors by 2DSWA method varying R_{UN} [AP10].

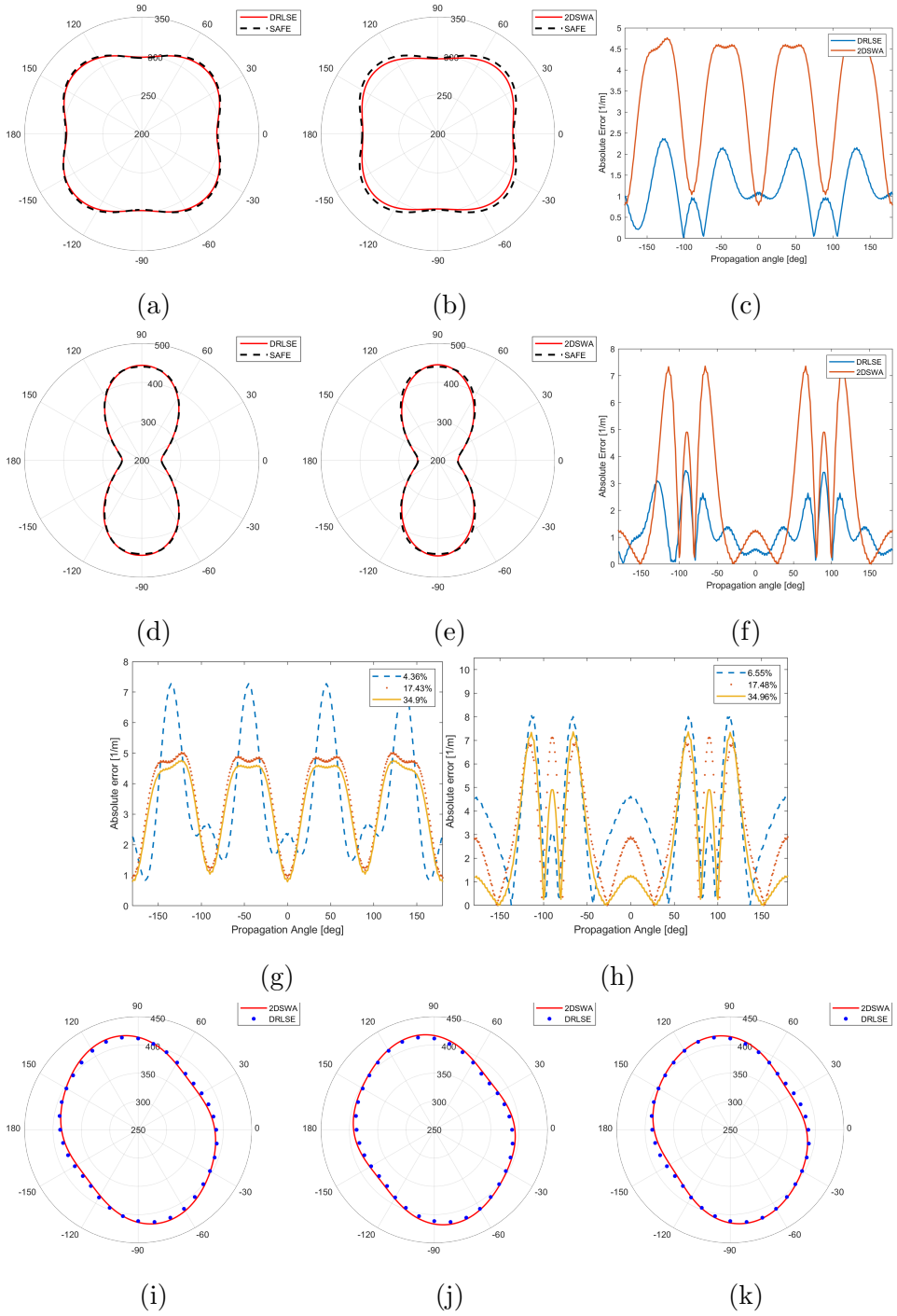

Figure 6.9: Wavenumbers extraction results ([m^{-1}]): (a,d) SANI,HANI DRLSE wavenumber reconstruction compared with SAFE simulation. (b,e) SANI,HANI 2DSWA wavenumber recontruction compared with SAFE simulation. (c,f) SANI,HANI error comparison between the two methods. (g,h) 2DSWA error analysis varying R_{UN} for the SANI,HANI datasets. (i,j,k) 2DSWA wavenumber reconstruction for the OGW dataset with $R_{UN} = 83.3\%, 41.66\%, 31.26\%$, respectively, compared with DRLSE output [AP10].

In this section, the extracted wavenumber profiles obtained by DRLSE and 2DSWA approaches are compared to SAFE simulations, which are supposed to be a reliable and accurate reference in the SANI and HANI cases. In Fig. 6.9a, 6.9b, 6.9d, and 6.9e, the DRLSE and 2DSWA outputs are depicted as a red continuous line, while SAFE simulations are drawn with a black dotted line. In both cases, the wavenumbers are extracted at the excitation frequency of 50 kHz. In Fig. 6.9c and 6.9f, instead, the DRLSE (in blue) and 2DSWA (in red) errors at each propagation angle are plotted. It's evident that the DRLSE results match extremely well the simulations. Meanwhile, 2DSWA features lower precision, even if the wavenumber reconstruction is still satisfactory if we consider that a sub–sampling of about $R_{UN} = 35\,\%$ was performed. In Fig. 6.9g, the error characterization of the SANI wavenumber at multiple compression rates, *i.e.* $R_{UN} = 34.9\,\%$, $R_{UN} = 17.43\,\%$ and $4.36\,\%$, is shown. By reducing R_{UN} the error increases, as expected. Anyways, the maximum error achieved is below $8\,\mathrm{m}^{-1}$, demonstrating that it is possible to obtain an accurate wavenumber reconstruction even with high compression levels. In Fig. 6.9h, the same analysis is carried on for the HANI dataset at compression rates of $R_{UN} = 34.9\,\%$, $R_{UN} = 17.4\,\%$ and $6.55\,\%$. Similarly to the previous case, the errors oscillate below $8\,\mathrm{m}^{-1}$. Therefore, the same conclusions can be drawn.

The characterization of the OGW dataset results, instead, can not be carried on similarly to SANI and HANI cases. In fact, difficulties arise in the estimation of the optimized elastic constants at lower frequencies, as described in [350]. Thus, an accurate and reliable error characterization based on SAFE simulations is not enabled. Thus, we relied on the DRLSE outputs to characterize those achieved with 2DSWA. In particular, the DRLSE OGW wavenumber profile matches very well the profile drown by the Fourier transform in the

k–space, as it can be observed in Fig. 6.6d. In Fig. 6.9i, 6.9j and 6.9k, the wavenumber reconstructions for $R_{UN} = 83.3\,\%$, $R_{UN} = 41.66\,\%$ and $31.26\,\%$ are depicted. In TABLE 6.2, instead, the maximum and average errors at each compression rate are shown. It can be observed that the performances are comparable for $R_{UN} = 83.3$, $R_{UN} = 41.66$ and $R_{UN} = 31.26$, while the error rises dramatically at R_{UN} lower than $31.26\,\%$. Moreover, it is worthy to notice that the compression rates are significantly higher w.r.t. the other datasets to achieve a good estimation.

6.5.2 Phase and group velocity extraction

In the previous section, it has been demonstrated that DRLSE and 2DSWA methods are able to accurately extract the wavenumber profile of the most energetic propagation mode at the excitation frequency of the datasets characterized. If a precise estimation of the wavenumber profile is performed, the phase and group velocities can be computed as well. The former quantity by exploiting the simple wavenumber–phase velocity relationship:

$$v_p(r,\theta) = \frac{\omega}{k(r,\theta)} \tag{6.19}$$

where ω is the angular frequency. The group velocity estimation, instead, is not trivial due to the derivative operation involved:

$$v_g(r,\theta) = \frac{\partial \omega}{\partial k} \tag{6.20}$$

In literature, the derivative is usually computed only in numerical models, where noise and inaccuracies of experimental data are not involved [270]. Anyway, thanks to the high precision wavenumber reconstructions obtained in this work, we propose to exploit numerical derivatives even with experimental data

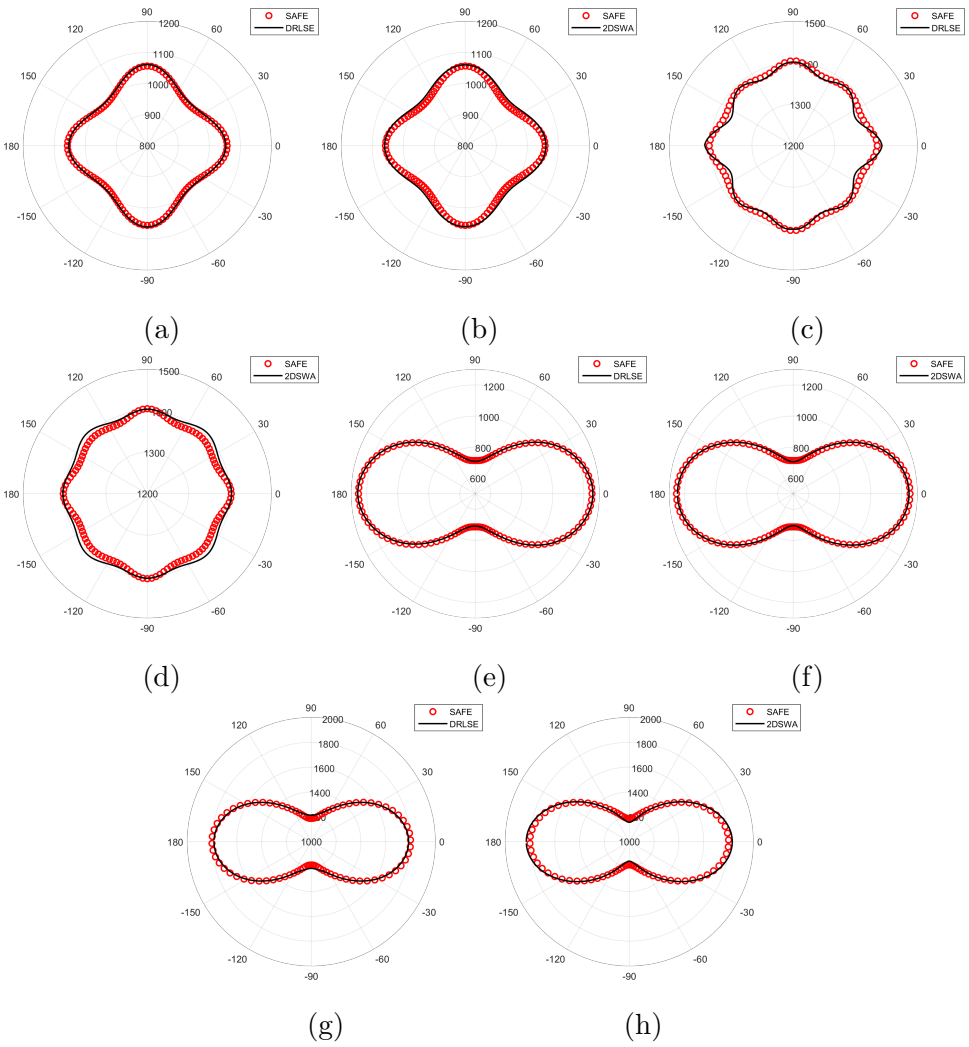

Figure 6.10: Phase and group velocity results ([m/s]) for SANI and HANI datasets. In particular: (a,b) SANI v_p by DRLSE,2DSWA methods. (c,d) SANI v_g by DRLSE,2DSWA methods. (e,f) HANI v_p by DRLSE,2DSWA methods. (g,h) HANI v_g by DRLSE,2DSWA methods [AP10].

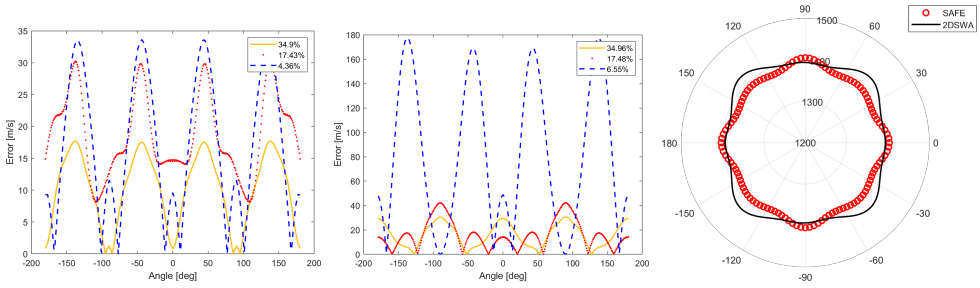

(a) (b) (c)

Figure 6.11: (a,b) v_g error characterization at different R_{UN} for SANI,HANI datasets. (c) SANI v_g at $R_{UN} = 4.36\,\%$ [AP10].

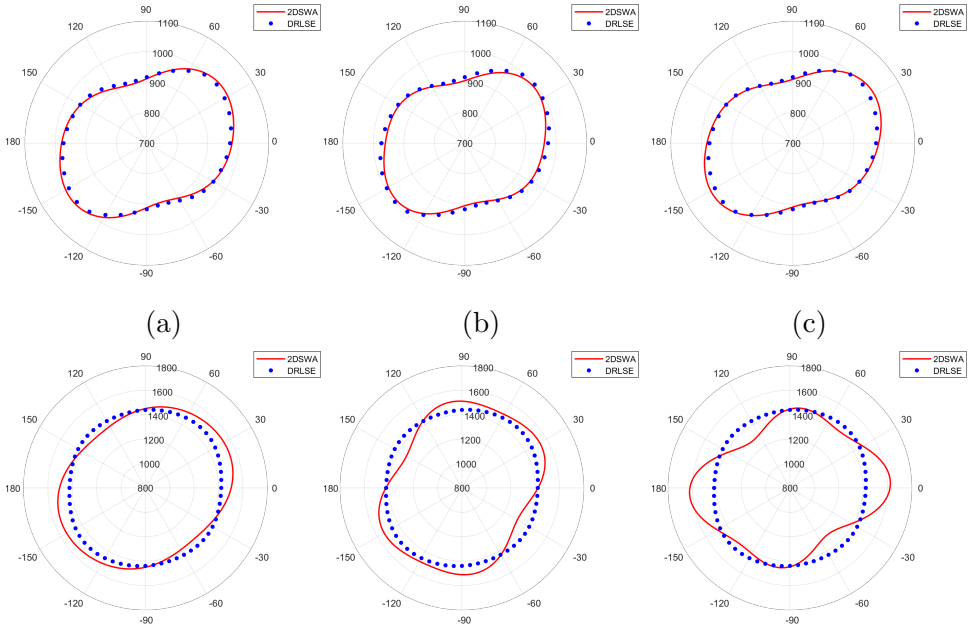

(a) (b) (c)

(d) (e) (f)

Figure 6.12: OGW dataset phase and group velocity results ([m/s]): (a,b,c) v_p at $R_{UN} = 83.28\,\%$, $R_{UN} = 41.66\,\%$, $R_{UN} = 31.26\,\%$. (d,e,f) v_g at $R_{UN} = 83.28\,\%$, $R_{UN} = 41.66\,\%$, $R_{UN} = 31.26\,\%$ [AP10].

as follows. In the SANI and HANI cases, the wavenumber $\mathcal{W}(f, r, \theta)$ has been extracted for frequencies from 42 kHz to 58 kHz, with a step of $\Delta f = 2$ kHz. For instance, in Fig.6.8, the A0 wavenumber profiles extracted by means of DRLSE in (k_x, k_y) coordinates are shown. Blue dots represent wavenumbers values along with the 0° direction, superimposed with the theoretical dispersion curve in black. Then, the $\mathcal{W}(r, f)|_{\theta=\theta_i}$ profile has been interpolated by a second–order polynomial method, reducing the frequency step to 100 Hz at each fixed propagation angle. Finally, the numerical derivative was computed by central difference for interior data points and single-sided differences along the edges of the numerical vector. The procedure is then repeated for each propagation direction. In Fig. 6.10, the computed phase and group velocities are shown. The estimation of the wavenumbers was carried on by the DRLSE and 2DSWA approaches. In the 2DSWA computations, compression rates of $R_{UN} = 34.9\,\%$ and $R_{UN} = 34.96\,\%$ were used for the SANI and HANI velocities extraction, respectively. In TABLE 6.3, the maximum and average errors of the velocities w.r.t. SAFE simulations are shown. It can be observed that the errors of the DRLSE approach are slightly lower in comparison with the 2DSWA in both the SANI and HANI datasets, as expected. Since 2DSWA at 35 % of compression rate was able to satisfactorily reconstruct the dispersion curves, the group velocity estimation with different compression rates has been deepened in order to determine the minimum R_{UN} achievable. In Fig. 6.11, the errors of the group velocity estimations for the SANI and HANI datasets at different R_{UN} are depicted. As expected, by reducing R_{UN} the quality of the group velocities gets worse. In particular, the SANI group velocity reconstruction can be considered successful only for $R_{UN} = 34.95\,\%$ and $R_{UN} = 17.43\,\%$. In fact, even if the errors remain below 35 $^{m}/_{s}$ at a compression rate of 4.36 %, the velocity shape in polar coordinates is not satisfactory and do not follows

	Max[$^m/_s$]	Average [$^m/_s$]
SANI DRLSE v_p	7.48	3.84
SANI 2DSWA v_p	15.31	10.9
HANI DRLSE v_p	8.01	3.36
HANI 2DSWA v_p	14.38	5.91
OGW 2DSWA v_p	12.5	6.79
SANI DRLSE v_g	14.74	5.35
SANI 2DSWA v_g	17.71	10.16
HANI DRLSE v_g	29.04	11.62
HANI 2DSWA v_g	30.6	16.05
OGW 2DSWA v_g	113.53	66.93

Table 6.3: Phase and group velocity errors. In the 2DSWA cases, R_{UN} at 34.9 %, 34.96 % and 83.3 % were considered for the SANI, HANI and OGW datasets, respectively [AP10].

anymore the expected profile (Fig. 6.11c). Similarly, the HANI group velocity is satisfactory at $R_{UN} = 34.9\,\%$ and $R_{UN} = 17.48\,\%$. The error rises dramatically at $R_{UN} = 6.55\,\%$, instead.

In the case of OGW velocity curves, $\mathcal{W}(f, r, \theta)$ has been extracted for frequencies from 50 kHz to 70 kHz, with a step of $\Delta f = 2.5$ kHz, and then interpolated. To facilitate the group velocity estimation, the interpolation frequency step was reduced to $\Delta f = 10$ Hz. In Fig. 6.12 the phase and group velocities are depicted with $R_{UN} = 83.3\,\%$, $R_{UN} = 41.66\,\%$ and $R_{UN} = 31.26\,\%$, from left to right, respectively. Unfortunately, the group velocity errors are not negligible, with a maximum of 113.53 $^m/_s$ and average 66.93 $^m/_s$ at $R_{UN} = 83.3\,\%$. In the other cases, the errors are even higher and, as it can be observed in Fig. 6.12e and 6.12f, the extracted profiles are distorted and do not follow anymore

the expected behaviour. Thus, it is evident that the 2DSWA approach was not able to properly reconstruct the group velocity in this application case. Conversely, the phase velocity computation shows good accordance in all the compression rates addressed.

Chapter 7

Conclusions

This dissertation describes the research work conducted to develop embedded systems and advanced signal processing for Acousto-Ultrasonic Inspections. In particular, this Thesis explores innovative solutions in both SHM and NDT application contexts.

- In the first part, it was discussed how conventional instrumentation for materials and structures inspection is often expensive and bulky, not suitable for permanent monitoring. The recent development of tiny, low–cost and scalable smart sensor networks leads the way to a new SHM paradigm, in which real–time, long–term monitoring is enabled. The development of such kinds of technologies is a pressing need in SHM field for widespread diffusion. In this context, a heterogeneous smart sensor network that features low–weight, low–price and low–power consumption with suitable signal processing has been presented in this Thesis. In detail, a multi–sensor strategy which exploits the simultaneous acquisition of both piezoelectric and MEMS accelerometer signals has been implemented and tested in two different experimental setups. The physical relationship between PZT and ACC data has been verified, and the

effectiveness of piezoelectric transducers for low–frequency application fields such as vibration and modal analysis has been demonstrated. Both the natural frequencies and modal shapes were extracted, the former by adopting an AR +Noise parametric model, the latter, instead, by exploiting a processing scheme that primarily performs a tuning procedure capable to compensate for intrinsic non–idealities in PZT transducers. Thus, the damage detection suitability of the PZT circuitry was profitably assessed. From these results, it can be concluded that low-cost PZT sensors might be used either alone or alongside traditional MEMS accelerometers to efficiently estimate the modal parameters of structures undergoing flexural vibrations with minimal invasivity.

- In the second part, damage localization methods based on Lamb waves inspection have been investigated. In literature, many solutions with distinctive features (high resolution, computational effort, damage detectability, etc) can be found. Among these, the most exploited methods still are DAS and RAPID due to their globally good performance and ease of implementation. In this work, the need of developing solutions that are both performative and straightforward has been addressed. In detail, the Delay Multiply and Sum, and the Double Stage Delay Multiply and Sum have been introduced for SHM and NDT purposes. These techniques can be considered as evolutions of the DAS beamforming algorithm which exploit the enhancement of correlated samples by means of multiplication operations to achieve better contrast and resolution. Moreover, to further improve the beamformings output, a specifically developed filtering approach referred to as Fresnel Zone Filtering has been introduced. In particular, FZF enhances ultrasonic beams which interact constructively with the damage scatters in the first Fresnel zone, reduc-

ing noise and artefacts. The methods have been validated and compared on a carbon fibre plate with artificial damages in a standard pitch–catch, round–robin ultrasonic inspection. The imaging results characterized by CR , PSNR and gCNR metrics show a clear trend in which DMAS enhances DAS image quality, while DS-DMAS outperforms both DAS and DMAS . Finally, each beamforming algorithm is significantly improved by the exploitation of FZF , demonstrating the effectiveness of the proposed approach. Nevertheless, the proposed localization methods are limited by the precision of the group velocity model, especially in highly anisotropic plates. A comprehensive method that can directly address the extraction of the dispersion curves in polar coordinates at a given frequency along with all the directions simultaneously does not exist in literature. Thus, innovative solutions have been developed to address this need. In particular, by exploiting scanner laser Doppler vibrometer measurements, two different signal processing techniques have been investigated and compared. The first approach relies on the extraction of the wavenumber profile in the wavenumber domain obtained by 3DFT and proper signal processing. A DRLSE algorithm has been used to precisely determine the wavenumber profile in the Fourier domain at a fixed frequency. The second approach, namely the 2DSWA, is based on subsampling the wavefield in the frequency–space domain in order to extract the Wavenumber profile by a 2–D OMP strategy that exploits the inherent signal sparsity. Then, phase and group velocities were extracted. The techniques have been validated on datasets related to carbon fiber plates with different anisotropy degrees and propagation properties. It has been demonstrated the capability of both the algorithms to accurately extract the wavenumber profile in all the case scenarios. Mean-

while, 2D–SWA struggles in the evaluation of the group velocity where the dataset is characterized by low signal–to–noise ratio and complex propagation behavior. From this analysis, it can be concluded that the DRLSE method is a robust and reliable technique for the wavenumber and velocities extraction in polar coordinates at a given frequency thanks to its flexibility in the signal pre/post processing. While the 2DSWA is a viable alternative in high signal–to–noise ratio measurements to speed up the characterization of materials.

7.1 Future work developments

The results described in this dissertation open the way to different future work developments which might further improve the state–of–the–art. In particular, the following extensions and improvements can be addressed.

- The capabilities of the proposed heterogeneous smart sensor network in a real application scenario for long–term monitoring will be investigated. Moreover, the possibility to insert more sensing elements (strain gauges, temperature and humidity sensors, etc.) will be investigated, such as the development of suitable data merging algorithms.

- The beamforming algorithms will be extended to allow them to handle multidamage cases, multimodal, dispersive and highly anisotropic waves propagation. For instance, the damage localization phase can be integrated with spatial clustering algorithms, *e.g.* DBSCAN, or machine learning methods to cluster and characterize multiple damages. Dispersion compensation, instead, can be addressed by exploiting, for instance, the Warping Frequency Transform described in [188] [AP11], while complex anisotropic velocity models can be inserted in the beamforming de-

lay terms computation. In particular, the DRLSE approach described in chapter 6 can be used for accurate velocity estimation enabling specific correction procedures such the one described in [266]. Finally, the validation of the proposed method in more complex application scenarios will be addressed by exploiting the open dataset described in Marzani et al. [303], which collects pitch–catch ultrasonic measurements in a real full scale aeronautical structure.

- The proposed DRLSE–based approach for the extraction of the polar representation of dispersion curves will be extended to the 3–D case for broadband measurements. So far, a multifrequency analysis can be carried on by performing the DRLSE at each frequency. A 3–D–DRLSE, instead, would speed up the procedure enabling an automatic and complete 3–D dispersion characterization. Moreover, to deal simultaneously with multiple modes, the DRLSE will be adapted for the identification of multiple concentric shapes.

Bibliography

[1] O. H. Amman, T. von Kármán, and G. B. Woodruff, "The failure of the tacoma narrows bridge," 1941.

[2] D. Mitchell, J. Marchand, P. Croteau, and W. D. Cook, "Concorde overpass collapse: structural aspects," *Journal of performance of constructed facilities*, vol. 25, no. 6, pp. 545–553, 2011.

[3] G. M. Calvi, M. Moratti, G. J. O'Reilly, N. Scattarreggia, R. Monteiro, D. Malomo, P. M. Calvi, and R. Pinho, "Once upon a time in italy: The tale of the morandi bridge," *Structural Engineering International*, vol. 29, no. 2, pp. 198–217, 2019.

[4] H. A. Kinnison and T. Siddiqui, "Aviation maintenance management," 2013.

[5] T. Aastroem, "From fifteen to two hundred ndt-methods in fifty years," in *17th World Conference on Nondestructive Testing*. Citeseer, 2008, pp. 25–28.

[6] L. Capineri and A. Bulletti, "Ultrasonic guided-waves sensors and integrated structural health monitoring systems for impact detection and localization: A review," *Sensors*, vol. 21, no. 9, 2021. [Online]. Available: https://www.mdpi.com/1424-8220/21/9/2929

[7] D. Balageas, C.-P. Fritzen, and A. Güemes, *Structural health monitoring*. John Wiley & Sons, 2010, vol. 90.

[8] P. J. Shull, *Nondestructive evaluation: theory, techniques, and applications*. CRC press, 2002.

[9] D. J. Inman, C. R. Farrar, V. L. Junior, and V. S. Junior, *Damage prognosis: for aerospace, civil and mechanical systems*. John Wiley & Sons, 2005.

[10] Y. Liu, S. Mohanty, and A. Chattopadhyay, "Condition based structural health monitoring and prognosis of composite structures under uniaxial and biaxial loading," *Journal of Nondestructive Evaluation*, vol. 29, no. 3, pp. 181–188, 2010.

[11] N. Eleftheroglou, D. Zarouchas, T. Loutas, R. Alderliesten, and R. Benedictus, "Structural health monitoring data fusion for in-situ life prognosis of composite structures," *Reliability Engineering & System Safety*, vol. 178, pp. 40–54, 2018.

[12] J. Chen, S. Yuan, C. Sbarufatti, and X. Jin, "Dual crack growth prognosis by using a mixture proposal particle filter and on-line crack monitoring," *Reliability Engineering & System Safety*, vol. 215, p. 107758, 2021.

[13] E. ASTM *et al.*, "Standard terminology for nondestructive examinations," 2006.

[14] S. Gholizadeh, Z. Leman, and B. H. T. Baharudin, "A review of the application of acoustic emission technique in engineering," *Structural Engineering and Mechanics*, vol. 54, no. 6, pp. 1075–1095, 2015.

[15] S. Grondel, C. Delebarre, J. Assaad, J.-P. Dupuis, and L. Reithler, "Fatigue crack monitoring of riveted aluminium strap joints by lamb wave analysis and acoustic emission measurement techniques," *Ndt & E International*, vol. 35, no. 3, pp. 137–146, 2002.

[16] V. Kietov, S. Henschel, and L. Krüger, "Study of dynamic crack formation in nodular cast iron using the acoustic emission technique," *Engineering Fracture Mechanics*, vol. 188, pp. 58–69, 2018.

[17] Z. Gong, E. Nyborg, and G. Oommen, "Acoustic emission monitoring of steel railroad bridges," *Materials evaluation*, vol. 50, no. 7, 1992.

[18] V. Perfilyev, I. Lapsker, A. Laikhtman, and L. Rapoport, "Scratching of copper and silicon: acoustic emission analysis," *Tribology Letters*, vol. 65, no. 1, pp. 1–10, 2017.

[19] P. Alander, L. V. Lassila, A. Tezvergil, and P. K. Vallittu, "Acoustic emission analysis of fiber-reinforced composite in flexural testing," *Dental Materials*, vol. 20, no. 4, pp. 305–312, 2004.

[20] L. Golaski, P. Gebski, and K. Ono, "Diagnostics of reinforced concrete bridges by acoustic emission," *Journal of acoustic emission*, vol. 20, no. 2002, pp. 83–89, 2002.

[21] S. Kawamoto, "Acoustic emission and acousto-ultrasonic techniques for wood and wood-based composites: a review," 2002.

[22] A. Nair and C. Cai, "Acoustic emission monitoring of bridges: Review and case studies," *Engineering structures*, vol. 32, no. 6, pp. 1704–1714, 2010.

[23] C. Ennaceur, A. Laksimi, C. Herve, and M. Cherfaoui, "Monitoring crack growth in pressure vessel steels by the acoustic emission technique and the method of potential difference," *International journal of pressure vessels and piping*, vol. 83, no. 3, pp. 197–204, 2006.

[24] J.-R. Kwon, G.-J. Lyu, T.-H. Lee, and J.-Y. Kim, "Acoustic emission testing of repaired storage tank," *International journal of pressure vessels and piping*, vol. 78, no. 5, pp. 373–378, 2001.

[25] K. M. Holford, R. Pullin, S. L. Evans, M. J. Eaton, J. Hensman, and K. Worden, "Acoustic emission for monitoring aircraft structures," *Proceedings of the Institution of Mechanical Engineers, Part G: Journal of Aerospace Engineering*, vol. 223, no. 5, pp. 525–532, 2009.

[26] P. Joosse, M. Blanch, A. Dutton, D. Kouroussis, T. Philippidis, and P. Vionis, "Acoustic emission monitoring of small wind turbine blades," *J. Sol. Energy Eng.*, vol. 124, no. 4, pp. 446–454, 2002.

[27] K. Ono, "Review on structural health evaluation with acoustic emission," *Applied Sciences*, vol. 8, no. 6, p. 958, 2018.

[28] S. Grondel, J. Assaad, C. Delebarre, and E. Moulin, "Health monitoring of a composite wingbox structure," *Ultrasonics*, vol. 42, no. 1-9, pp. 819–824, 2004.

[29] J. P. McCrory, S. K. Al-Jumaili, D. Crivelli, M. R. Pearson, M. J. Eaton, C. A. Featherston, M. Guagliano, K. M. Holford, and R. Pullin, "Damage classification in carbon fibre composites using acoustic emission: A comparison of three techniques," *Composites Part B: Engineering*, vol. 68, pp. 424–430, 2015.

[30] H. Sohn and C. R. Farrar, "Damage diagnosis using time series analysis of vibration signals," *Smart materials and structures*, vol. 10, no. 3, p. 446, 2001.

[31] M. Johnson, "Waveform based clustering and classification of ae transients in composite laminates using principal component analysis," *Ndt & e International*, vol. 35, no. 6, pp. 367–376, 2002.

[32] N. Godin, S. Huguet, R. Gaertner, and L. Salmon, "Clustering of acoustic emission signals collected during tensile tests on unidirectional glass/polyester composite using supervised and unsupervised classifiers," *Ndt & E International*, vol. 37, no. 4, pp. 253–264, 2004.

[33] A. R. Oskouei, H. Heidary, M. Ahmadi, and M. Farajpur, "Unsupervised acoustic emission data clustering for the analysis of damage mechanisms in glass/polyester composites," *Materials & Design*, vol. 37, pp. 416–422, 2012.

[34] H. Towsyfyan, A. Biguri, R. Boardman, and T. Blumensath, "Successes and challenges in non-destructive testing of aircraft composite structures," *Chinese Journal of Aeronautics*, vol. 33, no. 3, pp. 771–791, 2020.

[35] S. Garcea, Y. Wang, and P. Withers, "X-ray computed tomography of polymer composites," *Composites Science and Technology*, vol. 156, pp. 305–319, 2018.

[36] S. Garcea, I. Sinclair, and S. Spearing, "In situ synchrotron tomographic evaluation of the effect of toughening strategies on fatigue micromechanisms in carbon fibre reinforced polymers," *Composites Science and Technology*, vol. 109, pp. 32–39, 2015.

[37] ——, "Fibre failure assessment in carbon fibre reinforced polymers under fatigue loading by synchrotron x-ray computed tomography," *Composites Science and Technology*, vol. 133, pp. 157–164, 2016.

[38] J.-Y. Buffiere, E. Maire, J. Adrien, J.-P. Masse, and E. Boller, "In situ experiments with x ray tomography: an attractive tool for experimental mechanics," *Experimental mechanics*, vol. 50, no. 3, pp. 289–305, 2010.

[39] Y. Yang, Y. Zhang, and X. Tan, "Review on vibration-based structural health monitoring techniques and technical codes," *Symmetry*, vol. 13, no. 11, p. 1998, 2021.

[40] D. Capecchi, J. Ciambella, A. Pau, and F. Vestroni, "Damage identification in a parabolic arch by means of natural frequencies, modal shapes and curvatures," *Meccanica*, vol. 51, no. 11, pp. 2847–2859, 2016.

[41] N. T. Khiem and H. T. Tran, "A procedure for multiple crack identification in beam-like structures from natural vibration mode," *Journal of Vibration and Control*, vol. 20, no. 9, pp. 1417–1427, 2014.

[42] M. Friswell and J. E. Mottershead, *Finite element model updating in structural dynamics*. Springer Science & Business Media, 1995, vol. 38.

[43] G. Ghodrati Amiri, S. Seyed Razzaghi, and A. Bagheri, "Damage detection in plates based on pattern search and genetic algorithms," *Smart Structures and Systems*, vol. 7, no. 2, pp. 117–132, 2011.

[44] A. C. Neves, I. Gonzalez, J. Leander, and R. Karoumi, "Structural health monitoring of bridges: a model-free ann-based approach to damage detection," *Journal of Civil Structural Health Monitoring*, vol. 7, no. 5, pp. 689–702, 2017.

[45] X. Ye, T. Jin, and C. Yun, "A review on deep learning-based structural health monitoring of civil infrastructures," *Smart Struct Syst*, vol. 24, no. 5, pp. 567–586, 2019.

[46] T. Yin, Q.-H. Jiang, and K.-V. Yuen, "Vibration–based damage detection for structural connections using incomplete modal data by bayesian approach and model reduction technique," *Engineering Structures*, vol. 132, pp. 260–277, 2017.

[47] O. Williams, A. Blake, and R. Cipolla, "Sparse bayesian learning for efficient visual tracking," *IEEE Transactions on Pattern Analysis and Machine Intelligence*, vol. 27, no. 8, pp. 1292–1304, 2005.

[48] M. H. Rafiei and H. Adeli, "A novel unsupervised deep learning model for global and local health condition assessment of structures," *Engineering Structures*, vol. 156, pp. 598–607, 2018.

[49] Z. Ding, R. Yao, J. Li, and Z. Lu, "Structural damage identification based on modified artificial bee colony algorithm using modal data," *Inverse Problems in Science and Engineering*, vol. 26, no. 3, pp. 422–442, 2018.

[50] A. Sophian, G. Tian, D. Taylor, and J. Rudlin, "Electromagnetic and eddy current ndt: a review," *Insight*, vol. 43, no. 5, pp. 302–306, 2001.

[51] P. Underhill and T. Krause, "Eddy current analysis of mid-bore and corner cracks in bolt holes," *NDT & E International*, vol. 44, no. 6, pp. 513–518, 2011.

[52] J. Szlagowska-Spychalska, M. Spychalski, and K. Kurzydlowski, "A novel approach for measuring of thickness of induction hardened layers based on the eddy current method and the finite element modeling," *NDT & E International*, vol. 54, pp. 56–62, 2013.

[53] A. Shakoor and Z. Zhenggan, "Investigation of 3d anisotropic electrical conductivity in tig welded 5a06 al alloy using eddy currents," *Journal of Materials Processing Technology*, vol. 211, no. 11, pp. 1736–1741, 2011.

[54] A. Ortona, C. D'Angelo, and G. Bianchi, "Monitoring sandwich structured sic ceramics integrity with electrical resistance," *NDT & E International*, vol. 46, pp. 77–82, 2012.

[55] A. Bernieri, G. Betta, L. Ferrigno, and M. Laracca, "Crack depth estimation by using a multi-frequency ect method," *IEEE Transactions on Instrumentation and Measurement*, vol. 62, no. 3, pp. 544–552, 2013.

[56] A. Sophian, G. Tian, and M. Fan, "Pulsed eddy current non-destructive testing and evaluation: A review," *Chinese Journal of Mechanical Engineering*, vol. 30, no. 3, pp. 500–514, 2017.

[57] I. Z. Abidin, C. Mandache, G. Y. Tian, and M. Morozov, "Pulsed eddy current testing with variable duty cycle on rivet joints," *NDT & e International*, vol. 42, no. 7, pp. 599–605, 2009.

[58] S. Hosseini and A. A. Lakis, "Application of time–frequency analysis for automatic hidden corrosion detection in a multilayer aluminum structure using pulsed eddy current," *Ndt & E International*, vol. 47, pp. 70–79, 2012.

[59] M. Pan, Y. He, G. Tian, D. Chen, and F. Luo, "Defect characterisation using pulsed eddy current thermography under transmission mode and ndt applications," *Ndt & E International*, vol. 52, pp. 28–36, 2012.

[60] G. Zenzinger, J. Bamberg, W. Satzger, and V. Carl, "Thermographic crack detection by eddy current excitation," *Nondestructive Testing and Evaluation*, vol. 22, no. 2-3, pp. 101–111, 2007.

[61] I. Z. Abidin, G. Y. Tian, J. Wilson, S. Yang, and D. Almond, "Quantitative evaluation of angular defects by pulsed eddy current thermography," *Ndt & E International*, vol. 43, no. 7, pp. 537–546, 2010.

[62] J. Krautkrämer and H. Krautkrämer, *Ultrasonic testing of materials*. Springer Science & Business Media, 2013.

[63] D. Chimenti, "Review of air-coupled ultrasonic materials characterization," *Ultrasonics*, vol. 54, no. 7, pp. 1804–1816, 2014. [Online]. Available: https://www.sciencedirect.com/science/article/pii/S0041624X14000377

[64] C. Scruby, "Some applications of laser ultrasound," *Ultrasonics*, vol. 27, no. 4, pp. 195–209, 1989. [Online]. Available: https://www.sciencedirect.com/science/article/pii/0041624X89900437

[65] J. Isla and F. Cegla, "Emat phased array: A feasibility study of surface crack detection," *Ultrasonics*, vol. 78, pp. 1–9, 2017. [Online]. Available: https://www.sciencedirect.com/science/article/pii/S0041624X16302785

[66] J. Achenbach, "Quantitative nondestructive evaluation," *International Journal of Solids and Structures*, vol. 37, no. 1, pp. 13–27, 2000. [Online]. Available: https://www.sciencedirect.com/science/article/pii/S0020768399000748

[67] P. Doyle and C. Scala, "Crack depth measurement by ultrasonics: a review," *Ultrasonics*, vol. 16, no. 4, pp. 164–170, 1978.

[68] M. Silk, "The use of diffraction-based time-of-flight measurements to locate and size defects," *British Journal of Non-destructive Testing*, vol. 26, no. 4, pp. 208–213, 1984.

[69] A. Velichko and P. D. Wilcox, "An analytical comparison of ultrasonic array imaging algorithms," *The Journal of the Acoustical Society of America*, vol. 127, no. 4, pp. 2377–2384, 2010.

[70] C. Prada, F. Wu, and M. Fink, "The iterative time reversal mirror: A solution to self-focusing in the pulse echo mode," *The Journal of the Acoustical Society of America*, vol. 90, no. 2, pp. 1119–1129, 1991.

[71] M. V. Felice and Z. Fan, "Sizing of flaws using ultrasonic bulk wave testing: A review," *Ultrasonics*, vol. 88, pp. 26–42, 2018.

[72] N. Testoni, F. Zonzini, A. Marzani, V. Scarponi, and L. De Marchi, "A tilt sensor node embedding a data-fusion algorithm for vibration-based shm," *Electronics*, vol. 8, no. 1, p. 45, 2019.

[73] C. Scuro, P. F. Sciammarella, F. Lamonaca, R. S. Olivito, and D. L. Carni, "Iot for structural health monitoring," *IEEE Instrumentation & Measurement Magazine*, vol. 21, no. 6, pp. 4–14, 2018.

[74] M. Abdulkarem, K. Samsudin, F. Z. Rokhani, and M. F. A Rasid, "Wireless sensor network for structural health monitoring: A contemporary review of technologies, challenges, and future direction," *Structural Health Monitoring*, vol. 19, no. 3, pp. 693–735, 2020.

[75] R. A. Swartz, D. Jung, J. P. Lynch, Y. Wang, D. Shi, and M. P. Flynn, "Design of a wireless sensor for scalable distributed in-network computation in a structural health monitoring system," in *Proceedings of the 5th International Workshop on Structural Health Monitoring*, 2005, pp. 12–14.

[76] Y. Wang, J. P. Lynch, and K. H. Law, "A wireless structural health monitoring system with multithreaded sensing devices: design and validation," *Structure and Infrastructure Engineering*, vol. 3, no. 2, pp. 103–120, 2007.

[77] D. D. Mascarenas, E. B. Flynn, M. D. Todd, T. G. Overly, K. M. Farinholt, G. Park, and C. R. Farrar, "Development of capacitance-based and impedance-based wireless sensors and sensor nodes for structural health monitoring applications," *Journal of Sound and Vibration*, vol. 329, no. 12, pp. 2410–2420, 2010.

[78] T. Harms, B. Banks, S. S. Sarvestani, and F. Bastianini, "Design and testing of a low-power wireless sensor network for structural health monitoring of bridges," in *Sensors and Smart Structures Technologies for Civil, Mechanical, and Aerospace Systems 2009*, vol. 7292. International Society for Optics and Photonics, 2009, p. 72920U.

[79] E. Sazonov, V. Krishnamurthy, and R. Schilling, "Wireless intelligent sensor and actuator network-a scalable platform for time-synchronous applications of structural health monitoring," *Structural Health Monitoring*, vol. 9, no. 5, pp. 465–476, 2010.

[80] Q. Huang, B. Tang, and L. Deng, "Development of high synchronous acquisition accuracy wireless sensor network for machine vibration monitoring," *Measurement*, vol. 66, pp. 35–44, 2015.

[81] H. Yao, H. Cao, and J. Li, "Design and implementation of a portable wireless system for structural health monitoring," *Measurement and Control*, vol. 49, no. 1, pp. 23–32, 2016.

[82] Á. Lédeczi, P. Völgyesi, E. Barth, A. Nádas, A. Pedchenko, T. Hay, and S. Jayaraman, "Self-sustaining wireless acoustic emission sensor system for bridge monitoring," in *New Developments in Sensing Technology for Structural Health Monitoring*. Springer, 2011, pp. 15–39.

[83] L. Zhu, Y. Fu, R. Chow, B. F. Spencer, J. W. Park, and K. Mechitov, "Development of a high-sensitivity wireless accelerometer for structural health monitoring," *Sensors*, vol. 18, no. 1, p. 262, 2018.

[84] A. Shrestha and L. Xing, "A performance comparison of different topologies for wireless sensor networks," in *2007 IEEE Conference on Technologies for Homeland Security*. IEEE, 2007, pp. 280–285.

[85] A. R. Scott, "Characterizing system health using modal analysis," *IEEE Transactions on Instrumentation and Measurement*, vol. 58, no. 2, pp. 297–302, 2008.

[86] A. Brandt, *Noise and vibration analysis: signal analysis and experimental procedures*. John Wiley & Sons, 2011.

[87] R. Duan and F. Wang, "Fault diagnosis of on-load tap-changer in converter transformer based on time–frequency vibration analysis," *IEEE Transactions on Industrial Electronics*, vol. 63, no. 6, pp. 3815–3823, 2016.

[88] W. Fan and P. Qiao, "Vibration-based damage identification methods: a review and comparative study," *Structural health monitoring*, vol. 10, no. 1, pp. 83–111, 2011.

[89] N. Testoni, C. Aguzzi, V. Arditi, F. Zonzini, L. De Marchi, A. Marzani, and T. S. Cinotti, "A sensor network with embedded data processing and data-to-cloud capabilities for vibration-based real-time shm," *Journal of Sensors*, vol. 2018, 2018.

[90] C. Bedon, E. Bergamo, M. Izzi, and S. Noè, "Prototyping and validation of mems accelerometers for structural health monitoring-the case study of the pietratagliata cable-stayed bridge," *Journal of Sensor and Actuator Networks*, vol. 7, no. 3, p. 30, 2018.

[91] G. Piana, E. Lofrano, A. Carpinteri, A. Paolone, and G. Ruta, "Experimental modal analysis of straight and curved slender beams by piezoelectric transducers," *Meccanica*, vol. 51, no. 11, pp. 2797–2811, 2016.

[92] A. Belisario-Briceño, S. F. Zedek, T. Camps, R. François, C. Escriba, and J.-Y. Fourniols, "Shm based on modal analysis: accelerometer and piezoelectric transducers instrumentation for civil engineering in heterogeneous structures," in *EWSHM-7th European Workshop on Structural Health Monitoring*, 2014.

[93] H. Wang and P. Chen, "Intelligent diagnosis method for a centrifugal pump using features of vibration signals," *Neural Computing and Applications*, vol. 18, no. 4, pp. 397–405, 2009.

[94] C. Acar and A. M. Shkel, "Experimental evaluation and comparative analysis of commercial variable-capacitance mems accelerometers," *Journal of Micromechanics and Microengineering*, vol. 13, no. 5, p. 634, 2003.

[95] A. Sabato, C. Niezrecki, and G. Fortino, "Wireless mems-based accelerometer sensor boards for structural vibration monitoring: a review," *IEEE Sensors Journal*, vol. 17, no. 2, pp. 226–235, 2017.

[96] R. R. Ribeiro and R. d. M. Lameiras, "Evaluation of low-cost mems accelerometers for shm: frequency and damping identification of civil structures," *Latin American Journal of Solids and Structures*, vol. 16, no. 7, 2019.

[97] G. Lacidogna, G. Piana, and A. Carpinteri, "Damage monitoring of three-point bending concrete specimens by acoustic emission and resonant frequency analysis," *Engineering Fracture Mechanics*, vol. 210, pp. 203–211, 2019.

[98] C. Devriendt, F. Magalhães, W. Weijtjens, G. De Sitter, Á. Cunha, and P. Guillaume, "Structural health monitoring of offshore wind turbines using automated operational modal analysis," *Structural Health Monitoring*, vol. 13, no. 6, pp. 644–659, 2014.

[99] K.-Y. Oh, J.-Y. Park, J.-S. Lee, B. I. Epureanu, and J.-K. Lee, "A novel method and its field tests for monitoring and diagnosing blade health for wind turbines," *IEEE Transactions on Instrumentation and Measurement*, vol. 64, no. 6, pp. 1726–1733, 2015.

[100] N. Testoni, L. De Marchi, and A. Marzani, "A stamp size, 40ma, 5 grams sensor node for impact detection and location," in *European Workshop on SHM*, 2016.

[101] *STM32F303xB STM32F303xC Datasheet – production data*, STMicroelectronics, 10 2018, rev. 14.

[102] K. A. Jenkins and J. P. Eckhardt, "Measuring jitter and phase error in microprocessor phase-locked loops," *IEEE Design & Test of Computers*, vol. 17, no. 2, pp. 86–93, 2000.

[103] A. Araujo, J. García-Palacios, J. Blesa, F. Tirado, E. Romero, A. Samartín, and O. Nieto-Taladriz, "Wireless measurement system for structural health monitoring with high time-synchronization accuracy," *IEEE Transactions on instrumentation and measurement*, vol. 61, no. 3, pp. 801–810, 2011.

[104] J. e. a. Postel, "Rfc 793: Transmission control protocol," 1981.

[105] C. Rainieri and G. Fabbrocino, "Operational modal analysis of civil engineering structures," *Springer, New York*, vol. 142, p. 143, 2014.

[106] P. Stoica, R. L. Moses *et al.*, *Spectral analysis of signals*. Pearson Prentice Hall Upper Saddle River, NJ, 2005.

[107] R. Guidorzi, R. Diversi, L. Vincenzi, C. Mazzotti, and V. Simioli, "Structural monitoring of a tower by means of mems-based sensing and enhanced autoregressive models," *European Journal of Control*, vol. 20, no. 1, pp. 4–13, 2014.

[108] R. Guidorzi, R. Diversi, L. Vincenzi, and V. Simioli, "Ar+ noise versus ar and arma models in shm-oriented identification," in *2015 23rd Mediterranean Conference on Control and Automation (MED)*. IEEE, 2015, pp. 809–814.

[109] R. Diversi, R. Guidorzi, and U. Soverini, "Identification of autoregressive models in the presence of additive noise," *International Journal of Adaptive Control and Signal Processing*, vol. 22, no. 5, pp. 465–481, 2008.

[110] S. Mostafavian, S. R. Nabavian, M. R. Davoodi, and B. Navayi Neya, "Output-only modal analysis of a beam via frequency domain decomposition method using noisy data," *International Journal of Engineering*, vol. 32, no. 12, pp. 1753–1761, 2019.

[111] O. Salawu, "Detection of structural damage through changes in frequency: a review," *Engineering structures*, vol. 19, no. 9, pp. 718–723, 1997.

[112] R. Brincker and C. Ventura, *Introduction to operational modal analysis*. John Wiley & Sons, 2015.

[113] R. A. Ibrahim, *Handbook of Structural Life Assessment*. Wiley Online Library, 2017.

[114] L. Rayleigh, "On waves propagated along the plane surface of an elastic solid," *Proceedings of the London mathematical Society*, vol. 1, no. 1, pp. 4–11, 1885.

[115] H. Lamb, "On waves in an elastic plate," *Proceedings of the Royal Society of London. Series A, Containing papers of a mathematical and physical character*, vol. 93, no. 648, pp. 114–128, 1917.

[116] A. E. H. Love, *A treatise on the mathematical theory of elasticity*. Cambridge university press, 2013.

[117] R. Stoneley, "Elastic waves at the surface of separation of two solids," *Proceedings of the Royal Society of London. Series A, Containing Papers of a Mathematical and Physical Character*, vol. 106, no. 738, pp. 416–428, 1924.

[118] W. J. Staszewski, "Structural health monitoring using guided ultrasonic waves," in *Advances in smart technologies in structural engineering*. Springer, 2004, pp. 117–162.

[119] M. Hinderdael, Z. Jardon, J. Ertveldt, and P. Guillaume, "Structural health monitoring through surface acoustic wave inspection deployed on capillaries embedded in additively manufactured components," in *MATEC Web of Conferences*, vol. 349. EDP Sciences, 2021, p. 03010.

[120] J. M. Hughes, J. Vidler, C.-T. Ng, A. Khanna, M. Mohabuth, L. F. Rose, and A. Kotousov, "Comparative evaluation of in situ stress monitoring with rayleigh waves," *Structural Health Monitoring*, vol. 18, no. 1, pp. 205–215, 2019.

[121] N. Galarza, B. Rubio, A. Diez, F. Boto, D. Gil, J. Rubio, E. Moreno *et al.*, "Implementation of signal processing methods in a structural health

monitoring (shm) system based on ultrasonic guided waves for defect detection in different materials and structures," *The e-Journal of Nondestructive Testing & Ultrasonics*, 2016.

[122] R. Eslick, G. Tsoflias, and D. Steeples, "Field investigation of love waves in near-surface seismology," *Geophysics*, vol. 73, no. 3, pp. G1–G6, 2008.

[123] Z. Su, L. Ye, and Y. Lu, "Guided lamb waves for identification of damage in composite structures: A review," *Journal of sound and vibration*, vol. 295, no. 3-5, pp. 753–780, 2006.

[124] D. Worlton, "Experimental confirmation of lamb waves at megacycle frequencies," *Journal of applied physics*, vol. 32, no. 6, pp. 967–971, 1961.

[125] G. M. Ramalho, A. M. Lopes, and L. F. da Silva, "Structural health monitoring of adhesive joints using lamb waves: A review," *Structural Control and Health Monitoring*, p. e2849, 2021.

[126] J. L. Rose, *Ultrasonic guided waves in solid media*. Cambridge university press, 2014.

[127] H. Miao and F. Li, "Shear horizontal wave transducers for structural health monitoring and nondestructive testing: A review," *Ultrasonics*, vol. 114, p. 106355, 2021.

[128] J. L. Rose, "Ultrasonic waves in solid media," 2000.

[129] A. Khennane, *Introduction to finite element analysis using MATLAB® and abaqus*. CRC Press, 2013.

[130] C.-T. Ng, "On the selection of advanced signal processing techniques for guided wave damage identification using a statistical approach," *Engineering Structures*, vol. 67, pp. 50–60, 2014.

[131] B. Lee and W. Staszewski, "Sensor location studies for damage detection with lamb waves," *Smart materials and structures*, vol. 16, no. 2, p. 399, 2007.

[132] S. Carrino, F. Nicassio, G. Scarselli, and R. Vitolo, "Finite difference model of wave motion for structural health monitoring of single lap joints," *International Journal of Solids and Structures*, vol. 161, pp. 219–227, 2019.

[133] A. Marzani, P. Bocchini, E. Viola, I. Bartoli, S. Coccia, S. Salamone, and F. L. di Scalea, "A software for the computation of acoustic waves in cylindrical, plate and arbitrary cross-section waveguides," in *attidella 13a Congresso Nazionale sulle prove non distruttive Monitoraggio e diagnostica AIPnD, Roma, Italia*, 2009, pp. 1–9.

[134] P. Bocchini, A. Marzani, and E. Viola, "Graphical user interface for guided acoustic waves," *Journal of Computing in Civil Engineering*, vol. 25, no. 3, pp. 202–210, 2011.

[135] A. Marzani, *Guided wave modeling for bond inspection in aerospace structures*. University of California, San Diego, 2004.

[136] I. Bartoli, A. Marzani, F. L. Di Scalea, and E. Viola, "Modeling wave propagation in damped waveguides of arbitrary cross-section," *Journal of sound and vibration*, vol. 295, no. 3-5, pp. 685–707, 2006.

[137] A. Marzani, "Time–transient response for ultrasonic guided waves propagating in damped cylinders," *International Journal of Solids and Structures*, vol. 45, no. 25-26, pp. 6347–6368, 2008.

[138] A. Marzani and I. Bartoli, "High frequency waves propagating in octagonal bars: a low cost computation algorithm," *Algorithms*, vol. 2, no. 1, pp. 227–246, 2009.

[139] B. Lee and W. Staszewski, "Modelling of lamb waves for damage detection in metallic structures: Part i. wave propagation," *Smart materials and structures*, vol. 12, no. 5, p. 804, 2003.

[140] Y. Shen and C. E. Cesnik, "Modeling of nonlinear interactions between guided waves and fatigue cracks using local interaction simulation approach," *Ultrasonics*, vol. 74, pp. 106–123, 2017.

[141] Z. Su and L. Ye, *Identification of damage using Lamb waves: from fundamentals to applications*. Springer Science & Business Media, 2009, vol. 48.

[142] G. Yan, "A bayesian approach for damage localization in plate-like structures using lamb waves," *Smart Materials and Structures*, vol. 22, no. 3, p. 035012, 2013.

[143] N. Mori, S. Biwa, and T. Kusaka, "Damage localization method for plates based on the time reversal of the mode-converted lamb waves," *Ultrasonics*, vol. 91, pp. 19–29, 2019.

[144] C. Su, M. Jiang, S. Lv, S. Lu, L. Zhang, F. Zhang, and Q. Sui, "Improved damage localization and quantification of cfrp using lamb waves and convolution neural network," *IEEE Sensors Journal*, vol. 19, no. 14, pp. 5784–5791, 2019.

[145] J. Moll, J. Kathol, C.-P. Fritzen, M. Moix-Bonet, M. Rennoch, M. Koerdt, A. S. Herrmann, M. G. Sause, and M. Bach, "Open guided waves: online platform for ultrasonic guided wave measurements," *Structural Health Monitoring*, vol. 18, no. 5-6, pp. 1903–1914, 2019.

[146] X. Ma, K. Bian, J.-y. Lu, and K. Xiong, "Experimental research on detection for interface debond of cfrp t-joints under tensile load," *Composite Structures*, vol. 158, pp. 359–368, 2016.

[147] G. Alleman, M. Pelt, and R. Groves, "Air-coupled ultrasound for damage detection in cfrp using lamb waves and ultrasonic verification," in *Proc. ICAST2014: 25nd International Conference on Adaptive Structures and Technologies, The Hague*, 2014.

[148] D. N. Alleyne and P. Cawley, "The interaction of lamb waves with defects," *IEEE transactions on ultrasonics, ferroelectrics, and frequency control*, vol. 39, no. 3, pp. 381–397, 1992.

[149] V. Giurgiutiu, "Tuned lamb wave excitation and detection with piezoelectric wafer active sensors for structural health monitoring," *Journal of intelligent material systems and structures*, vol. 16, no. 4, pp. 291–305, 2005.

[150] M. Castaings and P. Cawley, "The generation, propagation, and detection of lamb waves in plates using air-coupled ultrasonic transducers," *The Journal of the Acoustical Society of America*, vol. 100, no. 5, pp. 3070–3077, 1996.

[151] T. Ghosh, T. Kundu, and P. Karpur, "Efficient use of lamb modes for detecting defects in large plates," *Ultrasonics*, vol. 36, no. 7, pp. 791–801, 1998.

[152] Z. Guo, J. Achenbach, and S. Krishnaswamy, "Emat generation and laser detection of single lamb wave modes," *Ultrasonics*, vol. 35, no. 6, pp. 423–429, 1997.

[153] P. D. Wilcox, M. J. Lowe, and P. Cawley, "The excitation and detection of lamb waves with planar coil electromagnetic acoustic transducers," *IEEE Transactions on ultrasonics, ferroelectrics, and frequency control*, vol. 52, no. 12, pp. 2370–2383, 2005.

[154] K. R. Whittemore Jr, S. N. Merchant, B. B. Poon, and J. J. Rosowski, "A normative study of tympanic membrane motion in humans using a laser doppler vibrometer (ldv)," *Hearing research*, vol. 187, no. 1-2, pp. 85–104, 2004.

[155] P. Kudela, M. Radzienski, P. Fiborek, and T. Wandowski, "Elastic constants identification of woven fabric reinforced composites by using guided wave dispersion curves and genetic algorithm," *Composite Structures*, p. 112569, 2020.

[156] C. B. Scruby and L. E. Drain, *Laser ultrasonics: techniques and applications*. Routledge, 2019.

[157] W. Staszewski, B. Lee, and R. Traynor, "Fatigue crack detection in metallic structures with lamb waves and 3d laser vibrometry," *Measurement Science and Technology*, vol. 18, no. 3, p. 727, 2007.

[158] H. Duflo, B. Morvan, and J.-L. Izbicki, "Interaction of lamb waves on bonded composite plates with defects," *Composite structures*, vol. 79, no. 2, pp. 229–233, 2007.

[159] T. Di Ianni, L. De Marchi, A. Perelli, and A. Marzani, "Compressive sensing of full wave field data for structural health monitoring applications," *IEEE transactions on ultrasonics, ferroelectrics, and frequency control*, vol. 62, no. 7, pp. 1373–1383, 2015.

[160] O. Mesnil, "Sparse reconstruction and analysis of guided wavefields for damage detection and quantification," Ph.D. dissertation, Georgia Institute of Technology, 2016.

[161] J. B. Harley and J. M. Moura, "Sparse recovery of the multimodal and dispersive characteristics of lamb waves," *The Journal of the Acoustical Society of America*, vol. 133, no. 5, pp. 2732–2745, 2013.

[162] ——, "Dispersion curve recovery with orthogonal matching pursuit," *The Journal of the Acoustical Society of America*, vol. 137, no. 1, pp. EL1–EL7, 2015.

[163] J. B. Harley, "Predictive guided wave models through sparse modal representations," *Proceedings of the IEEE*, vol. 104, no. 8, pp. 1604–1619, 2015.

[164] R. Monkhouse, P. Wilcox, and P. Cawley, "Flexible interdigital pvdf transducers for the generation of lamb waves in structures," *Ultrasonics*, vol. 35, no. 7, pp. 489–498, 1997.

[165] A. Bulletti, P. Giannelli, M. Calzolai, and L. Capineri, "An integrated acousto/ultrasonic structural health monitoring system for composite pressure vessels," *IEEE transactions on ultrasonics, ferroelectrics, and frequency control*, vol. 63, no. 6, pp. 864–873, 2016.

[166] B. Lin and V. Giurgiutiu, "Modeling and testing of pzt and pvdf piezoelectric wafer active sensors," *Smart Materials and Structures*, vol. 15, no. 4, p. 1085, 2006.

[167] L. Capineri and A. Bulletti, "Ultrasonic guided-waves sensors and integrated structural health monitoring systems for impact detection and localization: A review," *Sensors*, vol. 21, no. 9, p. 2929, 2021.

[168] V. Giurgiutiu and A. Cuc, "Embedded non-destructive evaluation for structural health monitoring, damage detection, and failure prevention," *Shock and Vibration Digest*, vol. 37, no. 2, p. 83, 2005.

[169] B. Xu and V. Giurgiutiu, "Single mode tuning effects on lamb wave time reversal with piezoelectric wafer active sensors for structural health monitoring," *Journal of Nondestructive Evaluation*, vol. 26, no. 2, pp. 123–134, 2007.

[170] V. Giurgiutiu, "Piezoelectric wafer active sensors for structural health monitoring of composite structures using tuned guided waves," *Journal of engineering materials and technology*, vol. 133, no. 4, 2011.

[171] M. Lemistre and D. Balageas, "Structural health monitoring system based on diffracted lamb wave analysis by multiresolution processing," *Smart materials and structures*, vol. 10, no. 3, p. 504, 2001.

[172] R. Monkhouse, P. Wilcox, M. Lowe, R. Dalton, and P. Cawley, "The rapid monitoring of structures using interdigital lamb wave transducers," *Smart Materials and Structures*, vol. 9, no. 3, p. 304, 2000.

[173] S. S. Kessler, S. M. Spearing, and C. Soutis, "Damage detection in composite materials using lamb wave methods," *Smart materials and structures*, vol. 11, no. 2, p. 269, 2002.

[174] S. Grondel, C. Paget, C. Delebarre, J. Assaad, and K. Levin, "Design of optimal configuration for generating a 0 lamb mode in a composite plate using piezoceramic transducers," *The Journal of the Acoustical Society of America*, vol. 112, no. 1, pp. 84–90, 2002.

[175] V. G. M. Annamdas and C. K. Soh, "Application of electromechanical impedance technique for engineering structures: review and future issues," *Journal of Intelligent material systems and structures*, vol. 21, no. 1, pp. 41–59, 2010.

[176] E. S. de Freitas and F. G. Baptista, "Experimental analysis of the feasibility of low-cost piezoelectric diaphragms in impedance-based shm applications," *Sensors and Actuators A: Physical*, vol. 238, pp. 220–228, 2016.

[177] V. Giurgiutiu and A. Zagrai, "Damage detection in thin plates and aerospace structures with the electro-mechanical impedance method," *Structural Health Monitoring*, vol. 4, no. 2, pp. 99–118, 2005.

[178] K. K. Tseng and L. Wang, "Smart piezoelectric transducers for in situ health monitoring of concrete," *Smart Materials and Structures*, vol. 13, no. 5, p. 1017, 2004.

[179] Y. Yang, Y. Y. Lim, and C. K. Soh, "Practical issues related to the application of the electromechanical impedance technique in the structural health monitoring of civil structures: I. experiment," *Smart Materials and Structures*, vol. 17, no. 3, p. 035008, 2008.

[180] S. R. Hamzeloo, M. Shamshirsaz, and S. M. Rezaei, "Damage detection on hollow cylinders by electro-mechanical impedance method: Experiments and finite element modeling," *Comptes Rendus Mécanique*, vol. 340, no. 9, pp. 668–677, 2012.

[181] K. K. Tseng and A. S. Naidu, "Non-parametric damage detection and characterization using smart piezoceramic material," *Smart Materials and Structures*, vol. 11, no. 3, p. 317, 2002.

[182] R. Tawie and H.-K. Lee, "Monitoring the strength development in concrete by emi sensing technique," *Construction and Building Materials*, vol. 24, no. 9, pp. 1746–1753, 2010.

[183] W. S. Na and J. Baek, "A review of the piezoelectric electromechanical impedance based structural health monitoring technique for engineering structures," *Sensors*, vol. 18, no. 5, p. 1307, 2018.

[184] A. N. Zagrai and V. Giurgiutiu, "Electro-mechanical impedance method for crack detection in thin plates," *Journal of Intelligent Material Systems and Structures*, vol. 12, no. 10, pp. 709–718, 2001.

[185] J. Zhang, C. Zhang, J. Xiao, and J. Jiang, "A pzt-based electromechanical impedance method for monitoring the soil freeze–thaw process," *Sensors*, vol. 19, no. 5, p. 1107, 2019.

[186] S. K. Bhalla and S. Moharana, "Modelling of piezo-bond structure system for structural health monitoring using emi technique," in *Key Engineering Materials*, vol. 569. Trans Tech Publ, 2013, pp. 1234–1240.

[187] Y. Y. Lim and C. K. Soh, "Damage detection and characterization using emi technique under varying axial load," *Smart Struct. Syst*, vol. 11, no. 4, pp. 349–364, 2013.

[188] L. De Marchi, A. Marzani, N. Speciale, and E. Viola, "A passive monitoring technique based on dispersion compensation to locate impacts in plate-like structures," *Smart Materials and Structures*, vol. 20, no. 3, p. 035021, 2011.

[189] L. Yu, G. Santoni-Bottai, B. Xu, W. Liu, and V. Giurgiutiu, "Piezoelectric wafer active sensors for in situ ultrasonic-guided wave shm," *Fatigue & Fracture of Engineering Materials & Structures*, vol. 31, no. 8, pp. 611–628, 2008.

[190] J. S. Crider II *et al.*, "Damage detection using lamb waves for structural health monitoring," 2007.

[191] C. Fendzi, J. Morel, M. Rebillat, M. Guskov, N. Mechbal, and G. Coffignal, "Optimal sensors placement to enhance damage detection in composite plates," 2014.

[192] H. K. Jung, G. Park, and J. Y. Jeon, "Development of an asymmetric sensor array with beamforming," in *Proceedings of the EWSHM-9th European Workshop on Structural Health Monitoring, Manchester, UK*, 2018, pp. 10–13.

[193] K. Heller, L. Jacobs, and J. Qu, "Characterization of adhesive bond properties using lamb waves," *NDT & E International*, vol. 33, no. 8, pp. 555–563, 2000.

[194] C. K. Liew and M. Veidt, "Pattern recognition of guided waves for damage evaluation in bars," *Pattern Recognition Letters*, vol. 30, no. 3, pp. 321–330, 2009.

[195] T. Hay, R. Royer, H. Gao, X. Zhao, and J. Rose, "A comparison of embedded sensor lamb wave ultrasonic tomography approaches for material loss detection," *Smart materials and structures*, vol. 15, no. 4, p. 946, 2006.

[196] C. Sbarufatti, G. Manson, and K. Worden, "A numerically-enhanced machine learning approach to damage diagnosis using a lamb wave sensing network," *Journal of Sound and Vibration*, vol. 333, no. 19, pp. 4499–4525, 2014.

[197] C. B. Scruby, "An introduction to acoustic emission," *Journal of Physics E: Scientific Instruments*, vol. 20, no. 8, p. 946, 1987.

[198] K. M. Holford, M. J. Eaton, J. J. Hensman, R. Pullin, S. L. Evans, N. Dervilis, and K. Worden, "A new methodology for automating acoustic emission detection of metallic fatigue fractures in highly demanding

aerospace environments: An overview," *Progress in Aerospace Sciences*, vol. 90, pp. 1–11, 2017.

[199] F. Ciampa and M. Meo, "A new algorithm for acoustic emission localization and flexural group velocity determination in anisotropic structures," *Composites Part A: Applied Science and Manufacturing*, vol. 41, no. 12, pp. 1777–1786, 2010.

[200] V. Salinas, Y. Vargas, J. Ruzzante, and L. Gaete, "Localization algorithm for acoustic emission," *Physics Procedia*, vol. 3, no. 1, pp. 863–871, 2010.

[201] C. Grosse, H. Reinhardt, and T. Dahm, "Localization and classification of fracture types in concrete with quantitative acoustic emission measurement techniques," *Ndt & E International*, vol. 30, no. 4, pp. 223–230, 1997.

[202] K. Salas and C. E. Cesnik, "Guided wave excitation by a clover transducer for structural health monitoring: theory and experiments," *Smart Materials and Structures*, vol. 18, no. 7, p. 075005, 2009.

[203] L. Cheng, H. Xin, R. M. Groves, and M. Veljkovic, "Acoustic emission source location using lamb wave propagation simulation and artificial neural network for i-shaped steel girder," *Construction and Building Materials*, vol. 273, p. 121706, 2021.

[204] E. D. Niri and S. Salamone, "A probabilistic framework for acoustic emission source localization in plate-like structures," *Smart Materials and Structures*, vol. 21, no. 3, p. 035009, 2012.

[205] F. Ciampa and M. Meo, "Acoustic emission source localization and velocity determination of the fundamental mode a0 using wavelet analysis

and a newton-based optimization technique," *Smart Materials and Structures*, vol. 19, no. 4, p. 045027, 2010.

[206] F. Zonzini, D. Bogomolov, T. Dhamija, N. Testoni, L. De Marchi, and A. Marzani, "Deep learning approaches for robust time of arrival estimation in acoustic emission monitoring," *Sensors*, vol. 22, no. 3, p. 1091, 2022.

[207] G. Giridhara, V. Rathod, S. Naik, D. R. Mahapatra, and S. Gopalakrishnan, "Rapid localization of damage using a circular sensor array and lamb wave based triangulation," *Mechanical Systems and Signal Processing*, vol. 24, no. 8, pp. 2929–2946, 2010.

[208] M. Harb and F. Yuan, "A rapid, fully non-contact, hybrid system for generating lamb wave dispersion curves," *Ultrasonics*, vol. 61, pp. 62–70, 2015.

[209] H. Chen, Z. Liu, Y. Gong, B. Wu, and C. He, "Evolutionary strategy-based location algorithm for high-resolution lamb wave defect detection with sparse array," *IEEE Transactions on Ultrasonics, Ferroelectrics, and Frequency Control*, vol. 68, no. 6, pp. 2277–2293, 2021.

[210] T. Kundu, S. Das, and K. V. Jata, "Point of impact prediction in isotropic and anisotropic plates from the acoustic emission data," *The Journal of the Acoustical Society of America*, vol. 122, no. 4, pp. 2057–2066, 2007.

[211] ——, "Detection of the point of impact on a stiffened plate by the acoustic emission technique," *Smart Materials and Structures*, vol. 18, no. 3, p. 035006, 2009.

[212] S. Salamone, I. Bartoli, P. Di Leo, F. Lanza Di Scala, A. Ajovalasit, L. D'Acquisto, J. Rhymer, and H. Kim, "High-velocity impact location on

aircraft panels using macro-fiber composite piezoelectric rosettes," *Journal of Intelligent Material Systems and Structures*, vol. 21, no. 9, pp. 887–896, 2010.

[213] J. Park, S. Ha, and F.-K. Chang, "Monitoring impact events using a system-identification method," *AIAA journal*, vol. 47, no. 9, pp. 2011–2021, 2009.

[214] Y.-T. Chan and K. Ho, "A simple and efficient estimator for hyperbolic location," *IEEE Transactions on signal processing*, vol. 42, no. 8, pp. 1905–1915, 1994.

[215] A. Urruela, J. Sala, and J. Riba, "Average performance analysis of circular and hyperbolic geolocation," *IEEE Transactions on Vehicular Technology*, vol. 55, no. 1, pp. 52–66, 2006.

[216] L. Capineri, A. Bulletti, and E. Marino Merlo, "Multichannel real-time electronics platform for the estimation of the error in impact localization with different piezoelectric sensor densities," *Applied Sciences*, vol. 11, no. 9, p. 4027, 2021.

[217] E. Marino-Merlo, A. Bulletti, P. Giannelli, M. Calzolai, and L. Capineri, "Analysis of errors in the estimation of impact positions in plate-like structure through the triangulation formula by piezoelectric sensors monitoring," *Sensors*, vol. 18, no. 10, p. 3426, 2018.

[218] F. Schäfer and R. Janovsky, "Impact sensor network for detection of hypervelocity impacts on spacecraft," *Acta Astronautica*, vol. 61, no. 10, pp. 901–911, 2007.

[219] M. Tracy and F.-K. Chang, "Identifying impacts in composite plates with piezoelectric strain sensors, part ii: Experiment," *Journal of intelligent material systems and structures*, vol. 9, no. 11, pp. 929–937, 1998.

[220] R. Seydel and F.-K. Chang, "Impact identification of stiffened composite panels: I. system development," *Smart materials and structures*, vol. 10, no. 2, p. 354, 2001.

[221] T. Kosel, I. Grabec, and P. Mužič, "Location of acoustic emission sources generated by air flow," *Ultrasonics*, vol. 38, no. 1-8, pp. 824–826, 2000.

[222] P. White, "Cross correlation in structural systems: dispersion and nondispersion waves," *The Journal of the Acoustical Society of America*, vol. 45, no. 5, pp. 1118–1128, 1969.

[223] M. Azaria and D. Hertz, "Time delay estimation by generalized cross correlation methods," *IEEE Transactions on Acoustics, Speech, and Signal Processing*, vol. 32, no. 2, pp. 280–285, 1984.

[224] A. Perelli, L. De Marchi, A. Marzani, and N. Speciale, "Acoustic emission localization in plates with dispersion and reverberations using sparse pzt sensors in passive mode," *Smart Materials and Structures*, vol. 21, no. 2, p. 025010, 2012.

[225] L. De Marchi, A. Marzani, S. Caporale, and N. Speciale, "Ultrasonic guided-waves characterization with warped frequency transforms," *IEEE transactions on ultrasonics, ferroelectrics, and frequency control*, vol. 56, no. 10, pp. 2232–2240, 2009.

[226] Q. Xu, "A comparison study of extreme learning machine and least squares support vector machine for structural impact localization," *Mathematical Problems in Engineering*, vol. 2014, 2014.

[227] L. Morse, Z. S. Khodaei, and M. Aliabadi, "Reliability based impact localization in composite panels using bayesian updating and the kalman filter," *Mechanical Systems and Signal Processing*, vol. 99, pp. 107–128, 2018.

[228] P. Coverley and W. Staszewski, "Impact damage location in composite structures using optimized sensor triangulation procedure," *Smart materials and structures*, vol. 12, no. 5, p. 795, 2003.

[229] H. M. Matt and F. L. di Scalea, "Macro-fiber composite piezoelectric rosettes for acoustic source location in complex structures," *Smart Materials and Structures*, vol. 16, no. 4, p. 1489, 2007.

[230] M. Romanoni, S. Gonella, N. Apetre, and M. Ruzzene, "Two-dimensional periodic actuators for frequency-based beam steering," *Smart materials and structures*, vol. 18, no. 12, p. 125023, 2009.

[231] E. Baravelli, M. Senesi, M. Ruzzene, L. De Marchi, and N. Speciale, "Double-channel, frequency-steered acoustic transducer with 2-d imaging capabilities," *IEEE transactions on ultrasonics, ferroelectrics, and frequency control*, vol. 58, no. 7, pp. 1430–1441, 2011.

[232] E. Baravelli, M. Senesi, M. Ruzzene, and L. De Marchi, "Fabrication and characterization of a wavenumber-spiral frequency-steerable acoustic transducer for source localization in plate structures," *IEEE Transactions on Instrumentation and Measurement*, vol. 62, no. 8, pp. 2197–2204, 2013.

[233] L. De Marchi, N. Testoni, and A. Marzani, "Spiral-shaped piezoelectric sensors for lamb waves direction of arrival (doa) estimation," *Smart Materials and Structures*, vol. 27, no. 4, p. 045016, 2018.

[234] L. D. Marchi, M. Dibiase, and N. Testoni, "Piezoelectric sensors for lamb waves direction of arrival (doa) estimation," in *Multidisciplinary Digital Publishing Institute Proceedings*, vol. 2, no. 13, 2018, p. 806.

[235] M. Dibiase, M. Mohammadgholiha, and L. De Marchi, "Optimal array design and directive sensors for guided waves doa estimation," *Sensors*, vol. 22, no. 3, p. 780, 2022.

[236] T. Kundu, H. Nakatani, and N. Takeda, "Acoustic source localization in anisotropic plates," *Ultrasonics*, vol. 52, no. 6, pp. 740–746, 2012.

[237] A. Garofalo, N. Testoni, A. Marzani, and L. De Marchi, "Multiresolution wavelet analysis to estimate lamb waves direction of arrival in passive monitoring techniques," in *2017 IEEE Workshop on Environmental, Energy, and Structural Monitoring Systems (EESMS)*. IEEE, 2017, pp. 1–6.

[238] ——, "Wavelet-based lamb waves direction of arrival estimation in passive monitoring techniques," in *2016 IEEE International Ultrasonics Symposium (IUS)*. IEEE, 2016, pp. 1–4.

[239] M. Marsden, "Cubic spline interpolation of continuous functions," *Journal of Approximation Theory*, vol. 10, no. 2, pp. 103–111, 1974.

[240] M. Mitra and S. Gopalakrishnan, "Guided wave based structural health monitoring: A review," *Smart Materials and Structures*, vol. 25, no. 5, p. 053001, 2016.

[241] M. Tabatabaeipour, J. Hettler, S. Delrue, and K. Van Den Abeele, "Reconstruction algorithm for probabilistic inspection of damage (rapid) in composites," in *Proc. 11th Eur. Conf. Non-Destructive Test.(ECNDT)*, 2014, pp. 1–8.

[242] S. Wang, W. Wu, Y. Shen, Y. Liu, and S. Jiang, "Influence of the pzt sensor array configuration on lamb wave tomography imaging with the rapid algorithm for hole and crack detection," *Sensors*, vol. 20, no. 3, p. 860, 2020.

[243] N. Quaegebeur, P. Ostiguy, and P. Masson, "Hybrid empirical/analytical modeling of guided wave generation by circular piezoceramics," *Smart Materials and Structures*, vol. 24, no. 3, p. 035003, 2015.

[244] P.-C. Ostiguy, N. Quaegebeur, and P. Masson, "Comparison of model-based damage imaging techniques for transversely isotropic composites," *Structural Health Monitoring*, vol. 16, no. 4, pp. 428–443, 2017.

[245] H. Gao, Y. Shi, and J. L. Rose, "Guided wave tomography on an aircraft wing with leave in place sensors," in *AIP Conference Proceedings*, vol. 760, no. 1. American Institute of Physics, 2005, pp. 1788–1794.

[246] G. Azuara, E. Barrera, M. Ruiz, and D. Bekas, "Damage detection and characterization in composites using a geometric modification of the rapid algorithm," *IEEE Sensors Journal*, vol. 20, no. 4, pp. 2084–2093, 2019.

[247] M. Dziendzikowski, K. Dragan, and A. Katunin, "Localizing impact damage of composite structures with modified rapid algorithm and non-circular pzt arrays," *Archives of Civil and Mechanical Engineering*, vol. 17, no. 1, pp. 178–187, 2017.

[248] R. Neubeck, C. Kexel, and J. Moll, "Matrix techniques for lamb-wave damage imaging in metal plates," *Smart Materials and Structures*, vol. 29, no. 11, p. 117003, oct 2020. [Online]. Available: https://doi.org/10.1088/1361-665x/abba6d

[249] Z. Sharif-Khodaei and M. Aliabadi, "Assessment of delay-and-sum algorithms for damage detection in aluminium and composite plates," *Smart materials and structures*, vol. 23, no. 7, p. 075007, 2014.

[250] V. Perrot, M. Polichetti, F. Varray, and D. Garcia, "So you think you can das? a viewpoint on delay-and-sum beamforming," *Ultrasonics*, vol. 111, p. 106309, 2021.

[251] G. C. Luppescu, A. J. Dawson, and J. E. Michaels, "Dispersive matched filtering of ultrasonic guided waves for improved sparse array damage localization," in *AIP Conference Proceedings*, vol. 1706, no. 1. AIP Publishing LLC, 2016, p. 030008.

[252] J. Moll, L. De Marchi, C. Kexel, and A. Marzani, "High resolution defect imaging in guided waves inspections by dispersion compensation and nonlinear data fusion," *Acta Acustica united with Acustica*, vol. 103, no. 6, pp. 941–949, 2017.

[253] F. Le Bourdais, O. Mesnil, and O. d'Almeida, "Machine-learning based temperature compensation for guided wave imaging in structural health monitoring," in *Proceedings of the 11th International Symposium on NDT in aerospace, Paris-Saclay*, 2019.

[254] Y. Ren, L. Qiu, S. Yuan, and F. Fang, "Gaussian mixture model and delay-and-sum based 4d imaging of damage in aircraft composite structures under time-varying conditions," *Mechanical Systems and Signal Processing*, vol. 135, p. 106390, 2020. [Online]. Available: https://www.sciencedirect.com/science/article/pii/S0888327019306119

[255] M. Salmanpour, Z. Sharif Khodaei, and M. Aliabadi, "Transducer placement optimisation scheme for a delay and sum damage detection algo-

rithm," *Structural Control and Health Monitoring*, vol. 24, no. 4, p. e1898, 2017.

[256] C. Xu, Z. Yang, S. Tian, and X. Chen, "Lamb wave inspection for composite laminates using a combined method of sparse reconstruction and delay-and-sum," *Composite Structures*, vol. 223, p. 110973, 2019. [Online]. Available: https://www.sciencedirect.com/science/article/pii/S0263822318338522

[257] G. Lu, Y. Li, T. Wang, H. Xiao, L. Huo, and G. Song, "A multi-delay-and-sum imaging algorithm for damage detection using piezoceramic transducers," *Journal of Intelligent Material Systems and Structures*, vol. 28, no. 9, pp. 1150–1159, 2017. [Online]. Available: https://doi.org/10.1177/1045389X16666184

[258] J. S. Hall, P. McKeon, L. Satyanarayan, J. E. Michaels, N. F. Declercq, and Y. H. Berthelot, "Minimum variance guided wave imaging in a quasi-isotropic composite plate," *Smart Materials and Structures*, vol. 20, no. 2, p. 025013, 2011.

[259] E. Carcreff, N. Laroche, D. Braconnier, A. Duclos, and S. Bourguignon, "Improvement of the total focusing method using an inverse problem approach," in *2017 IEEE International Ultrasonics Symposium (IUS)*, 2017, pp. 1–4.

[260] H. Zhang, J. Hua, F. Gao, and J. Lin, "Efficient lamb-wave based damage imaging using multiple sparse bayesian learning in composite laminates," *NDT E International*, vol. 116, p. 102277, 2020. [Online]. Available: https://www.sciencedirect.com/science/article/pii/S0963869520300050

[261] H. B. Lim, N. T. T. Nhung, E.-P. Li, and N. D. Thang, "Confocal microwave imaging for breast cancer detection: Delay-multiply-and-sum image reconstruction algorithm," *IEEE Transactions on Biomedical Engineering*, vol. 55, no. 6, pp. 1697–1704, 2008.

[262] G. Matrone, A. S. Savoia, G. Caliano, and G. Magenes, "The delay multiply and sum beamforming algorithm in ultrasound b-mode medical imaging," *IEEE transactions on medical imaging*, vol. 34, no. 4, pp. 940–949, 2014.

[263] J. Park, S. Jeon, J. Meng, L. Song, J. S. Lee, and C. Kim, "Delay-multiply-and-sum-based synthetic aperture focusing in photoacoustic microscopy," *Journal of biomedical optics*, vol. 21, no. 3, p. 036010, 2016.

[264] M. Mozaffarzadeh, M. Sadeghi, A. Mahloojifar, and M. Orooji, "Double-stage delay multiply and sum beamforming algorithm applied to ultrasound medical imaging," *Ultrasound in medicine & biology*, vol. 44, no. 3, pp. 677–686, 2018.

[265] M. Mozaffarzadeh, A. Mahloojifar, M. Orooji, S. Adabi, and M. Nasiriavanaki, "Double-stage delay multiply and sum beamforming algorithm: Application to linear-array photoacoustic imaging," *IEEE Transactions on Biomedical Engineering*, vol. 65, no. 1, pp. 31–42, 2017.

[266] J. Moll, R. Schulte, B. Hartmann, C. Fritzen, and O. Nelles, "Multi-site damage localization in anisotropic plate-like structures using an active guided wave structural health monitoring system," *Smart Materials and Structures*, vol. 19, no. 4, p. 045022, 2010.

[267] J. E. Michaels, "Detection, localization and characterization of damage in plates with an in situ array of spatially distributed ultrasonic sensors," *Smart Materials and Structures*, vol. 17, no. 3, p. 035035, 2008.

[268] H. Zhang, J. Hua, F. Gao, and J. Lin, "Efficient lamb-wave based damage imaging using multiple sparse bayesian learning in composite laminates," *NDT & E International*, vol. 116, p. 102277, 2020.

[269] J. Chen, Z. Li, and K. Gong, "Nondestructive testing method based on lamb waves for localization and extent of damage," *Acta Mechanica Solida Sinica*, vol. 30, no. 1, pp. 65–74, 2017.

[270] L. Wang and F. Yuan, "Group velocity and characteristic wave curves of lamb waves in composites: Modeling and experiments," *Composites science and technology*, vol. 67, no. 7-8, pp. 1370–1384, 2007.

[271] C. Chang and F. Yuan, "Dispersion curve extraction of lamb waves in metallic plates by matrix pencil method," in *Sensors and Smart Structures Technologies for Civil, Mechanical, and Aerospace Systems 2017*, vol. 10168. International Society for Optics and Photonics, 2017, p. 1016807.

[272] F. Schöpfer, F. Binder, A. Wöstehoff, T. Schuster, S. von Ende, S. Föll, and R. Lammering, "Accurate determination of dispersion curves of guided waves in plates by applying the matrix pencil method to laser vibrometer measurement data," *CEAS Aeronautical Journal*, vol. 4, no. 1, pp. 61–68, 2013.

[273] A. Nokhbatolfoghahai, H. Navazi, and R. Groves, "Using the hybrid das-sr method for damage localization in composite plates," *Composite Structures*, vol. 247, p. 112420, 2020.

[274] G. Konstantinidis, B. W. Drinkwater, and P. D. Wilcox, "The temperature stability of guided wave structural health monitoring systems," *Smart Materials and Structures*, vol. 15, no. 4, p. 967, 2006.

[275] A. J. Croxford, J. Moll, P. D. Wilcox, and J. E. Michaels, "Efficient temperature compensation strategies for guided wave structural health monitoring," *Ultrasonics*, vol. 50, no. 4-5, pp. 517–528, 2010.

[276] M. S. Salmanpour, Z. Sharif Khodaei, and M. H. Aliabadi, "Impact damage localisation with piezoelectric sensors under operational and environmental conditions," *Sensors*, vol. 17, no. 5, p. 1178, 2017.

[277] M. Salmanpour, Z. Sharif Khodaei, and M. Aliabadi, "Guided wave temperature correction methods in structural health monitoring," *Journal of Intelligent Material Systems and Structures*, vol. 28, no. 5, pp. 604–618, 2017.

[278] A. Nokhbatolfoghahai, H. Navazi, and R. Groves, "Evaluation of the sparse reconstruction and the delay-and-sum damage imaging methods for structural health monitoring under different environmental and operational conditions," *Measurement*, vol. 169, p. 108495, 2021.

[279] S. Fu, L. Shi, Y. Zhou, and J. Cai, "Dispersion compensation in lamb wave defect detection with step-pulse excitation and warped frequency transform," *IEEE transactions on ultrasonics, ferroelectrics, and frequency control*, vol. 61, no. 12, pp. 2075–2088, 2014.

[280] J. S. Hall and J. E. Michaels, "Adaptive dispersion compensation for guided wave imaging," in *AIP Conference Proceedings*, vol. 1430, no. 1. American Institute of Physics, 2012, pp. 623–630.

[281] H. Jia, H. Liu, Z. Zhang, F. Dai, Y. Liu, and J. Leng, "A baseline-free approach of locating defect based on mode conversion and the reciprocity principle of lamb waves," *Ultrasonics*, vol. 102, p. 106063, 2020.

[282] J. E. Michaels and T. E. Michaels, "Enhanced differential methods for guided wave phased array imaging using spatially distributed piezoelectric transducers," in *AIP conference proceedings*, vol. 820, no. 1. American Institute of Physics, 2006, pp. 837–844.

[283] M. A. Aldhaeebi, K. Alzoubi, T. S. Almoneef, S. M. Bamatraf, H. Attia, and O. M. Ramahi, "Review of microwaves techniques for breast cancer detection," *Sensors*, vol. 20, no. 8, p. 2390, 2020.

[284] J. Moll, T. Kelly, D. Byrne, M. Sarafianou, V. Krozer, and I. Craddock, "Microwave Radar Imaging of Heterogeneous Breast Tissue Integrating A-Priori Information," *International Journal of Biomedical Imaging*, pp. Article ID 943 549, 10 pages, 2014.

[285] M. Elahi, D. O'Loughlin, B. Lavoie, M. Glavin, E. Jones, E. Fear, and M. O'Halloran, "Evaluation of Image Reconstruction Algorithms for Confocal Microwave Imaging: Application to Patient Data," *Sensors*, vol. 18, no. 6, p. 1678, May 2018.

[286] J. Moll and V. Krozer, "Time-Difference-of-Arrival Imaging for Ultra-Wideband Microwave Mammography," in *7th European Conference on Antennas and Propagation*, Gothenburg, Sweden, 2013, pp. 2595–2599.

[287] M. O'Halloran, M. Glavin, and E. Jones, "Channel-ranked beamformer for the early detection of breast cancer," *Progress In Electromagnetics Research*, vol. 103, pp. 153–168, 2010.

[288] M. T. Islam, M. T. Islam, M. Samsuzzaman, S. Kibria, and M. E. H. Chowdhury, "Microwave Breast Imaging Using Compressed Sensing Approach of Iteratively Corrected Delay Multiply and Sum Beamforming," *Diagnostics*, vol. 11, no. 3, p. 470, Mar. 2021.

[289] C. Kexel, J. Moll, M. Kuhnt, F. Wiegandt, and V. Krozer, "Compressed Sensing for Three-Dimensional Microwave Breast Cancer Imaging," in *8th European Conference on Antennas and Propagation*, 2014, pp. 1634–1638.

[290] K. M. Kempski, M. T. Graham, M. R. Gubbi, T. Palmer, and M. A. L. Bell, "Application of the generalized contrast-to-noise ratio to assess photoacoustic image quality," *Biomedical Optics Express*, vol. 11, no. 7, pp. 3684–3698, 2020.

[291] S. Buske, S. Gutjahr, and C. Sick, "Fresnel volume migration of single-component seismic data," *Geophysics*, vol. 74, no. 6, pp. WCA47–WCA55, 2009.

[292] J. Spetzler and R. Snieder, "The fresnel volume and transmitted waves," *Geophysics*, vol. 69, no. 3, pp. 653–663, 2004.

[293] N. Hirabayashi, "Reflector imaging using trial reflector and crosscorrelation: Application to fracture imaging for sonic data," *Geophysics*, vol. 81, no. 6, pp. S433–S446, 2016.

[294] C. Hu and P. L. Stoffa, "Slowness-driven gaussian-beam prestack depth migration for low-fold seismic data," *Geophysics*, vol. 74, no. 6, pp. WCA35–WCA45, 2009.

[295] R. NEUBECK, B. WEIHNACHT, and B. FRANKENSTEIN, "Mode–selective imaging procedures of acoustic ultrasonic data on hollow cylinder geometries for structural-health-monitoring," 2014.

[296] P. Brémaud, *Mathematical principles of signal processing: Fourier and wavelet analysis*. Springer, 2002.

[297] A. Rodriguez-Molares, O. M. H. Rindal, J. D'hooge, S.-E. Måsøy, A. Austeng, M. A. L. Bell, and H. Torp, "The generalized contrast-to-noise ratio: a formal definition for lesion detectability," *IEEE Transactions on Ultrasonics, Ferroelectrics, and Frequency Control*, vol. 67, no. 4, pp. 745–759, 2019.

[298] A. Rodriguez-Molares, O. M. H. Rindal, J. D'hooge, S.-E. Måsøy, A. Austeng, and H. Torp, "The generalized contrast-to-noise ratio," in *2018 IEEE International Ultrasonics Symposium (IUS)*. IEEE, 2018, pp. 1–4.

[299] G. Matrone, A. Ramalli, J. D'hooge, P. Tortoli, and G. Magenes, "A comparison of coherence-based beamforming techniques in high-frame-rate ultrasound imaging with multi-line transmission," *IEEE transactions on ultrasonics, ferroelectrics, and frequency control*, vol. 67, no. 2, pp. 329–340, 2019.

[300] M. Patterson and F. Foster, "The improvement and quantitative assessment of b-mode images produced by an annular array/cone hybrid," *Ultrasonic Imaging*, vol. 5, no. 3, pp. 195–213, 1983.

[301] O. M. H. Rindal, A. Austeng, A. Fatemi, and A. Rodriguez-Molares, "The effect of dynamic range alterations in the estimation of contrast," *IEEE transactions on ultrasonics, ferroelectrics, and frequency control*, vol. 66, no. 7, pp. 1198–1208, 2019.

[302] M. R. Gubbi and M. A. L. Bell, "Theoretical predictions of the generalized contrast-to-noise ratio for photoacoustic images," in *2020 IEEE International Ultrasonics Symposium (IUS)*. IEEE, 2020, pp. 1–4.

[303] A. Marzani, N. Testoni, L. De Marchi, M. Messina, E. Monaco, and A. Apicella, "An open database for benchmarking guided waves structural health monitoring algorithms on a composite full-scale outer wing demonstrator," *Structural Health Monitoring*, p. 1475921719889029, 2019.

[304] L. Zeng, L. Huang, X. Cao, and F. Gao, "Determination of lamb wave phase velocity dispersion using time–frequency analysis," *Smart Materials and Structures*, vol. 28, no. 11, p. 115029, 2019.

[305] K. Xu, J.-G. Minonzio, D. Ta, B. Hu, W. Wang, and P. Laugier, "Sparse svd method for high-resolution extraction of the dispersion curves of ultrasonic guided waves," *IEEE transactions on ultrasonics, ferroelectrics, and frequency control*, vol. 63, no. 10, pp. 1514–1524, 2016.

[306] P. Zabbal, G. Ribay, B. Chapuis, and J. Jumel, "Multichannel multiple signal classification for dispersion curves extraction of ultrasonic guided waves," *The Journal of the Acoustical Society of America*, vol. 143, no. 2, pp. EL87–EL92, 2018.

[307] B. Hosten and M. Castaings, "Finite elements methods for modeling the guided waves propagation in structures with weak interfaces," *The Journal of the Acoustical Society of America*, vol. 117, no. 3, pp. 1108–1113, 2005.

[308] T. Hayashi and D. Inoue, "Calculation of leaky lamb waves with a semi-analytical finite element method," *Ultrasonics*, vol. 54, no. 6, pp. 1460–1469, 2014.

[309] J. Li, Z. S. Khodaei, and M. Aliabadi, "Boundary element modelling of ultrasonic lamb waves for structural health monitoring," *Smart Materials and Structures*, vol. 29, no. 10, p. 105030, 2020.

[310] Y. Cho and J. L. Rose, "A boundary element solution for a mode conversion study on the edge reflection of lamb waves," *The Journal of the Acoustical Society of America*, vol. 99, no. 4, pp. 2097–2109, 1996.

[311] P. Kudela, A. Żak, M. Krawczuk, and W. Ostachowicz, "Modelling of wave propagation in composite plates using the time domain spectral element method," *Journal of Sound and Vibration*, vol. 302, no. 4-5, pp. 728–745, 2007.

[312] A. Kamal and V. Giurgiutiu, "Stiffness transfer matrix method (stmm) for stable dispersion curves solution in anisotropic composites," in *Health Monitoring of Structural and Biological Systems 2014*, vol. 9064. International Society for Optics and Photonics, 2014, p. 906410.

[313] B. Pavlakovic, M. Lowe, D. Alleyne, and P. Cawley, "Disperse: A general purpose program for creating dispersion curves," in *Review of progress in quantitative nondestructive evaluation*. Springer, 1997, pp. 185–192.

[314] P. Castellini, M. Martarelli, and E. P. Tomasini, "Laser doppler vibrometry: Development of advanced solutions answering to technology's needs," *Mechanical systems and signal processing*, vol. 20, no. 6, pp. 1265–1285, 2006.

[315] E. D. Swenson, H. Sohn, S. E. Olson, and M. P. Desimio, "A comparison of 1d and 3d laser vibrometry measurements of lamb waves," in *Health Monitoring of Structural and Biological Systems 2010*, vol. 7650. International Society for Optics and Photonics, 2010, p. 765003.

[316] L. Mallet, B. Lee, W. Staszewski, and F. Scarpa, "Structural health monitoring using scanning laser vibrometry: Ii. lamb waves for damage detection," *Smart Materials and Structures*, vol. 13, no. 2, p. 261, 2004.

[317] J.-H. Lee and S.-J. Lee, "Application of laser-generated guided wave for evaluation of corrosion in carbon steel pipe," *Ndt & E International*, vol. 42, no. 3, pp. 222–227, 2009.

[318] R. Longo, S. Vanlanduit, J. Vanherzeele, and P. Guillaume, "A method for crack sizing using laser doppler vibrometer measurements of surface acoustic waves," *Ultrasonics*, vol. 50, no. 1, pp. 76–80, 2010.

[319] L. P. Scudder, D. A. Hutchins, and N. Guo, "Laser-generated ultrasonic guided waves in fiber-reinforced plates-theory and experiment," *IEEE transactions on ultrasonics, ferroelectrics, and frequency control*, vol. 43, no. 5, pp. 870–880, 1996.

[320] M. Harb and F. Yuan, "Non-contact ultrasonic technique for lamb wave characterization in composite plates," *Ultrasonics*, vol. 64, pp. 162–169, 2016.

[321] H. Sohn, D. Dutta, J. Yang, M. DeSimio, S. Olson, and E. Swenson, "Automated detection of delamination and disbond from wavefield images obtained using a scanning laser vibrometer," *Smart Materials and Structures*, vol. 20, no. 4, p. 045017, 2011.

[322] M. Ruzzene, "Frequency-wavenumber domain filtering for improved damage visualization," in *Ultrasonic and Advanced Methods for Nondestructive Testing and Material Characterization*. World Scientific, 2007, pp. 591–611.

[323] O. Mesnil, C. A. Leckey, and M. Ruzzene, "Instantaneous and local wavenumber estimations for damage quantification in composites," *Structural Health Monitoring*, vol. 14, no. 3, pp. 193–204, 2015.

[324] V. V. S. Malladi, M. I. Albakri, M. Krishnan, S. Gugercin, and P. A. Tarazaga, "Estimating experimental dispersion curves from steady-state frequency response measurements," *Mechanical Systems and Signal Processing*, vol. 164, p. 108218, 2022.

[325] Z. Ma and L. Yu, "Noncontact/remote material characterization using ultrasonic guided wave methods," in *Smart Materials, Adaptive Structures and Intelligent Systems*, vol. 84027. American Society of Mechanical Engineers, 2020, p. V001T05A006.

[326] S. Rajagopalan, J. M. Aller, J. A. Restrepo, T. G. Habetler, and R. G. Harley, "Analytic-wavelet-ridge-based detection of dynamic eccentricity in brushless direct current (bldc) motors functioning under dynamic operating conditions," *IEEE Transactions on Industrial Electronics*, vol. 54, no. 3, pp. 1410–1419, 2007.

[327] J. Zhong and Y. Huang, "Time-frequency representation based on an adaptive short-time fourier transform," *IEEE Transactions on Signal Processing*, vol. 58, no. 10, pp. 5118–5128, 2010.

[328] B. Hernandez Crespo, C. R. Courtney, and B. Engineer, "Calculation of guided wave dispersion characteristics using a three-transducer measurement system," *Applied Sciences*, vol. 8, no. 8, p. 1253, 2018.

[329] Z. Tian and L. Yu, "Lamb wave frequency–wavenumber analysis and decomposition," *Journal of Intelligent Material Systems and Structures*, vol. 25, no. 9, pp. 1107–1123, 2014.

[330] P. Kudela, M. Radzieński, and W. Ostachowicz, "Identification of cracks in thin-walled structures by means of wavenumber filtering," *Mechanical Systems and Signal Processing*, vol. 50, pp. 456–466, 2015.

[331] G. Sha, M. Radzienski, R. Soman, T. Wandowski, M. Cao, and W. Ostachowicz, "Delamination imaging in laminated composite plates using 2d wavelet analysis of guided wavefields," *Smart Materials and Structures*, vol. 30, no. 1, p. 015001, 2020.

[332] L. De Marchi, E. Baravelli, M. Ruzzene, N. Speciale, and G. Masetti, "Guided wave expansion in warped curvelet frames," *IEEE transactions on ultrasonics, ferroelectrics, and frequency control*, vol. 59, no. 5, pp. 949–957, 2012.

[333] K. Xu, D. Ta, and W. Wang, "Multiridge-based analysis for separating individual modes from multimodal guided wave signals in long bones," *IEEE transactions on ultrasonics, ferroelectrics, and frequency control*, vol. 57, no. 11, pp. 2480–2490, 2010.

[334] Z. Ma and L. Yu, "Lamb wave imaging with actuator network for damage quantification in aluminum plate structures," *Journal of Intelligent Material Systems and Structures*, vol. 32, no. 2, pp. 182–195, 2021.

[335] S. Sabeti, C. A. Leckey, L. De Marchi, and J. B. Harley, "Sparse wavenumber recovery and prediction of anisotropic guided waves in composites: A comparative study," *IEEE transactions on ultrasonics, ferroelectrics, and frequency control*, vol. 66, no. 8, pp. 1352–1363, 2019.

[336] S. Sabeti and J. B. Harley, "Spatio-temporal undersampling: Recovering ultrasonic guided wavefields from incomplete data with compressive

sensing," *Mechanical Systems and Signal Processing*, vol. 140, p. 106694, 2020.

[337] C. Li, C. Xu, C. Gui, and M. D. Fox, "Distance regularized level set evolution and its application to image segmentation," *IEEE transactions on image processing*, vol. 19, no. 12, pp. 3243–3254, 2010.

[338] G. Aubert and P. Kornprobst, *Mathematical problems in image processing: partial differential equations and the calculus of variations*. Springer Science & Business Media, 2006, vol. 147.

[339] E. B. Flynn, "Embedded multi-tone ultrasonic excitation and continuous-scanning laser doppler vibrometry for rapid and remote imaging of structural defects," in *EWSHM-7th European workshop on structural health monitoring*, 2014.

[340] O. Mesnil, H. Yan, M. Ruzzene, K. Paynabar, and J. Shi, "Fast wavenumber measurement for accurate and automatic location and quantification of defect in composite," *Structural Health Monitoring*, vol. 15, no. 2, pp. 223–234, 2016.

[341] J. M. Kilpatrick and V. B. Markov, "Full-field laser vibrometer for instantaneous vibration measurement and non-destructive inspection," in *Key Engineering Materials*, vol. 437. Trans Tech Publ, 2010, pp. 407–411.

[342] Z. Tian, L. Yu, and C. Leckey, "Rapid guided wave delamination detection and quantification in composites using global-local sensing," *Smart Materials and Structures*, vol. 25, no. 8, p. 085042, 2016.

[343] S. Qaisar, R. M. Bilal, W. Iqbal, M. Naureen, and S. Lee, "Compressive sensing: From theory to applications, a survey," *Journal of Communications and networks*, vol. 15, no. 5, pp. 443–456, 2013.

[344] Y. K. Esfandabadi, L. De Marchi, N. Testoni, A. Marzani, and G. Masetti, "Full wavefield analysis and damage imaging through compressive sensing in lamb wave inspections," *IEEE transactions on ultrasonics, ferroelectrics, and frequency control*, vol. 65, no. 2, pp. 269–280, 2017.

[345] Y. K. ESFANDABADI, M. BILODEAU, P. MASSON, and L. DE MARCHI, "Ultrasonic guided wave dataset for super-resolution reconstruction of images from compressed wavefield acquisition," *Structural Health Monitoring 2019*, 2019.

[346] Y. Keshmiri Esfandabadi, M. Bilodeau, P. Masson, and L. De Marchi, "Deep learning for enhancing wavefield image quality in fast non-contact inspections," *Structural Health Monitoring*, vol. 19, no. 4, pp. 1003–1016, 2020.

[347] S. Sabeti and J. B. Harley, "Two-dimensional sparse wavenumber recovery for guided wavefields," in *AIP Conference Proceedings*, vol. 1949, no. 1. AIP Publishing LLC, 2018, p. 230003.

[348] J. A. Tropp and A. C. Gilbert, "Signal recovery from random measurements via orthogonal matching pursuit," *IEEE Transactions on information theory*, vol. 53, no. 12, pp. 4655–4666, 2007.

[349] Y. Fang, J. Wu, and B. Huang, "2d sparse signal recovery via 2d orthogonal matching pursuit," *Science China Information Sciences*, vol. 55, no. 4, pp. 889–897, 2012.

[350] P. Kudela, M. Radzienski, P. Fiborek, and T. Wandowski, "Elastic constants identification of fibre-reinforced composites by using guided wave dispersion curves and genetic algorithm for improved simulations," *Composite Structures*, vol. 272, p. 114178, 2021.

[351] M. Golub, J. Moll, T. Ebert, E. Glushkov, N. Glushkova, C. Fritzen, and O. Nelles, "Experimentally based modeling of non-axisymmetric lamb wave propagation from circular pzts," in *ECCOMAS Thematic Conference on Smart Structures and Materials*, 2011, pp. 486–492.

[352] H. Sohn, C. R. Farrar, F. M. Hemez, D. D. Shunk, D. W. Stinemates, B. R. Nadler, and J. J. Czarnecki, "A review of structural health monitoring literature: 1996–2001," *Los Alamos National Laboratory, USA*, vol. 1, 2003.

[353] E. Bassoli, L. Vincenzi, M. Bovo, and C. Mazzotti, "Dynamic identification of an ancient masonry bell tower using a mems-based acquisition system," in *2015 IEEE Workshop on Environmental, Energy, and Structural Monitoring Systems (EESMS) Proceedings*. IEEE, 2015, pp. 226–231.

[354] A. Saisi, C. Gentile, and A. Ruccolo, "Continuous monitoring of a challenging heritage tower in monza, italy," *Journal of Civil Structural Health Monitoring*, vol. 8, no. 1, pp. 77–90, 2018.

[355] S. Grondel, J. Assaad, C. Delebarre, and E. Moulin, "Health monitoring of a composite wingbox structure," *Ultrasonics*, vol. 42, no. 1-9, pp. 819–824, 2004.

[356] D. L. Mascarenas, M. D. Todd, G. Park, and C. R. Farrar, "Development of an impedance-based wireless sensor node for structural health monitoring," *Smart Materials and Structures*, vol. 16, no. 6, p. 2137, 2007.

[357] A. R. J. Downey, "Sensing skin for the structural health monitoring of mesoscale structures," Ph.D. dissertation, Iowa State University, 2018.

[358] F. Zonzini, M. M. Malatesta, D. Bogomolov, N. Testoni, L. De Marchi, and A. Marzani, "Heterogeneous sensor-network for vibration-based shm," in *2019 IEEE International Symposium on Measurements & Networking (M&N)*. IEEE, 2019, pp. 1–5.

[359] F. Ubertini, S. Laflamme, E. Chatzi, B. Glisic, and F. Magalhaes, "Dense sensor networks for mesoscale shm: innovations in sensing technologies and signal processing," *Measurement Science and Technology*, vol. 28, no. 4, p. 040103, 2017.

[360] G. Capellari, E. Chatzi, and S. Mariani, "Cost–benefit optimization of structural health monitoring sensor networks," *Sensors*, vol. 18, no. 7, p. 2174, 2018.

[361] *STM32F303 RM0316 Reference manual*, STMicroelectronics, 1 2017, rev. 8.

[362] M. Abdulkarem, K. Samsudin, F. Z. Rokhani, and M. F. A Rasid, "Wireless sensor network for structural health monitoring: A contemporary review of technologies, challenges, and future direction," *Structural Health Monitoring*, p. 1475921719854528, 2019.

[363] F. G. Baptista and J. Vieira Filho, "A new impedance measurement system for pzt-based structural health monitoring," *IEEE Transactions on Instrumentation and Measurement*, vol. 58, no. 10, pp. 3602–3608, 2009.

[364] C. Trigona, B. Andò, and S. Baglio, "Performance measurement methodologies and metrics for vibration energy scavengers," *IEEE Transactions on Instrumentation and Measurement*, vol. 66, no. 12, pp. 3327–3339, 2017.

[365] S. De, K. Gupta, R. J. Stanley, M. T. Ghasr, R. Zoughi, K. Doering, D. C. Van Aken, G. Steffes, M. O'Keefe, and D. D. Palmer, "A comprehensive multi-modal nde data fusion approach for failure assessment in aircraft lap-joint mimics," *IEEE Transactions on Instrumentation and Measurement*, vol. 62, no. 4, pp. 814–827, 2013.

[366] B.-T. Wang and C.-C. Wang, "Feasibility analysis of using piezoceramic transducers for cantilever beam modal testing," *Smart Materials and Structures*, vol. 6, no. 1, p. 106, 1997.

[367] A. C. Okafor, K. Chandrashekhara, and Y. Jiang, "Delamination prediction in composite beams with built-in piezoelectric devices using modal analysis and neural network," *Smart materials and structures*, vol. 5, no. 3, p. 338, 1996.

[368] B. Chapuis and E. Sjerve, *Sensors, algorithms and applications for structural health monitoring.* Springer, 2017.

[369] H. M. Elwalwal, S. Mahzan, and A. N. Abdalla, "Crack inspection using guided waves (gws)/structural health monitoring (shm)," *J. Appl. Sci.*, vol. 17, pp. 415–428, 2017.

[370] D. Komorowski and S. Pietraszek, "The use of continuous wavelet transform based on the fast fourier transform in the analysis of multi-channel electrogastrography recordings," *Journal of medical systems*, vol. 40, no. 1, pp. 1–15, 2016.

[371] R. Gorgin, Y. Luo, and Z. Wu, "Environmental and operational conditions effects on lamb wave based structural health monitoring systems: A review," *Ultrasonics*, p. 106114, 2020.

[372] I. Ursu, V. Giurgiutiu, and A. Toader, "Towards spacecraft applications of structural health monitoring," *INCAS Bulletin*, vol. 4, no. 4, pp. 111–124, 2012.

[373] M. Cobos, A. Marti, and J. J. Lopez, "A modified srp-phat functional for robust real-time sound source localization with scalable spatial sampling," *IEEE Signal Processing Letters*, vol. 18, no. 1, pp. 71–74, 2010.

[374] L. Zeng, X. Cao, L. Huang, and Z. Luo, "The measurement of lamb wave phase velocity using analytic cross-correlation method," *Mechanical Systems and Signal Processing*, vol. 151, p. 107387, 2021.

[375] A. Muller, B. Robertson-Welsh, P. Gaydecki, M. Gresil, and C. Soutis, "Structural health monitoring using lamb wave reflections and total focusing method for image reconstruction," *Applied Composite Materials*, vol. 24, no. 2, pp. 553–573, 2017.

[376] F. Yan, R. L. Royer Jr, and J. L. Rose, "Ultrasonic guided wave imaging techniques in structural health monitoring," *Journal of intelligent material Systems and Structures*, vol. 21, no. 3, pp. 377–384, 2010.

[377] G. Lu, Y. Li, T. Wang, H. Xiao, L. Huo, and G. Song, "A multi-delay-and-sum imaging algorithm for damage detection using piezoceramic transducers," *Journal of Intelligent Material Systems and Structures*, vol. 28, no. 9, pp. 1150–1159, 2017.

[378] L. Demi, "Practical guide to ultrasound beam forming: Beam pattern and image reconstruction analysis," *Applied Sciences*, vol. 8, no. 9, p. 1544, 2018.

[379] S. E. Olson, M. P. DeSimio, and M. M. Derriso, "Beam Forming of Lamb Waves for Structural Health Monitoring," *Journal of Vibration and*

Acoustics, vol. 129, no. 6, pp. 730–738, 01 2007. [Online]. Available: https://doi.org/10.1115/1.2731404

[380] N. Budyn, "On the use of the geometric median in delay-and-sum ultrasonic array imaging," *IEEE Transactions on Ultrasonics, Ferroelectrics, and Frequency Control*, 2020.

[381] G. Matrone, A. S. Savoia, G. Caliano, and G. Magenes, "Ultrasound plane-wave imaging with delay multiply and sum beamforming and coherent compounding," in *2016 38th Annual International Conference of the IEEE Engineering in Medicine and Biology Society (EMBC)*. IEEE, 2016, pp. 3223–3226.

[382] T. Fyleris and E. Jasiūnienė, "Comparative analysis of plane-wave imaging and the total focusing method in the reconstruction of complex geometrical surfaces," *Surface Topography: Metrology and Properties*, vol. 7, no. 3, p. 035011, 2019.

[383] J. Opretzka, M. Vogt, and H. Ermert, "A model-based synthetic aperture focusing technique for high-frequency ultrasound imaging," in *8th European Conference on Synthetic Aperture Radar*. VDE, 2010, pp. 1–4.

[384] J. E. Michaels and T. E. Michaels, "Guided wave signal processing and image fusion for in situ damage localization in plates," *Wave motion*, vol. 44, no. 6, pp. 482–492, 2007.

[385] X. Zhao, R. L. Royer, S. E. Owens, and J. L. Rose, "Ultrasonic lamb wave tomography in structural health monitoring," *Smart Materials and Structures*, vol. 20, no. 10, p. 105002, 2011.

[386] E. Schubert, J. Sander, M. Ester, H. P. Kriegel, and X. Xu, "Dbscan revisited, revisited: why and how you should (still) use dbscan," *ACM Transactions on Database Systems (TODS)*, vol. 42, no. 3, pp. 1–21, 2017.

[387] M. Ester, H.-P. Kriegel, J. Sander, X. Xu *et al.*, "A density-based algorithm for discovering clusters in large spatial databases with noise." in *kdd*, vol. 96, no. 34, 1996, pp. 226–231.

[388] C. R. Farrar and K. Worden, *Structural health monitoring: a machine learning perspective*. John Wiley & Sons, 2012.

[389] M. Abbas and M. Shafiee, "Structural health monitoring (shm) and determination of surface defects in large metallic structures using ultrasonic guided waves," *Sensors*, vol. 18, no. 11, p. 3958, 2018.

[390] N. Quaegebeur and P. Masson, "Correlation-based imaging technique using ultrasonic transmit–receive array for non-destructive evaluation," *Ultrasonics*, vol. 52, no. 8, pp. 1056–1064, 2012.

[391] A. Kulakovskyi, O. Mesnil, B. Chapuis, O. d'Almeida, and A. Lhémery, "Experimental determination of 3d green's function in composite plates for defect imaging using guided waves."

[392] P.-C. Ostiguy, N. Quaegebeur, and P. Masson, "Assessment of the excitelet algorithm for in-situ mechanical characterization of orthotropic structures," in *Health Monitoring of Structural and Biological Systems 2012*, vol. 8348. International Society for Optics and Photonics, 2012, p. 83480N.

[393] J. Capon, "High-resolution frequency-wavenumber spectrum analysis," *Proceedings of the IEEE*, vol. 57, no. 8, pp. 1408–1418, 1969.

[394] X. Zhao, H. Gao, G. Zhang, B. Ayhan, F. Yan, C. Kwan, and J. L. Rose, "Active health monitoring of an aircraft wing with embedded piezoelectric sensor/actuator network: I. defect detection, localization and growth monitoring," *Smart materials and structures*, vol. 16, no. 4, p. 1208, 2007.

[395] S. Ma, Q. Xia, Y. Liu, Y. Lu, S. Cao, and H. Zhang, "A modified damage index probability imaging algorithm based on delay-and-sum imaging for synthesizing time-reversed lamb waves," *Journal of Vibroengineering*, vol. 21, no. 8, pp. 2140–2147, dec 2019. [Online]. Available: https://doi.org/10.21595%2Fjve.2019.20568

[396] M. A. Aldhaeebi, K. Alzoubi, T. S. Almoneef, S. M. Bamatraf, H. Attia, and O. M. Ramahi, "Review of Microwaves Techniques for Breast Cancer Detection," *Sensors*, vol. 20, no. 8, p. 2390, Apr. 2020.

[397] E. Norouzzadeh, S. Chamaani, and J. Moll, "Parametric Study of Time-Reversal Imaging for the Detection of Tumors in MRI-derived Breast Phantoms," in *2019 12th German Microwave Conference (GeMiC)*. Stuttgart, Germany: IEEE, Mar. 2019, pp. 206–209.

[398] G. Matrone, A. Ramalli, P. Tortoli, and G. Magenes, "Experimental evaluation of ultrasound higher-order harmonic imaging with filtered-delay multiply and sum (f-dmas) non-linear beamforming," *Ultrasonics*, vol. 86, pp. 59–68, 2018.

[399] S. Jeon, E.-Y. Park, W. Choi, R. Managuli, K. jong Lee, and C. Kim, "Real-time delay-multiply-and-sum beamforming with coherence factor for in vivo clinical photoacoustic imaging of humans," *Photoacoustics*, vol. 15, p. 100136, 2019.

[400] A. Ramalli, M. Scaringella, G. Matrone, A. Dallai, E. Boni, A. S. Savoia, L. Bassi, G. E. Hine, and P. Tortoli, "High dynamic range ultrasound imaging with real-time filtered-delay multiply and sum beamforming," in *2017 IEEE International Ultrasonics Symposium (IUS)*. IEEE, 2017, pp. 1–4.

[401] S. R. M. Rostami, M. Mozaffarzadeh, A. Hariri, J. V. Jokerst, and M. Ghaffari-Miab, "Openacc gpu implementation of double-stage delay-multiply-and-sum algorithm: toward enhanced real-time linear-array photoacoustic tomography," in *Photons Plus Ultrasound: Imaging and Sensing 2019*, vol. 10878. International Society for Optics and Photonics, 2019, p. 108785C.

[402] S. E. Olson, M. P. DeSimio, and M. M. Derriso, "Beam forming of lamb waves for structural health monitoring," 2007.

[403] C. Holmes, B. Drinkwater, and P. Wilcox, "The post-processing of ultrasonic array data using the total focusing method," *Insight-Non-Destructive Testing and Condition Monitoring*, vol. 46, no. 11, pp. 677–680, 2004.

[404] J. E. Michaels and T. E. Michaels, "Guided wave signal processing and image fusion for in situ damage localization in plates," *Wave Motion*, vol. 44, no. 6, pp. 482–492, 2007, special Issue of Selected Papers Presented at the International Symposium on Mechanical Waves in Solids. [Online]. Available: https://www.sciencedirect.com/science/article/pii/S0165212507000212

[405] J. E. Michaels, A. J. Dawson, T. E. Michaels, and M. Ruzzene, "Approaches to hybrid shm and nde of composite aerospace structures," in

Health Monitoring of Structural and Biological Systems 2014, vol. 9064. International Society for Optics and Photonics, 2014, p. 906427.

[406] A. J. Croxford, P. D. Wilcox, G. Konstantinidis, and B. W. Drinkwater, "Strategies for overcoming the effect of temperature on guided wave structural health monitoring," in *Health Monitoring of Structural and Biological Systems 2007*, vol. 6532. International Society for Optics and Photonics, 2007, p. 65321T.

[407] V. Červenỳ and J. E. P. Soares, "Fresnel volume ray tracing," *Geophysics*, vol. 57, no. 7, pp. 902–915, 1992.

[408] G. B. Santoni, L. Yu, B. Xu, and V. Giurgiutiu, "Lamb wave-mode tuning of piezoelectric wafer active sensors for structural health monitoring," 2007.

[409] A. Migot, H. Mei, and V. Giurgiutiu, "Numerical and experimental investigation of delaminations in a unidirectional composite plate using ndt and shm techniques," *Journal of Intelligent Material Systems and Structures*, p. 1045389X20978294, 2020.

[410] M. Welvaert and Y. Rosseel, "On the definition of signal-to-noise ratio and contrast-to-noise ratio for fmri data," *PloS one*, vol. 8, no. 11, p. e77089, 2013.

[411] J. T. Bushberg and J. M. Boone, *The essential physics of medical imaging*. Lippincott Williams & Wilkins, 2011.

[412] M. Engholm and T. Stepinski, "Adaptive beamforming for array imaging of plate structures using lamb waves," *IEEE transactions on ultrasonics, ferroelectrics, and frequency control*, vol. 57, no. 12, pp. 2712–2724, 2010.

[413] D. N. Alleyne and P. Cawley, "A 2-dimensional fourier transform method for the quantitative measurement of lamb modes," in *IEEE Symposium on Ultrasonics*. IEEE, 1990, pp. 1143–1146.

[414] C. Willberg, S. Duczek, J. V. Perez, D. Schmicker, and U. Gabbert, "Comparison of different higher order finite element schemes for the simulation of lamb waves," *Computer methods in applied mechanics and engineering*, vol. 241, pp. 246–261, 2012.

[415] K. B. Prakash, S. Zhou, T. C. Morgan, D. F. Hanley, and W. L. Nowinski, "Segmentation and quantification of intra-ventricular/cerebral hemorrhage in ct scans by modified distance regularized level set evolution technique," *International journal of computer assisted radiology and surgery*, vol. 7, no. 5, pp. 785–798, 2012.

[416] Y. Chen, G. Chen, Y. Wang, N. Dey, R. S. Sherratt, and F. Shi, "A distance regularized level-set evolution model based mri dataset segmentation of brain's caudate nucleus," *IEEE Access*, vol. 7, pp. 124 128–124 140, 2019.

[417] S. Nanthakumar, T. Lahmer, X. Zhuang, G. Zi, and T. Rabczuk, "Detection of material interfaces using a regularized level set method in piezoelectric structures," *Inverse Problems in Science and Engineering*, vol. 24, no. 1, pp. 153–176, 2016.

[418] A. M. Braga, R. C. Marques, F. A. Rodrigues, and F. N. Medeiros, "A median regularized level set for hierarchical segmentation of sar images," *IEEE Geoscience and Remote Sensing Letters*, vol. 14, no. 7, pp. 1171–1175, 2017.

[419] L. Yu and Z. Tian, "Phased array techniques for damage detection in aerospace structures," in *Structural Health Monitoring (SHM) in Aerospace Structures*. Elsevier, 2016, pp. 285–306.

[420] Ł. Pieczonka, Ł. Ambroziński, W. J. Staszewski, D. Barnoncel, and P. Pérès, "Damage detection in composite panels based on mode-converted lamb waves sensed using 3d laser scanning vibrometer," *Optics and lasers in engineering*, vol. 99, pp. 80–87, 2017.

[421] D. Alleyne and P. Cawley, "A two-dimensional fourier transform method for the measurement of propagating multimode signals," *The Journal of the Acoustical Society of America*, vol. 89, no. 3, pp. 1159–1168, 1991.

[422] L. Yu and Z. Tian, "Lamb wave structural health monitoring using a hybrid pzt-laser vibrometer approach," *Structural Health Monitoring*, vol. 12, no. 5-6, pp. 469–483, 2013.

[423] F. Cabello, J. León, Y. Iano, and R. Arthur, "Implementation of a fixed-point 2d gaussian filter for image processing based on fpga," in *2015 Signal Processing: Algorithms, Architectures, Arrangements, and Applications (SPA)*. IEEE, 2015, pp. 28–33.

[424] Y. Keshmiri Esfandabadi, "Compressive sensing and imaging of guided ultrasonic wavefields," Ph.D. dissertation, University of Bologna, 2020.

[425] S. Vázquez, J. Gosálbez, W. Wright, C. Gallardo, I. Bosch, and A. Carrión, "Airborne ultrasonic technique to measure leaky lamb waves with narrowband and low-frequency excitation," in *International Congress on Ultrasonics*, 2019.

[426] X. Cao, L. Zeng, J. Lin, and J. Hua, "A correlation-based approach to corrosion detection with lamb wave mode cutoff," *Journal of Nondestructive Evaluation*, vol. 38, no. 4, pp. 1–16, 2019.

[427] E. B. Flynn, S. Y. Chong, G. J. Jarmer, and J.-R. Lee, "Structural imaging through local wavenumber estimation of guided waves," *Ndt & E International*, vol. 59, pp. 1–10, 2013.

[428] K. Xu, D. Ta, P. Moilanen, and W. Wang, "Mode separation of lamb waves based on dispersion compensation method," *The Journal of the Acoustical Society of America*, vol. 131, no. 4, pp. 2714–2722, 2012.

[429] C. R. Ng, J. C. M. Than, O. M. Rijal, R. M. Kassim, A. Yunus, and N. M. Noor, "Construction of 3d lung image morphology using 3d distance regularized level set," *ARPN Journal of Engineering and Applied Sciences*, vol. 14, no. 1, pp. 109–113, 2019.

Author's publications

[AP1] F. Zonzini, M. M. Malatesta, D. Bogomolov, N. Testoni, A. Marzani, and L. De Marchi, "Vibration-based shm with upscalable and low-cost sensor networks," *IEEE Transactions on Instrumentation and Measurement*, vol. 69, no. 10, pp. 7990–7998, 2020.

[AP2] F. Zonzini, M. M. Malatesta, D. Bogomolov, N. Testoni, L. D. Marchi, and A. Marzani, "Heterogeneous sensor-network for vibration-based shm," in *2019 IEEE International Symposium on Measurements Networking (M N)*, 2019, pp. 1–5.

[AP3] S. Quqa, M. Malatesta, P. Martakis, and A. Movsessian, "Investigation on damage sensitive features for optimal sensor networks based on real-scale recordings," in *EURODYN 2020 Proceedings of the XI International Conference on Structural Dynamics Streamed from Athens, Greece 23-26 November 2020*, vol. 1. European Association for Structural Dynamics (EASD), 2020, pp. 936–947.

[AP4] M. M. Malatesta, F. Zonzini, D. Bogomolov, N. Testoni, L. De Marchi, and A. Marzani, "Structural health monitoring reliability enhancement by an automated sensor tuning procedure," in *Proceedings of the 30th European Safety and Reliability Conference*

and the 15th Probabilistic Safety Assessment and Management Conference, 2020.

[AP5] M. M. Malatesta, R. Neubeck, J. Moll, K. Tschöke, and L. De Marchi, "Double stage dmas with fresnel zone filtering in guided waves damage imaging," *IEEE Transactions on Ultrasonics, Ferroelectrics, and Frequency Control*, 2022.

[AP6] M. M. Malatesta, N. Testoni, L. De Marchi, and A. Marzani, "Lamb waves direction of arrival estimation based on wavelet decomposition," in *2019 IEEE International Ultrasonics Symposium (IUS)*. IEEE, 2019, pp. 1616–1618.

[AP7] M. M. Malatesta, N. Testoni, A. Marzani, and L. De Marchi, "Guided waves direction of arrival estimation based on calibrated," *Lect. Notes Electr. Eng*, vol. 627, pp. 363–369, 2020.

[AP8] M. M. Malatesta, D. Bogomolov, M. Messina, D. D' Ippolito, N. Testoni, L. De Marchi, and A. Marzani, "The delay multiply and sum algorithm for lamb waves based structural health monitoring," in *European Workshop on Structural Health Monitoring*. Springer, 2020, pp. 657–666.

[AP9] M. M. Malatesta, L. De Marchi, and J. Moll, "3d microwave breast imaging using double stage delay multiply and sum beamforming," in *2022 European Conference on Antennas and Propagation (EuCAP)*. IEEE, 2022.

[AP10] M. M. Malatesta, J. Moll, P. Kudela, M. Radzienski, and L. De Marchi, "Wavefield analysis tools for wavenumber and velocities

extraction in polar coordinates," *IEEE Transactions on Ultrasonics, Ferroelectrics, and Frequency Control*, 2021.

[AP11] L. De Marchi, N. Testoni, M. Malatesta, and G. Augugliaro, "Processing innovativo per la localizzazione delle sorgenti di emissioni acustiche."